MICROCOPY RESOLUTION TEST CHART
NATIONAL BUREAU OF STANDARDS 1963 A

LEVEL

REPORT DOCUMENTATION PAGE		READ INSTRUCTIONS BEFORE COMPLETING FORM
1. REPORT NUMBER ETL-0192	2. GOVT ACCESSION NO.	3. RECIPIENT'S CATALOG NUMBER
4. TITLE (and Subtitle) SPATIAL LIGHT MODULATORS: TEST AND EVALUATION		5. TYPE OF REPORT & PERIOD COVERED Contract Report
		6. PERFORMING ORG. REPORT NUMBER
7. AUTHOR(s) David Casasent Sanjiv Natu		8. CONTRACT OR GRANT NUMBER(s) DAAK70-78-C-0076
9. PERFORMING ORGANIZATION NAME AND ADDRESS Department of Electrical Engineering Carnegie-Mellon University Pittsburgh, PA 15213		10. PROGRAM ELEMENT, PROJECT, TASK AREA & WORK UNIT NUMBERS 6.27.07.A 4A762707A855 855C00007
11. CONTROLLING OFFICE NAME AND ADDRESS U.S. Army Engineer Topographic Laboratories Fort Belvoir, Virginia 22060		12. REPORT DATE July 1979
		13. NUMBER OF PAGES
14. MONITORING AGENCY NAME & ADDRESS(if different from Controlling Office)		15. SECURITY CLASS. (of this report) Unclassified
		15a. DECLASSIFICATION/DOWNGRADING SCHEDULE
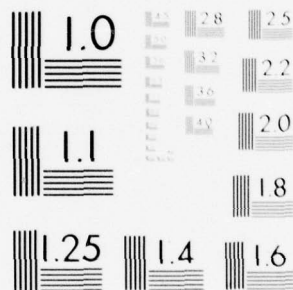
16. DISTRIBUTION STATEMENT (of this Report)

Approved for public release; distribution unlimited.

17. DISTRIBUTION STATEMENT (of the abstract entered in Block 20, if different from Report)

18. SUPPLEMENTARY NOTES

19. KEY WORDS (Continue on reverse side if necessary and identify by block number)

Liquid crystal light valve, optical data processing, photo-DKDP, spatial light modulators

20. ABSTRACT (Continue on reverse side if necessary and identify by block number)

Real-time and reusable spatial light modulators are one of the key technological components necessary in optical data processors. The purpose of this contract is to investigate the test and evaluation procedures to be used with these new data processing devices. Specific attention was devoted to the photo-DKDP and the liquid crystal light valves.

(Continued on reverse side)

DD FORM 1473 EDITION OF 1 NOV 65 IS OBSOLETE
1 JAN 73

From detailed experiments performed on the LCLV, a spatially varying sensitometry and contrast ratio and a voltage and frequency dependent sensitometry were observed. These issues were analyzed, modeled, and theoretically explained. Complete sensitometry, resolution, and noise test data for the photo-DKDP were also obtained. From these experiments, we found a field dependent sensitometry of the Se photo-conductor used in this SLM. This makes the dynamic performance of the device superior to its static performance but makes interframe operations such as image addition and subtraction difficult. A theoretical analysis of this issue was performed and a suggestion to decrease the field dependence by proper device doping was advanced. From these extensive experiments on individual devices, a general test and evaluation procedure for SLMs was formulated. Issues addressed were sensitometry, resolution, and noise. The appropriateness of the various test procedures for resolution and noise measurements to various specific applications were also noted.

An extensive experimental program was also completed in which the photo-DKDP SLM was used as the real-time input transducer for an optical addition and subtraction system, two optical pattern recognition correlators for text and aerial imagery, and two optical signal processors for ambiguity function computation. Comparison of the performance of the real-time SLM systems to similar systems using film as the input material and comparisons to the theoretically expected correlation output plane data were also included. In all cases, the real-time SLM system performed most accurately.

Accession For

NTIS GRA&I	X
DDC TAB	
Unannounced	
Justification	

By_____

Distribution/

Availability Codes

Dist.	Avail and/or special
A	

D D C

R̶E̶C̶E̶I̶V̶E̶D̶
AUG 14 1979

D

TABLE OF CONTENTS

ABSTRACT

Real-time and reusable spatial light modulators are one of the key technolo-
gical components necessary in optical data processors. The purpose of this contract
is to investigate the test and evaluation procedures to be used with these new data
processing devices. Specific attention was devoted to the photo-DKDP and the liquid
crystal light valves.

From detailed experiments performed on the LCLV, a spatially varying sensito-
metry and contrast ratio and a voltage and frequency dependent sensitometry were
observed. These issues were analyzed, modeled, and theoretically explained. Com-
plete sensitometry, resolution, and noise test data for the photo-DKDP were also
obtained. From these experiments, we found a field dependent sensitometry of the
Se photo-conductor used in this SLM. This makes the dynamic performance of the
device superior to its static performance but makes interframe operations such as
image addition and subtraction difficult. A theoretical analysis of this issue
was performed and a suggestion to decrease the field dependence by proper
device doping was advanced. From these extensive experiments on individual devices,
a general test and evaluation procedure for SLMs was formulated. Issues addressed
were sensitometry, resolution, and noise. The appropriateness of the various test
procedures for resolution and noise measurements to various specific applications
were also noted.

An extensive experimental program was also completed in which the photo-DKDP
SLM was used as the real-time input transducer for an optical addition and subtrac-
tion system, two optical pattern recognition correlators for text and aerial
imagery, and two optical signal processors for ambiguity function computation.
Comparison of the performance of the real-time SLM systems to similar systems
using film as the input material and comparisons to the theoretically expected
correlation output plane data were also included. In all cases, the real-time SLM
system performed most accurately.

LIST OF FIGURE CAPTIONS

LIST OF TABLE CAPTIONS

Table 4.1   Components used in the sensitometry data acquisition system of Figure 4.6.

Table 4.2   Components used in the sensitometry data acquisition test system of Figure 4.9.

Table 4.3   Components used in the test system of Figure 4.12.

Table 4.4   Components used in the imaging MTF system of Figure 4.16.

Table 4.5   Components used in the MTF system of Figure 4.19.

Table 4.6   Components used in the reflective imaging MTF system of Figure 4.22.

Table 4.7   Imaging lens parameters.

Table 4.8   Components used in the interferometric OPD system of Figure 4.26.

1. INTRODUCTION

In this final report, we address five major areas of real-time and reusable SLMs for optical data processing. The importance of these key technological components in optical data processing systems is well known. As the discipline of coherent optical data processing matures, it will be essential that all researchers and customers understand the specifications of these components and that they are able to properly specify the test and evaluation procedure to be used to obtain such device data. This program should contribute initial assistance toward this goal.

In Section 2, we present the first unified treatment of a general procedure to be used for SLM test and evaluation. The SLM issues addressed in this discussion include sensitometry, resolution, and noise. This general SLM test and evaluation procedure emerged from extensive experiments on various SLMs, theoretical and basic aspects of resolution, as well as detailed physics and materials aspects of SLM fabrication and operation. The need for unnormalized MTF data with input modulation and a full description of the experimental procedure used, the concern over differences between global and local data, and the importance of a rigorous and organized phase error, noise, dynamic range, and contrast ratio experimental procedure were noted. Acceptable resolution measurement techniques differ when the active SLM thickness is large or the photo-conductive layer is thick.

In Section 3, we describe three detailed issues of SLM testing and device physics and modeling for the LCLV. From extensive tests on this LCLV, we found a spatially varying sensitometry and contrast ratio for the device and a strong voltage and frequency dependence (and control) of these parameters. The spatially varying device performance was analyzed and found to be due to thickness variations in the liquid crystal layer. Analysis of a model for the LCLV device provided this

information and in addition was useful in obtaining theoretical agreement with our experimentally observed voltage and frequency dependent device performance.

In Section 4, we present the results of our sensitometry, resolution, and noise data for the photo-DKDP SLM. In these experiments, a field dependent photo-sensitivity for the Se photo-conductor was observed. This was then theoretically analyzed, the reasons for it were ascertained, and a method to reduce this depen-dence by proper device doping was advanced. This field dependent sensitometry was shown to make dynamic data superior to static data on this device, but to compli-cate performing interframe operations, such as image addition and subtraction. This field dependence may well occur in other SLMs and thus its presence should be considered in the test and evaluation procedures for all SLMs. The appropriateness of various SLM resolution tests to different applications are discussed, as well as the issues of cone angle, depth of focus of the lenses used and other photo-DKDP test components.

An extensive application and operation oriented program using the photo-DKDP SLM as the input transducer was then performed (Section 5). The seven experiments included: (1-3) performing image contrast reversal, addition, and subtraction on the SLM; (4-5) the use of the SLM as the input transducer to two optical pattern recognition systems for text and aerial image pattern recognition and correlation; and (6-7) the use of the photo-DKDP as the input transducer for two different optical signal processing systems for ambiguity function synthesis. The results of these experiments and comparison to off-line results obtained on the same data sets using film as the input medium (for the optical pattern recognition experiments), as well as to theoretically expected results (for the optical signal processing experiments) were obtained with excellent agreement and results. This represented the first comparison of the accuracy of real-time spatial light modulators in optical correla-tor systems. These data are included in Chapter 5.

In Chapter 6, we then summarize our findings and conclusions and recommenda-
tions for future work. The contents of Chapter 2 is an accepted journal paper,
whereas Chapters 3 and 5 involve three other submitted journal papers. A list of
those publications that have resulted from this ETL sponsored program are noted in
Chapter 7.

A firsthand experimental and theoretical test and evaluation program, such as
this one is most necessary. There is no substitute for such firsthand experience.
Also, in any such program, it is expected that many unforeseen and heretofore
unpublished SLM issues will emerge. This program was no exception in this regard.
Although a large quantity of published data existed on both SLMs considered, the
experiments previously reported on these SLMs were generally always so inadequately
documented or unreported that use of or interpretation of the results of others
was impossible.

A rigorous SLM test and evaluation program is necessary. In this, the measure-
ment and test procedures used and specifically the test system and all of its com-
ponents must be adequately documented. It is also necessary to state why each
component was chosen and why this specific test component chosen was used. Moreso
than just collecting data, the program should include an analysis of why the results
obtained are correct and why they did occur. This philosophy guided the experimen-
tal SLM test and evaluation program reported upon here. In one short year, many
findings and four journal papers have been produced, plus this report. These are
initial steps that should aid the direction of future real-time SLM and optical
data processing research.

Performance evaluation of spatial light modulators

David Casasent

An experimental test procedure and associated theoretical formulations are described for the evaluation of spatial light modulators (SLMs) for coherent optical computing. The experimental data included were obtained by us on Hughes liquid crystal and photo DKDP SLMs among others. However, in this paper we address only the general procedures to be used to evaluate SLM performance. The detailed aspects of these tests and their relationships to specific SLMs will be covered in separate papers.

I. Introduction

Optical computing[1] offers the attractive features of parallel processing in real time and thus has been of considerable research interest. It has long been recognized that to realize these advantages of such systems, real-time, reusable, 2-D input and often filter plane transducers are essential. These components are referred to as spatial light modulators (SLMs).[2-4] Our present concern will be with the experimental procedures we feel should be used in the evaluation of SLMs. By this approach we hope to clarify many of the misconceptions present concerning the use of SLMs, interpreting the published specifications for these SLMs, devising appropriate acceptance tests for these SLMs, and the procedures to be used to perform these tests.

The appropriateness of various tests depends on and varies with the SLM used as well as the intended application. Space does not permit an extensive discussion of all SLMs[2-4] or of all optical computing applications,[1] and certainly not extensive discussions of when each test is appropriate. The reader will thus have to be content with general remarks (the purpose of this paper). Experimental results of various test methods applied to the Hughes hybrid field-effect liquid crystal,[5] photo KD*P (deuterated potassium dihydrogen phosphate),[6-8] and the Prom[9] light valves will be included. The discussions will be such that general conclusions and procedures to be used emerge that are of use in general SLM evaluation. Specific discussions of these data for each individual SLM will be discussed in future papers.

Brief descriptions of the three SLMs used are provided in Sec. II for completeness and to enable future issues to be better understood. We divide SLM performance criteria into three areas: sensitometry (Sec. III); modulation transfer function (MTF) (Sec. IV); and noise (Sec. V). This present paper concerns only optically addressed electrooptical SLMs. More detailed extensions to electron beam addressed SLMs and to phase modulated SLMs can be made and will be detailed later.

II. Electrooptical Optically Addressed SLMs

The three major devices that are representative of this class of SLM[1] are the LCLV (liquid crystal light valve),[5] photo KD*P,[6-8] and the Prom.[9] The LCLV consists of over twenty thin film and other layers. It basically consists of a photoconductor, mirror, light-blocking, and LCLV active material layers between two outer transparent electrodes. In operation, an ac voltage is applied between the electrodes, and the pattern to be recorded is incident on the photoconductor at λ_W, whereas readout is in reflection at λ_R from the LCLV side of the device.

The structure and operation of photo KD*P are similar except no light blocking layer exists, and a dc voltage is present across the electrodes. Other differences are that the polarity and value of this voltage are changed during the write (W), read (R), and erase (E) cycles. The major difference between the LCLV and the other SLMs is the lack of long term storage in the LCLV and the need for active erase mechanisms (apply the proper voltage to the electrodes and flooding the photoconductor with light of the proper λ) in the photo KD*P and Prom. Normally $\lambda_W \simeq 514$ nm and $\lambda_R \simeq 633$ nm. In all cases, readout through crossed polarizers is required.

The Prom differs from the prior SLMs in that the electrooptic crystal is both electrooptical and photoconductive. Since no photoconductor layer is present,

6
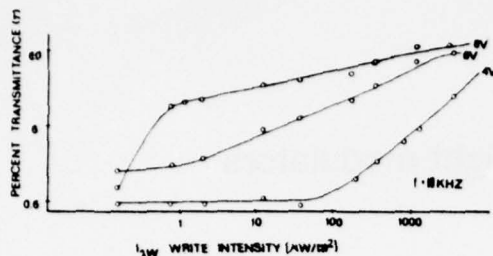
Fig. 1. Global sensitometry curves showing variation with voltage applied across the SLM.

insulating parylene layers are used to produce the required spatial voltage division across the active material proportional to the input λ_W irradiance. It is generally available only in the transmission rather than the reflection readout configuration. Even though no dielectric mirror is present within the SLM structure, it is still generally used in the reflex readout mode.

III. Sensitometry

The representatives of the optically addressed class of SLMs are all sensitive to either the input light irradiance (I) or the light energy (E). The first data required for any SLM is a sensitometry curve of $I_{\lambda W}$ (incident irradiance at λ_W) vs amplitude (t) or irradiance (τ) transmittance. The former curve ($I_{\lambda W}$ vs t) applies when coherent light is used for readout, whereas the latter curve ($I_{\lambda W}$ vs τ) is of use in projection display or similar applications when readout uses noncoherent light. For the LCLV, both the voltage V applied between electrodes and its frequency f affect sensitometry. Such data are shown in Fig. 1 for the LCLV. From these data, we see that the linearity of response, the dynamic range, the useful $I_{\lambda W}$ exposure range, and the $I_{\lambda W}$ threshold at which the device responds all vary with V and f. For the Prom and photo KD*P only V is variable because a dc voltage is applied.

We have found that V and f also affect the SLM noise and the spatial uniformity of the SLM's response. We have also found considerable difference between global sensitometry data (Fig. 1) (obtained by illuminating and reading a large SLM area) and local sensitometry data (Fig. 2) (obtained over a small region of the SLM). Response time, reciprocity data, and other information on the SLM's dynamic response are also of concern and often vary considerably from static data and vary also with the λ_W illumination range used and the address time per point.

A schematic of the basic sensitometry measurement system used is shown in Fig. 3. The vertically polarized λ_R light from a He–Ne laser incident on the polarizing beam splitter (PBS) is reflected toward the SLM. With $I_{\lambda W} = 0$, the λ_R light reflected from the SLM is also vertically polarized and $I_{\lambda R} = 0$. As $I_{\lambda W}$ increases, the elliptical polarization of the λ_R light reflected from the

SLM increases and so does the reflected $I_{\lambda R}$ component that passes through the PBS. To obtain local sensitometry data, the spatial variation of such data, and the effect of V and f choices on noise, linearity, and dynamic range, we used apertures A_1 and A_2 shown in Fig. 3. For the LCLV, we illuminated the photoconductor side of the LCLV through only one of the 3-mm² regions of A_1 and measured $I_{\lambda R}$ in all nine 3-mm regions of A_2 as V, f, and $I_{\lambda W}$ were varied. We denote $I_{\lambda R}$ in the corresponding 3-mm² region of A_2 as signal and the $I_{\lambda R}$ value in all other regions of A_2 as noise.

A summary of our results for the LCLV follow. Less noise was observed as f was decreased and V was increased. As f was lowered, the noise tracked the signal at a lower rate. Most important were the large spatial differences we found in the voltage V_T and irradiance $I_{\lambda WT}$ threshold differences (at which $I_{\lambda R}$ changed). Large differences in V_T and $I_{\lambda WT}$ for signal and noise are desirable. For the LCLV, we found V_T to be lower at low f with larger signal and noise thresholds at $f = 1$ kHz than at 10 kHz and with noise tracking the signal slower at lower f values. The local sensitometry data
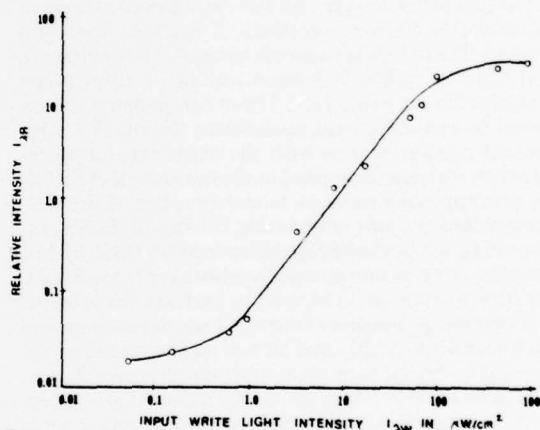
Fig. 2. Representative local sensitometry curve.
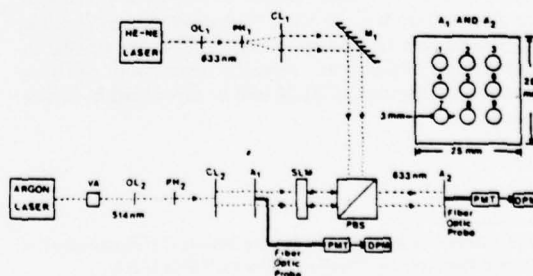
Fig. 3. Schematic diagram of the SLM global and local sensitometry data acquisition system.

for a 3-mm^2 region of the LCLV were shown in Fig. 2. The large 1500:1 contrast ratio and 30,000:1 dynamic range shown in Fig. 2 are misleading, since spatial sensitometry variations make the global values (Fig. 1) for such parameters much less. We have found these spatial variations to be equivalent to horizontal shifts of the sensitometry curve or effectively to changes in $I_{\lambda WT}$ due to spatial variations in the photoconductor, CdTe/CdS heterojunction diode, and LC thickness variations. Thus only global sensitometry data should be used, with local sensitometry data being of use in determining the reasons for the obtained performance and the spatial response uniformity of the device.

The importance of SLM sensitometry data as a first step in SLM testing and other aspects of such data can be seen from Fig. 1. From Fig. 1, we see that the dynamic range of the SLM increases with V. For our application, a large linear dynamic range was desirable, thus $V = 4$–6 V and $f = 10$ kHz were chosen as the SLM operating values. Other applications may require emphasis of other SLM features. Previously published[10] LCLV sensitometry data exhibited a knee in the curve (as in the 8-V curve in Fig. 1). However, as shown, proper selection of V and f can result in a linear t-E curve. This feature by which the shape of the SLM's sensitometry curve can be controlled is of potential use in various applications such as 2-D optical analog/digital conversion, halftone screening, homomorphic filtering, etc.

From Fig. 1, we find the global and hence useful linear dynamic range ($I_{\lambda W \text{ max}}/I_{\lambda W \text{ min}}$) of the SLM to be about 1000:1, the contrast ratio $I_{\lambda R \text{ max}}/I_{\lambda R \text{ min}}$ to be 70:1, and the desirable $I_{\lambda W}$ bias level (center of the linear portion of the curve) to be 70–100 μW/cm^2.

The photodetector used to measure $I_{\lambda R}$ places a lower limit on these curves. For our case, $I_{\lambda R \text{ min}}$ was 70 nW/cm^2, t_{min} was 0.78%, and τ_{min} was 0.6%. The detector used in such sensitometry tests and the $I_{\lambda W}$ range used should of course be compatible with the levels present during the SLM's intended application. The 22% transmission loss observed ($t_{\text{max}} = 78\%$, $\tau_{\text{max}} = 60\%$) was attributed to incomplete reflections from the dielectric mirror within the LCLV structure, to nonideal alignment of the LCLV molecules, and to the inability of the device to rotate completely vertically polarized input λ_R light into horizontally polarized λ_R reflected light. Lens and PBS losses have been compensated for in the data of Figs. 1 and 2.

Because of the hybrid field effect used in the LCLV, the λ_R wavelength used must be matched to the thickness of the LC layer to optimize contrast ratio.[11,12] For other SLMs, λ_R must be chosen to reduce the destructive effects of reading on a stored image. For other SLMs operated with dc voltages, we have found the dielectric mirrors to pass considerable λ_R light thus degrading a stored pattern while it is being read. Although readout through a crossed polarizer/analyzer or PBS system is theoretically optimum,[11,12] we have found the use of separate polarizers and analyzers oriented slightly off from 90° to increase results and the flexibility of the measurement system.

For integrating or storage mode SLMs such as photo-DKDP, we have found that extra care should be taken in acquiring sensitometry data. Specifically, in the photo-DKDP light valve, we have observed a strong dependence of the photosensitivity of the Se photoconductor to the potential gradient present across it. As a result, when long exposure times and low $I_{\lambda W}$ light levels are used, the SLM's sensitivity to the initial and later photocarriers differs considerably. In such cases, one can obtain very different sensitometry data depending upon the write light exposure time used. As usual and here especially, the test conditions should duplicate those present in the SLM's actual application.

IV. Modulation Transfer Function (MTF)

The MTF of an SLM or any device used in an optical processor is one of the most important but seemingly least understood or most misused parameters. We have analytically and experimentally evaluated over eight different MTF tests. Only the most useful ones are discussed here. The appropriateness of various MTF tests depends upon the specific SLM and its intended system application. A discussion of MTF and definitions might appear too tutorial, but is vital to provide an adequate framework for the MTF data to follow.

A. Theoretical Formulation

We assume the pattern recorded on the SLM to be a sinusoid at spatial frequency u' (in 1-D for simplicity). We first clearly distinguish between amplitude m_A and irradiance m_I modulation by describing the SLM's transmittance by

$$t(x) = (1 + m_A \cos 2\pi u' x), \tag{1a}$$

$$\tau(x) = (1 + m_A \cos 2\pi u' x)^2, \tag{1b}$$

where t and τ denote amplitude and irradiance transmittance, respectively. If a reconstructed image of a test pattern recorded on the SLM is formed using the SLM as a relay and the detected output pattern is scanned, the measured modulation is

$$m = m_I = (I_{\text{max}} - I_{\text{min}})/(I_{\text{max}} + I_{\text{min}}). \tag{2}$$

where I_{max} and I_{min} are the measured quantities (the maximum and minimum irradiances in the reconstructed image). A binary image such as the 3-bar Air Force resolution chart is used as the test pattern in such a test.

If noncoherent illumination is used in the above imaging modulation test, the detected pattern (that is scanned to determine I_{max} and I_{min}) is τ. If the image reconstruction is performed in coherent light, the detected pattern is $|t|^2$. Since $\tau = |t|^2$, no difference should result, and $m = m_I$ defined by Eq. (2) is obtained. In practice, the MTF and OTF of the associated imaging optics used affect the observed output patterns in the coherent and noncoherent illumination cases, respectively. Since the MTF of a system is superior to its OTF, coherent illumination is recommended for any such imaging test (when the modulation of the SLM alone rather than of the entire system, in-

cluding lenses, is desired). We have consistently obtained higher modulation values when coherent rather than noncoherent illumination was used.
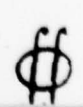
Amplitude modulation m_A is the desired MTF parameter in coherent optical processing application. We can relate m_A to m_I as

$$m_I = \frac{A_{max}^2 - A_{min}^2}{A_{max}^2 + A_{min}^2} = \frac{2m_A}{1 + m_A^2}, \qquad (3)$$

which follows directly from the definitions in Eqs. (1) and (2).

However, this relationship is valid only for monotone inputs, and m_I is best obtained in a coherent image reconstruction experiment. We can always obtain m_I from m_A using Eq. (3).

It is also possible and often preferable to measure m from the Fourier transform of Eq. (1). For this case, we use t in Eq. (1a) to describe the transmittance of the SLM. The amplitude of the Fourier transform of Eq. (1a) is

$$T(u) = A_0[\delta(u) + (m_A/2)\delta(u \pm u')]. \qquad (4)$$

The irradiances I_0 and I_1 of the dc and each first-order term are easily measurable in the Fourier plane. From Eqs. (1)–(4), these are related to m and the measurable quantity I_1/I_0 by

$$I_0/I_1 = (m_A)^2/4. \qquad (5a)$$

$$m_A = 2(I_1/I_0)^{1/2}. \qquad (5b)$$

$$m_I = \frac{4(I_1/I_0)^{1/2}}{1 + 4(I_1/I_0)}. \qquad (5c)$$

The classic MTF as defined is a plot of normalized modulation m_n:

$$m_n = \frac{m_{out}(u')/m_{in}(u')}{m_{out}(0)/m_{in}(0)} \qquad (6)$$

vs the input spatial frequency u'. The measurable quantity in Eqs. (5) is m_{out}. It generally decreases as u' increases. One generally normalizes m by dividing it by its maximum value $m_{out}(0)$, which occurs at low or zero spatial frequency (for deformable SLMs with bandpass MTFs, alternate normalizations are required). Further normalization by $m_{in}(u')/m_{in}(0)$ is used when the modulation m_{in} of the recorded pattern is not 100% and when m_{in} varies with the recorded spatial frequency u'. Thus, for this classic MTF plot, m_n varies from 1 to 0 as u' increases from 0 spatial frequency.

For reasons we amplify later, we have found the use of an unnormalized m vs u' plot to be preferable. We thus plot m vs u', where

$$m = \frac{m_{out}(u')}{m_{in}(u')/m_{in}(0)}. \qquad (7a)$$

For coherent optical systems, an unnormalized amplitude MTF m_A vs u' is used. Generally, we advocate that normalization by the input modulation not be used, rather a plot of

$$m = m_{out}(u') \qquad (7b)$$

vs spatial frequency u' be provided and the constant input modulation be specified. For imaging applica-

tions in noncoherent readout light, an unnormalized irradiance MTF curve of m_I vs u' is appropriate. If m is measured in an image plane, Eq. (2) is used; if the measurement is made in a Fourier plane, Eq. (5) is used. In practice, MTF as defined is really a contrast transfer function (since the phase of the imagery is neglected). However, the above definitions have become common of late and relate directly to the intended device parameter we wish to describe and quantify. We will thus still refer to a plot of m vs u as MTF.

For deformable SLMs and phase modulators, the MTF has a bandpass response and $m_{out}(0) = 0$ and $m = 0$ if t is described by Eq. (1). Thus MTF as described by Eq. (6) is not usable for such devices. Rather, the diffraction efficiency η of these devices is specified. For these SLMs, η is the product of the fraction of the input light in one first-order usable for modulation and the amount of average input light that can be diffracted into one first-order. Thus

$$\eta = \frac{m_A^2/4}{1 + m_A^2/2} \cdot \frac{1 + m_A^2/2}{(1 + m_A)^2} = \frac{m_A^2}{4(1 + m_A)^2} \qquad (8)$$

$$\eta = \frac{[1 - (1 - m_A^2)^{1/2}]^2}{[1 + m_A + (1 - m_A^2)^{1/2}]^2} \simeq \frac{m_n^2}{16}. \qquad (9)$$

In Eq. (9), m_n is defined by Eq. (6), and $m_{in} = 1$ and $m_{out}(0) = 1$ are assumed. The final approximation in Eq. (9) is usually made. This is only valid for small m_n and is not appropriate since $\eta = \frac{1}{16}$ when $m_n = 1$. However, Eq. (9) is still used to extrapolate MTF from η data since low η values look more impressive when expressed as an MTF.

B. Sensitometry Effects

Three aspects of SLM sensitometry affect MTF. From Figs. 1 and 2, we see that the device's $I_{\lambda W}$ region used should be linear if linear modulation is desired and should cover a large range if optimum modulation is of concern. To achieve either result, control of the average $I_{\lambda W \, avg}$ write light and/or the input bias light level $I_{\lambda W \, bias}$ is needed. The recording mechanism used to address the SLM in its intended actual application and the type of input data to be processed affect the bias level and contrast ratio that will actually be present in the input data. For example, reflective aerial imagery usually has a higher bias level and lower contrast than other imagery, whereas signal processing applications usually demand a large dynamic range and linear recording.

A second effect of SLM sensitometry arises when linear recording (a linear relationship between t and $I_{\lambda W}$) is of concern (e.g., as in many signal processing applications). In these cases, use of the proper region of the device's sensitometry curve is vital. The most appropriate method we have found for obtaining linear MTF data is interferometrically (Sec. IV.D) by measuring the second-order Fourier term (I_2) as well as I_0 and I_1. By adjusting the input bias and modulation levels until I_2 is 20 dB below I_1, we can insure that interharmonic distortion is below 1%; we then note that a 1% linear MTF results. Other I_1/I_2 ratios yield MTF data with other degrees of linearity.

The effect of gamma γ (the slope of the SLMs $\tau - I_{\lambda W}$ curve on log-log axes) on MTF is the final effect of sensitometry on MTF that we consider. To include this effect, we assume an irradiance transmittance for the SLM of the form

$$\tau(x) = \tau_0(1 + m_I \cos 2\pi u'x)^{-\gamma}. \tag{10}$$

The Fourier transform of the binomial expansion of $t = \tau^{1/2}$ can be manipulated to relate I_1/I_0 to m_I and γ by Ref. 9:

$$m_I = (4/\gamma)(I_1/I_0)^{1/2}. \tag{11}$$

From Eq. (11), we see that an SLM with $\gamma = 1$ yields twice the irradiance MTF of an SLM with $\gamma = 2$. In most cases, it is inappropriate to separate γ and MTF effects, except when comparing theoretical and experimental resolution data.

C. Imaging MTF

The most used and in some sense the simplest measure of SLM resolution and MTF is obtained by imaging a resolution chart (such as the 3-bar Air Force test chart) onto the SLM, reconstructing the image of the test pattern using the SLM as a relay device, and then scanning the reconstructed image with a photometric microscope. We then measure $I_{\min}$ and $I_{\max}$ for each group/element in the reconstructed image of the test chart; $m_{\text{out}}(u')$ is thus obtained from Eq. (2), and an MTF curve defined by Eq. (7b) not Eq. (6) is plotted. m_A or m_I is used depending upon the application.

Examples of several experimentally obtained unnormalized imaging MTF curves for the LCLV at different voltages and frequencies are shown in Fig. 4. The modulation of the imaging optics used was measured to be unity, whereas m_{in} for the test chart was found to be 0.9 out to 80 cycles/mm. The MTF data presented have been normalized for these values as in Eq. (7b). These initial MTF curves serve to demonstrate several vital aspects of MTF data. First and foremost, unnormalized MTF data must be used since m is then directly the fraction of the input light that is usable for modulation. To demonstrate this, we select the $m = 0.4$ point on both curves. This corresponds to some given amount of usable output light. From Fig. 4(a), we find that we can obtain this amount of light for an input spatial frequency of up to 19 cycles/mm; whereas for the V and f settings used in the Fig. 4(b) data, we can obtain this amount of light only up to 13 cycles/mm of input data. If both curves were normalized, such comparative data would not be present.

Another obvious remark concerning data acquisition is that the MTF data should be continued to low enough spatial frequencies that three approximately equal and constant modulation values result. This is of utmost importance if the MTF curve is normalized. The third issue concerns the SLM resolution one reads from such data. The limiting SLM resolution at $m = 0.05$ is often given but is rarely appropriate for use because of the negligible light levels available at this low modulation. Only a light budget analysis for the full actual system can answer what SLM modulation is necessary. We

advocate the use of unnormalized MTF data and that the resolution be given at the $m = 0.5$ or 50% modulation point. In addition, we note that the input $I_{\lambda W}$ bias value and the true input modulation used be provided if any MTF data are to be of use at the system level. Examples of such data follow in Sec. IV.D.

Other peculiarities of MTF data depend on the specific SLM being tested. For the LCLV, we obtained MTF curves for various control voltages and ac frequencies and found the MTF to be better at higher (10-kHz) frequencies. This appears to be due to the increase in the ratio of the transverse-to-longitudinal impedance of the LCLV with frequency. Another specific feature of the LCLV is the effect that the λ_R choice has on the device's performance. To reduce the off-state transmittance of the SLM, the thickness of the LC layer must be properly adjusted, because the twisted nematic effect determines the off state. The thickness of the LC layer in the LCLV we used was optimized for $\lambda_R = 633$ nm. We can partly attribute the lower modulation and resolution obtained in Fig. 4(b) compared with Fig. 4(a) to the broadband λ_R light used in the one case. Other MTF tests performed on the LCLV with
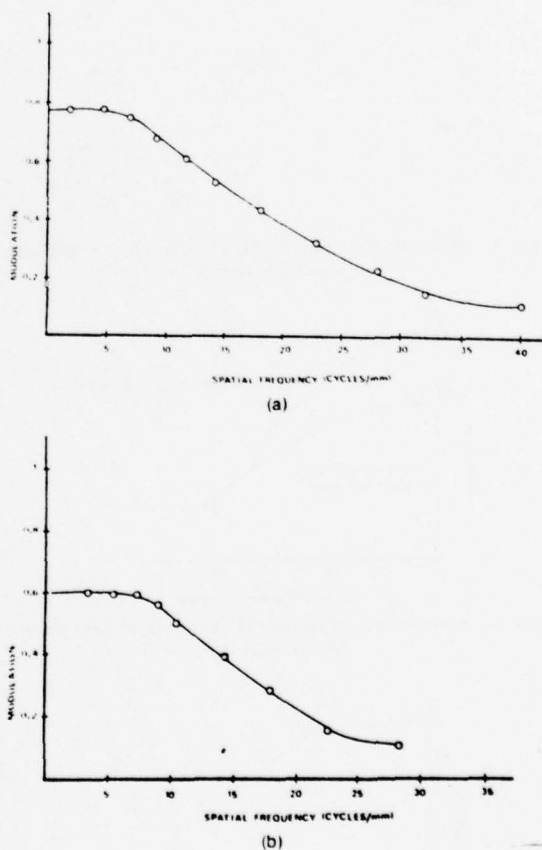
Fig. 4. Imaging MTF curves: (a) 6 V and 10 kHz with coherent λ_R = 633 nm light; (b) 3.5 V and 10 kHz with noncoherent filtered λ_R = 620 ± 10-nm light.

$\lambda_R = 514$ nm yielded even poorer modulation and resolution.

Our objections to an imaging MTF test are many. The test is subjective and plagued by operator attitude and error. This is due primarily to the degree to which the input data can be focused onto the SLM. More important, since the test patterns used (3-bar Air Force chart) are binary, this type of test does not investigate the gray scale resolution or linearity of the SLM. Finally, the input bias light level and input modulation are not easily variable in such MTF tests.

D. Interferometric MTF

For the reasons noted above, interferometric MTF data are preferable to imaging MTF data for reasons of both experimental ease and data content. The interferometric MTF data acquisition system used is shown in Fig. 5. In this architecture, the interference pattern

Fig. 5. Schematic diagram of an SLM interferometric MTF data acquisition system.
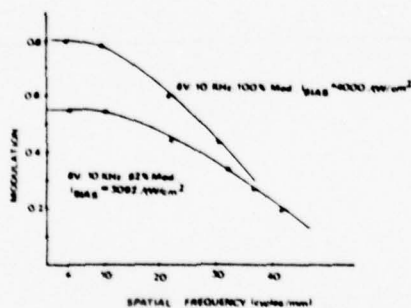
Fig. 6. Nonlinear interferometric MTF curves at different bias and input modulation.
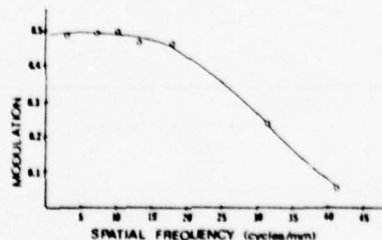
Fig. 7. Linear interferometric MTF curve with 1% SLM linearity.

of two plane waves of irradiances I_A and I_B inclined at an angle θ is recorded. The subsequent amplitude transmittance is

$$t = I_A + I_B + 2(I_A I_B)^{1/2} \cos 2\pi u' x. \qquad (12)$$

where $u' = 4\pi(\sin\theta)/\lambda$ is the spatial frequency of the recorded fringe pattern in cycles/mm. From Eqs. (1), (12), and (2), we find

$$m_{in} = \frac{2(I_A/I_B)^{1/2}}{1 + (I_A/I_B)} = \frac{2R^{1/2}}{1 + R}. \qquad (13)$$

From Eq. (13), we see that by varying the ratio R of the intensities of the two beams, we can control m. By controlling $I_{avg} = I_A + I_B$, we can vary the bias point chosen on the SLM's sensitometry curve. By varying θ by changing the tilt angle of mirror M_3, the spatial frequency u' can be changed. The Fourier transform of Eq. (13) can then be scanned by a fiber optic probe (FP), photometric microscope, and photomultiplier (PMT) system.

This system topology of Fig. 5 thus allows us to vary easily the bias level, spatial frequency u', and modulation m of the input fringe pattern. Of further concern is the fact that the sine wave pattern in Eq. (13) is automatically in focus over the entire thickness of the SLM, thus completely overcoming any input focusing errors that could arise in an imaging MTF system. To obtain the MTF of the SLM, we can monitor I_0 and I_1 in the Fourier transform of Eq. (13) for different u' input spatial frequencies and apply Eq. (5b) or Eq. (5c) to determine m. Equation (7b) is then used to obtain the MTF plot of m vs u'.

Two such MTF curves are shown in Fig. 6 with slightly different m_{in} and I_{avg} levels. These two curves vividly demonstrate many of the MTF remarks advanced earlier. The effect of a slight 18% change in m_{in} on MTF is seen to be dramatic. With a lower m_{in}, less of the SLM's sensitometry curve is used and the reduced m shown results. The need to specify MTF test conditions (I_{avg} and m_{in}) is thus apparent. Similarly, only through unnormalized MTF data, as shown, do these differences appear. In the lower curve in Fig. 6, we find a lower peak m (due to the lower m_{in}); but the resolution (at 50% of the peak m value) is found to be larger (37 cycles/mm) for the lower $m_{in} = 0.82$ case than for the larger $m_{in} = 1.0$ case (32 cycles/mm). However, the unnormalized MTF data of Fig. 6 clearly convey the point that more usable output light is always present with the larger m_{in} value. Such results would not appear in MTF data if the normalized MTF definition in Eq. (6) were used. Similarly, the relevance of these data would not be of use unless I_{avg} and m_{in} were specified as done in Fig. 6.

We refer to the data of Fig. 6 as a nonlinear MTF curve. A linear MTF curve for the same LCLV SLM is shown in Fig. 7. To obtain these latter data, I_2 was monitored as well as I_1/I_0. By keeping I_2 below I_1 by 20 dB (by reducing m_{in} and adjusting I_{avg} accordingly), we can ensure that the SLM's resultant MTF is linear within 1% (i.e., less than 1% interharmonic distortion). With I_{avg} adjusted to lie in the center of the linear por-

tion of the SLM's sensitometry curve of Fig. 1 and with m_{in} reduced to 0.79, the curve of Fig. 7 results. The resolution at $m = 0.25$ (50% of the peak $m = 0.5$ value) is seen to be 32 cycles/mm. The modulation at 32 cycles/mm is below that obtainable for nonlinear SLM operation in Fig. 6 as expected. Only such fully documented and unnormalized MTF data are of use in deciding on the performance to be expected of an SLM in a given application as well as in comparing the MTFs of different SLMs.

The effect of modulation on the performance of an optical correlator is rarely quantified, but is of major concern in determining the usable SLM resolution in a system scenario. For example, an irradiance modulation of 10% is equivalent to an amplitude modulation of 5%. The resultant peak intensity in one sidelobe in the Fourier plane pattern is 32 dB below dc. This represents an intolerable loss in most cases. Such light level budget analyses are needed for each specific application to determine the necessary system performance. The output detector used greatly affects such system data.

E. Depth of Focus

Interferometric MTF data are more reproducible than imaging MTF data and include gray scale and linearity information on the SLM. It has thus become the most used MTF data acquisition method. However, because of the infinite depth of field of the recorded fringe pattern (the feature that makes this MTF method easy to perform), this test may yield different results than one would obtain in the SLM's actual system application. The actual depth of focus of the interferometric fringe pattern is effectively the thickness of the photoconductor layer (10 μm) for photo-KD*P and the LCLV. However, the Prom crystal is thick (500–900 μm) and both electrooptic and photoconductive. For such devices, the depth of focus of the interferometric pattern is effectively the crystal's thickness.

Interferometric MTF data will be valid only if the SLM's actual data recording system has a depth of focus comparable with the thickness of the photoconductor or crystal (depending upon the SLM). In addition, for an SLM such as photo-KD*P with a 10-μm thick photoconductor layer, interferometric MTF data are only valid up to 50-cycle/mm input spatial frequencies (the reciprocal of 2×10 μm) and only if the depth of focus of the data recording system in the device's actual application exceeds 10 μm. When the SLM is used in the frequency plane and interference patterns such as a matched spatial filter[13] or joint transform[14] are recorded on it, the interferometric MTF is, of course, valid. When the SLM is used as an image plane transducer, the infinite depth of focus assumption is not always valid. If low f-number optics are used, care must be taken that the thickness of the photoconductor does not exceed the depth of focus of the actual recording optics used. For f-number optics with a 10-μm spot size, the depth of focus is

$$\text{depth of focus} = 2 \ (f\text{-number})(\text{spot size}) = 80 \ \mu m. \quad (14)$$

If the photoconductor's thickness (or the active crystal thickness for the case of the Prom) exceeds this 80-μm value, interferometric MTF test data are not appropriate. In actual use, the MTF will decrease because of overlap of the light cone away from focus. In summary, interferometric MTF data will yield the best possible SLM resolution and modulation. Whether such SLM performance is actually obtainable depends upon the specific way the SLM is used in the actual system application.

F. Alternate MTF Tests

The usefulness, ease of implementation, and reproducibility of over eight MTF tests were evaluated first-hand on over four different SLMs during this program. MTF tests that required sine wave input transparencies of various spatial frequencies and LFM Sayce charts of linearly varying spatial frequency were found to suffer from lack of inputs of adequate precision. Correlation-based MTF tests[15] were found to be plagued by low light levels and diffraction efficiency (i.e., the problem became one of measuring detector accuracy rather than SLM performance).

One attractive MTF test that is appropriate for evaluation of SLMs in system applications in which data are written sequentially on the SLM by a scanning recording device is the edge or gradient MTF test method.[16-18] In such a test, an edge is imaged onto the SLM, and its reconstructed image (using the SLM as a relay device), is scanned. These data are then smoothed and can be corrected for the SLM's sensitometry curve if appropriate. Differentiation of such an edge image results in the SLM's line spread function. The Fourier transform of this line spread function is then the SLM's optical transfer function, whose magnitude is the device's MTF. The operations of smoothing, sensitometry correction, differentiation, Fourier transformation, and magnitude calculation on the edge image are generally performed in digital electronics. This results in a rather indirect MTF calculation. This fact plus the requirement that the system be space-invariant in the image analysis domain (optical systems are in fact space-variant)[19-21] tend to reduce the potential appropriateness of this MTF analysis method. In time, dedicated hardware and software advances may change this observation.

V. Noise

The third and final aspect of SLM evaluation to be discussed is that of SLM noise. We distinguish four types of noise: distortions; phase; and scatter and signal-dependent noise.

A. Distortion

Distortion is of concern when linear recording is required. MTF data with control of the interharmonic distortion level can be measured by the linear interferometric MTF technique described in Sec. IV.D.
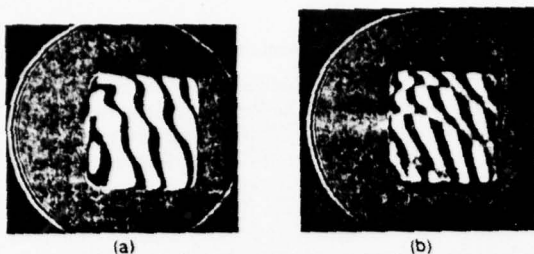
Fig. 8. Interferograms of the OPD of an SLM: (a) 0 V; (b) 5 V, 6 kHz.

B. Phase Error

Phase errors are of utmost concern in coherent optical correlators. Slowly varying phase errors or linear phase errors are not of major concern except in optical correlators. Such error sources in coherent optical computers are best described by optical path difference (OPD) maps.[21-24] Such OPD plots must be provided for all input spatial frequencies and aperture sizes to characterize completely a coherent optical system.[22] To relate these phase errors to the accuracy of an optical processor, 2-D spatial OPD maps are necessary.[21] Techniques for easily acquiring such data have been previously reported.[23,24] Accurate analysis of such data requires one to model the optical processor and its components as a space-variant system.[19-21] Thus, to obtain quantitatively meaningful SLM phase error data, one must acquire spatial OPD data on the SLM rather than the rms OPD data characteristically available for such components. In summary, it is not the average phase error that matters, but rather how this phase error is distributed.

In obtaining any type of SLM data, even rms OPD, the test should be performed with voltage applied to the SLM [Fig. 8(b)], since often a considerably different OPD phase error results than if no voltage is applied to the device [Fig. 8(a)].

C. Scatter Level

The surface roughness and cosmetic imperfections of the SLM generally manifest themselves as random phase errors of high spatial frequency. These noise sources predominantly contribute to the system's background noise level or scatter level. We refer to this as scatter level noise. It directly affects the maximum obtainable system dynamic range. The extent of this noise source is most easily measured by imaging a square aperture onto the SLM and scanning its Fourier transform pattern. Such a cross-sectional Fourier scan is shown in Fig. 9(b). For comparison purposes, the Fourier transform of an empty square aperture obtained using the same lens system is scanned [Fig. 9(a)]. Care should be taken to extend the Fourier plane scan out to several hundred sidelobes until the pattern's exponential decrease stabilizes.

From Fig. 9(a), we find that the scatter level of the optical system alone [Fig. 9(a)] exceeds 40 dB at $u = 4$ cycles/mm and is within 1 dB of the theoretical value. Comparing Figs. 9(a) and 9(b), we see that the presence of the SLM (the LCLV for this data) results in an increased scatter level 3–5 dB above the theoretical value and above that of the optical system alone.

D. Signal-to-Noise Ratio (SNR)

Signal dependent noise or the ratio of signal to noise level (in the same spatial frequency band) is often of more concern. We have found two methods to be of use in obtaining such data. The first is to record a square-wave pattern on the device by imaging an accurate test pattern onto the SLM. A scan of the Fourier transform of this input square wave is shown in Fig. 10 for a 5-cycle/mm square wave recorded on the LCLV. This pattern shows Fourier components at both even and odd harmonics of the fundamental frequency of the square-wave grating. The amplitudes of these Fourier components are all within 1 dB of the theoretical values found from a Fourier series expansion of the input pattern. Our present concern is with the measurable null depth of this pattern. From Fig. 10, we see that the system's dynamic range, including all SLM noise, is a maximum of 52 dB even with an input signal present.
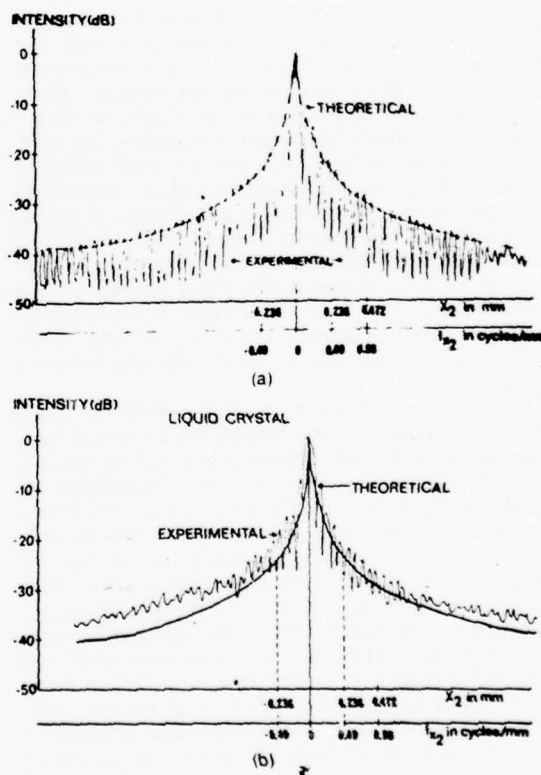
Fig. 9. Cross-sectional scan of the Fourier transform of a square aperture for scatter-level noise tests: (a) empty aperture; (b) SLM in aperture.

(a)

(b)
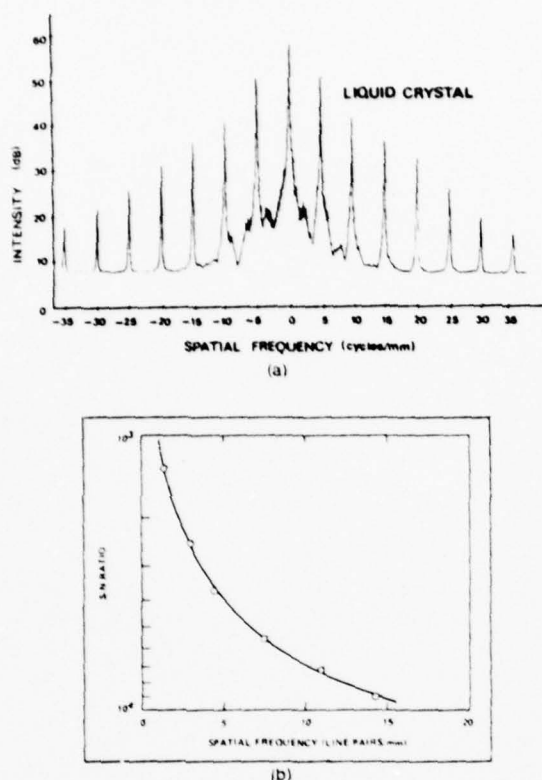
Fig. 10. SNR SLM test data: (a) cross-sectional scan of the Fourier transform of a square wave recorded on the SLM; (b) plot of SNR vs spatial frequency obtained from Fourier plane data of interferometrically recorded sine waves.[5]

VI. Conclusions

As optical computing and SLM technology mature and as more coherent optical processing systems are fabricated and delivered, the specifications and testing of the SLM components (so vital to such systems) must be standardized. We feel the procedure described in this paper and demonstrated by experimental confirmation provide a necessary first step toward such ends.

Since the amplitude of increasing Fourier orders of the square wave decreases, whereas the noise level remains essentially constant, true SNR is not obtainable from such data. However, true SNR can be measured by interferometrically recording a sine wave on the SLM and investigating its Fourier transform pattern for various input spatial frequencies u'. The maximum obtainable I_1/I_2 ratio or the I_1 to scatter level ratio obtainable in the Fourier plane will then provide us with the SNR of the SLM vs spatial frequency u'. An example of such data is shown[5] in Fig. 10(b) for the LCLV. The increase in SNR with spatial frequency occurs because the system's scatter level decreases faster with u than the SLM's MTF. Care should be taken to measure such I_1, I_2 and scatter levels with an area photodiode detector whose size equals the diffraction limited spot size of the Fourier transform system used.

References

1. Special Issue on Optical Computing, Proc. IEEE 65 (January 1977).
2. D. Casasent, Proc. IEEE 65, 143 (1977).
3. D. Casasent, "Coherent Light Valves," in Applied Optics and Optical Engineering, R. Kingslake and B. J. Thompson, Eds. (Adacemic, New York, 1979).
4. Special Issue on Spatial Light Modulators, Opt. Eng. 17 (July 1978).
5. W. Bleha et al., Opt. Eng. 17, 371 (1978).
6. G. Marie and J. Donjon, Proc. IEEE 61, 942 (1973).
7. G. Marie, J. Donjon, and J. Hazan, "Pockles Effect Imaging Devices and Their Applications," in Advances in Image Pick-up and Display Vol. 1, B. Kazan, Ed. (Academic, New York, 1974), p. 225.
8. D. Casasent, Opt. Eng. 17, 365 (1978).
9. B. Horwitz and F. Corbett, Opt. Eng. 17, 353 (1978).
10. J. Grinberg et al., Opt. Eng. 14, 217 (1975).
11. J. Grinberg and A. Jacobson, J. Opt. Soc. Am. 66, 1003 (1976).
12. J. Bigelow and R. Kashnow, Appl. Opt. 16, 2090 (1977).
13. A. Vander Lugt, IEEE Trans. Inf. Theory IT-10, 139 (1964).
14. J. Rao, J. Opt. Soc. Am. 57, 798 (1967).
15. A. Grumet, Appl. Opt. 16, 154 (1977).
16. R. Barakat, J. Opt. Soc. Am. 54, 920 (1964).
17. B. Tatian, J. Opt. Soc. Am. 55, 1014 (1965).
18. D. Dutton, Appl. Opt. 14, 513 (1975).
19. G. Winzer and I. Kachel, Opt. Acta 20, 359 (1973).
20. N. Brousseau and H. Arsenault, Appl. Opt. 14, 1679 (1975).
21. T. Luu and D. Casasent, Appl. Opt. 18, 791 (1979).
22. K. Preston, Jr., Coherent Optical Computers (McGraw-Hill, New York, 1972).
23. K. von Bieren, Appl. Opt. 12, 1642 (1973).
24. D. Casasent and T. Luu, Appl. Opt. 17, 2973 (1978).

3.1   SPATIAL VARIATIONS IN A HYBRID FIELD-EFFECT
LIQUID CRYSTAL LIGHT VALVE

Abstract

Spatial sensitometry variations in a liquid crystal light valve are studied, as well as signal induced noise and differences in global and local contrast ratio. The device's off-state is investigated and spatial variations in the thickness of the LC layer are used to quantify the results obtained. Operation with low frequency applied a.c. voltages appears preferable from noise considerations, whereas operation at high frequency appears preferable for improved uniformity.

PACS CODE NOS: 85.60.-q, 35.60.Pg

3.1.1   Introduction

The a.c. liquid crystal light valve (LCLV) [1] employing the hybrid field effect [2] has received considerable attention as a real-time and reusable spatial light modulator [3] for optical data processing [1]. In these applications, uniform response and high contrast ratios are more important than in display applications. In this paper we consider spatial variations in LCLV response uniformity (Section 3.1.3), LCLV noise (Section 3.1.4) and distinguish between global and local contrast ratio data (Section 3.1.5). In Section 3.1.6, we quantify the experimental results found in Sections 3.1.4 and 3.1.5 with an analysis of the device's off-state. We conclude that the observed spatial sensitometry variations and differences in global and local contrast ratio values are due to variations in the thickness of the LC layer and how these spatial variations can be reduced.

3.1.2 The LCLV

The LCLV we used [1,2] consisted of a CdS photo-conductor, CdTe light block-
ing layer, dielectric mirror, and 2.74μm thick LC layer all sandwiched between
transparent indium-tin-oxide electrodes. Initially, all LC molecules in this
device are parallel to the electrode faces and normal to the z axis (light propa-
gation direction). The LC molecules in successive layers exhibit a 45° contin-
uous twist (in the plane of the entrance electrode) over the thickness d of the
LC layer. Data is written on the device by illuminating the CdS side of the LCLV
with λ_W = 514nm light of intensity $I_{\lambda W}$. Readout is in linearly polarized λ_R = 633nm
light in reflection from the opposite LC side of the device. The reflected read
light $I_{\lambda RO}$ is measured through crossed output polarizers. The off-state ($I_{\lambda RO}$ = 0
or transmittance τ = 0) is determined by the twisted nematic effect.

When an a.c. voltage V at frequency f is applied across the electrodes and
some $I_{\lambda W}$ is present, the LC molecules tilt away from the plane of the entrance
electrode. The birefringence of the LC then determines the on-state transmittance
vs. $I_{\lambda W}$ [1,4,5]. Our concern in this paper is with the off-state of this LCLV
device.

3.1.3 Spatial Sensitometry Data

One of our initial concerns were the spatial uniformity of sensitometry data
and contrast ratio values for this LCLV. To obtain such data, the test system of
Figure 3.1 was used. An Argon-ion and He-Ne laser served as the write (λ_W) and
read (λ_R) sources, with readout in reflection through a polarizing beam splitter.
For local sensitometry and contrast ratio data, apertures A_1 and A_2 with nine 3mm
diameter holes (arranged in three rows with three holes per row) were used in the
write and read beams. With only one 3mm diameter region of the LCLV illuminated
with $I_{\lambda W}$ light, the $I_{\lambda RO}$ light in the corresponding 3mm aperture in A_2 was read as
I_W was varied. By varying the spatial location of the 3mm diameter region of the

LCLV on which data was written (and read), the device's local sensitometry curve (transmittance τ vs. $I_{\lambda W}$) resulted. Variations in these curves for different 3mm LCLV regions provide the desired spatial uniformity data on sensitometry.

The results of such an experiment showed that the peak τ occurred at the same $I_{\lambda W}$ value for all 3mm LCLV regions. But for lower $I_{\lambda W}$ values, differences of $\pm 30\%$ were found in τ in various regions with the same $I_{\lambda W}$ input write light. To investigate these spatial uniformity variations, several other experiments were performed.

3.1.4 LCLV Noise

With only the central 3mm hole in A_1 of Figure 3.1 illuminated with constant $I_{\lambda W} = 75\mu w/cm^2$ write light intensity, the reflected readout from the central 3mm hole 5 in A_2 (and hole 2 in A_2 directly above the center of the LCLV aperture) were measured as V across the entire device was varied. We denote the output from hole 2 as noise. In Figure 3.2, we show $I_{\lambda RO}$ for these signal and noise outputs as a function of total a.c. voltage V applied to the LCLV for two frequencies (1kHz and 10kHz) and as a function of frequency for V = 5v. From these data, we note that:

(a) The V threshold at which $I_{\lambda RO}$ starts to increase is larger for the noise than for the signal (see Figures 3.2a and 3.2b).

(b) The noise tracks the signal, but the noise appears to be independent of f, whereas signal response improves as f is decreased.

A large difference in the V thresholds for signal and noise is desirable. Similarly, it is desirable that the noise track the signal at a slower rate. Thus, from these data, operation of the LCLV at lower a.c. frequencies and higher voltages appears to result in superior overall SNR. Fraas, et.al., [6,7] noted that increased a.c. frequency f results in a more spatially uniform τ vs. $I_{\lambda W}$ curve. This is expected since at higher a.c. frequencies, the capacitive rather than the resistive effects of the layers in the LCLV dominate the device's performance.

Since these capacitive terms are controlled by the thicknesses of the various layers in the LCLV structure, and since these thicknesses can be well controlled in thin film fabrication, more uniform response is expected at higher f. In addition, the higher capacitive currents should dominate the sheet-resistivity spreading currents at higher f, thus reducing charge spreading and improving device resolution. These remarks may well apply to the CdS-CdTe layers as analyzed by Fraas, et.al. But for the entire LCLV (including the LC layer), our data of Figure 3.2 indicates that less charge spread coupling and an improved SNR results when the control voltage is operated at a lower a.c. frequency f. The effects of V and f changes on $I_{\lambda RO}$ and τ on the signal component noted in Figure 3.2 were verified and explained earlier [8] by us, as well as the effects of V and f on the shape of the LCLV's sensitometry curve and the observed shifts in the curves with different V and f choices [8]. Thus the signal data in Figure 3.2 appears to be correct and explainable. Hence our experimental observation noted above on LCLV noise appears to be valid.

3.1.5 Global and Local Contrast Ratio

For all local sensitometry data, $I_{\lambda W}$ and $I_{\lambda R}$ were measured with a fiber optic probe connected to a photo-metric microscope and PMT with the apertures A_1 and A_2 in place as in Figure 3.1. For all global sensitometry data, apertures A_1 and A_2 were removed and $I_{\lambda W}$ and $I_{\lambda R}$ measurements were obtained using a $1cm^2$ LCLV area and a $1cm^2$ photo-diode detector. A local sensitometry curve for a 3mm diameter area of the LCLV is shown in Figure 3.3. From the $I_{\lambda RO}$ axis of this curve, we find a local contrast ratio of 1500:1; whereas from the horizontal axis we find a dynamic range of 30,000:1. Clearly, obtaining such performance requires excellent detectors and is only possible on a local basis (in isolated 3mm diameter areas of the LCLV). The global sensitometry curve for the LCLV at the same (6v, 10kHz) operating values showed only a 100:1 contrast ratio. Caution should thus be made in all spatial light modulator evaluations [9] to separate local device performance from

global device specifications and to consider spatial variations or uniformity in all device parameters.

3.1.6 Discussion

Many factors affect global and local LCLV data and the spatial uniformity of the device. For the LCLV substrate, a uniform dark current is needed when V is present. The capacitive impedance of the CdS dominates this at high f and its uniformity is determined by the uniformity of the thickness of the CdS. As shown in References 6 and 7 the thickness uniformity of the CdS appears to be excellent and easily realized by control of the geometry of the sputter process. At low f, the resistive impedance of the CdS and its stoichiometry and doping uniformity dominate. The main source of non-uniform spatial response of the LCLV appears to be spatial variations in the thickness of the LCLV layer. Such thickness variations result in spatial variations in the off-state transmittance of the LCLV. The constancy of the $I_{\lambda W}$ value at which τ saturation was observed in the experiments described in Section 3.1.3 lends further credence to this assumption.

To quantify the results obtained, we thus considered the off-state transmission of an LCLV using a twisted nematic LC molecule arrangement. Many authors have analyzed the transmission of a twisted nematic layer. Grinberg and Jacobson [10] approached this problem by a recursive analysis in which discrete twist angles were assumed for the various LC molecule layers throughout the crystal thickness d. McIntyre and Snyder [11] assumed a continuous z axis twist and employed a more sophisticated coupled mode analysis to obtain a most general result. A Poincare sphere analysis [12] likewise results in analogous results for τ in the off-state.

We denote the total twist angle for the LC layer by α and the total phase introduced between the two birefringent components of the wave by $\beta = 2\pi(\Delta n)d/\lambda$, where Δn is the total index of refraction difference. Then the general result in Reference [11] reduces to

$$\tau_{off} = \frac{1 - \cos \eta}{2\gamma^2 + 1 + \cos \eta} \tag{1}$$

where $\eta = (4\alpha^2 + \beta^2)^{\frac{1}{2}}$ and $\gamma = (\beta/2\alpha)$. Eq. (1) represents a closed form solution. With appropriate approximations, this expression reduces to the result presented in Reference [10].

$$\tau_{off} = \frac{2x^2(1-\cos \beta)}{1-2x^2(1-\cos \beta)} \tag{2}$$

where $x = \frac{1}{2}\gamma$. To obtain minimum τ (in the off-state), we require $(1-\cos \beta) = 0$ or $\beta = 2\pi k$, (where k is an integer which obviously determines the thickness d of the LC layer. With τ small (desirable) for small x and with x small, we approximate (2) as in Reference [10] by

$$\tau_{off} = 2x^2 (1-\cos \beta) , \tag{3}$$

from which we obtain the condition in References [10-12] that $(1-\cos \beta) = 0$ is desired.

Expanding $(1-\cos \beta)$ for $\beta \simeq 2\pi k$, we obtain

$$\tau_{off} = x^2(\beta-2\pi k)^2 = \alpha^2(\Delta\beta^2)/\beta^2 \tag{4}$$

where $(\beta-2\pi k)$ is the error $\Delta\beta$ in β and $\alpha = 2(\pi/4)$ is the total twist angle ϕ for our LCLV. From these manipulations we can express the off-state transmittance τ_{off} in terms of the fractional percent variation Δd in the thickness d of the LC layer as

$$\sqrt{\tau} = \alpha(\Delta\beta/\beta) = (\pi/2) (\Delta\beta/\beta) = (\pi/2) (\Delta d/d) \tag{5}$$

since $\beta = 2\pi\Delta nd/\lambda$. From (5), we see that a 5% spatial variation in the thickness of the LC layer (i.e., $\Delta d/d = 0.05$) results in a minimum $\tau_{off} = 6.16 \times 10^{-3}$ and hence a maximum contrast ratio for the device (assuming as in [1] that $\tau_{on} = 0.8$ or 80% of the peak $\tau_{on} = 1$) of 130:1. Similarly, a 1% spatial thickness variation (d/d = 0.01) results in a $\tau_{off} = 0.2465 \times 10^{-3}$ and a maximum contrast ratio of 3250:1.

From an interferometric optical path difference measurement of the LCLV in reflection readout, we found a one-way optical path difference of $\lambda/4$ for the LCLV in reflection readout. This is equivalent to a 5.25% thickness variation, a transmittance $\tau_{off} = 8.23 \times 10^{-3}$ and a maximum contrast ratio of 97:1. This is in excellent agreement with our observed 100:1 global contrast ratio for the LCLV. The observed 1500:1 local contrast ratio (Figure 3.3) is equivalent to a thickness variation of 1.48% over the 3mm diameter LC region used.

From these data, we conclude that the maximum global contrast ratio possible on the LCLV has yet to be reached and that achieving such performance requires fabrication of thin 2-3μm liquid crystal layers of more uniform thickness. Although devices with thicker LC layers will result in larger contrast ratios for a given percent ($\Delta d/d$) tolerance, such thicker layers result in an LCLV with far slower response. However, in cases when operation at 30 frames/sec is not required, thicker LC layers are appropriate and far larger contrast ratios than the presently obtainable 100:1 global values should easily be obtainable.

3.1 REFERENCES

1. W. Bleha, et.al., Opt. Eng., 17, 371-384 (1978).

2. J. Grinberg, et.al., Opt. Eng., 14, 217-225 (1975).

3. D. Casasent, Proc. IEEE, 65, 143-157 (1977).

4. M. Born and E. Wolf, Principles of Optics, 2nd Ed., Pergamon Press, New York (1970).

5. J. Grinberg, et.al., IEEE, ED-22, 775-783 (1975).

6. L. M. Fraas, et.al., J. Appl. Phys., 47, 576-583 (1976).

7. L. M. Fraas, et.al., J. Appl. Phys., 47, 584-590 (1976).

8. D. Casasent, S. Natu, Opt. Commun. (Submitted).

9. D. Casasent, Appl. Opt., (Submitted).

10. J. Grinberg, A. Jacobson, J. Opt. Soc. Amer., 66, 1003-1009 (1976).

11. P. McIntyre, A. Snyder, J. Opt. Soc. Amer., 68, 149-157 (1978).

12. J. Bigelow, R. Kashnow, Appl. Opt., 16, 2090-2096 (1979).
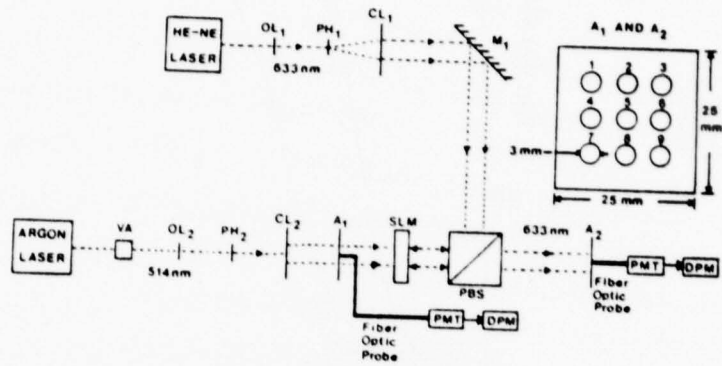
Figure 3.1 Sensitometry and Contrast Ratio Test System

Figure 3.2a

24
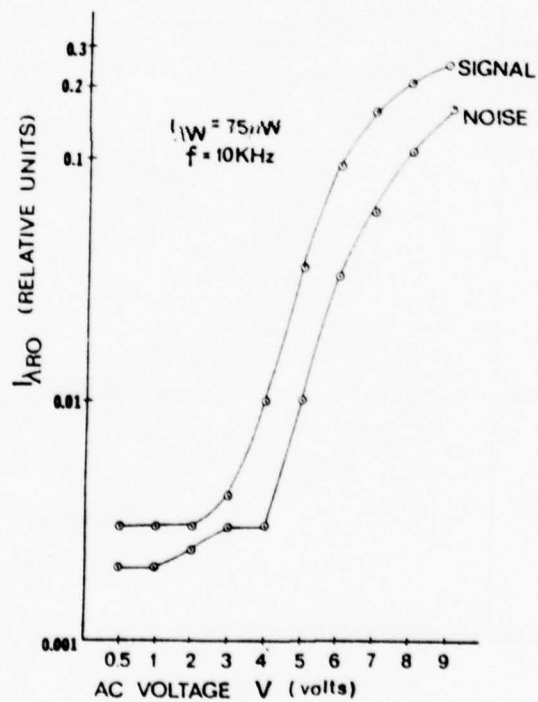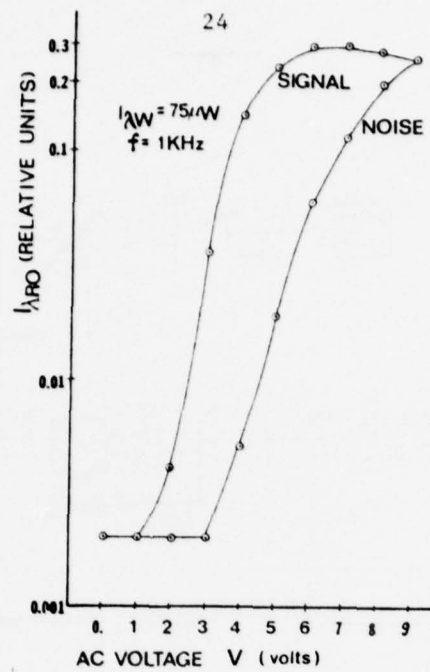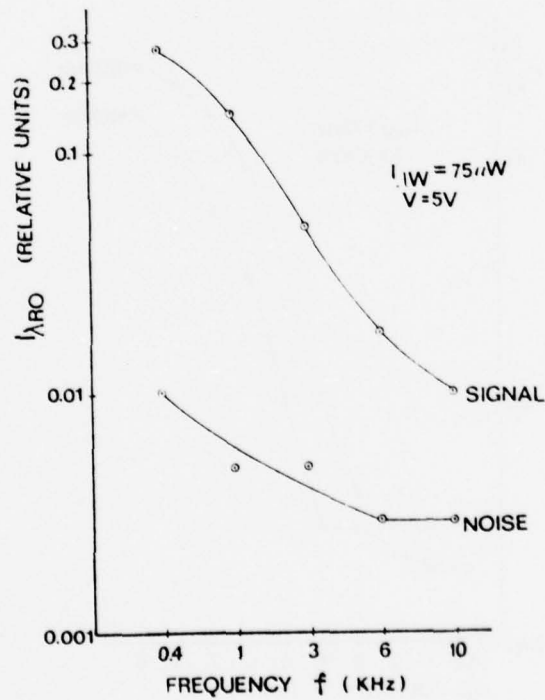
Figure 3.2b

Figure 3.2c

Signal and Noise for the LCLV (a) vs. V for f = 10 kHz,
(b) vs. V for f = 1 kHz and (c) vs. f for V = 5v
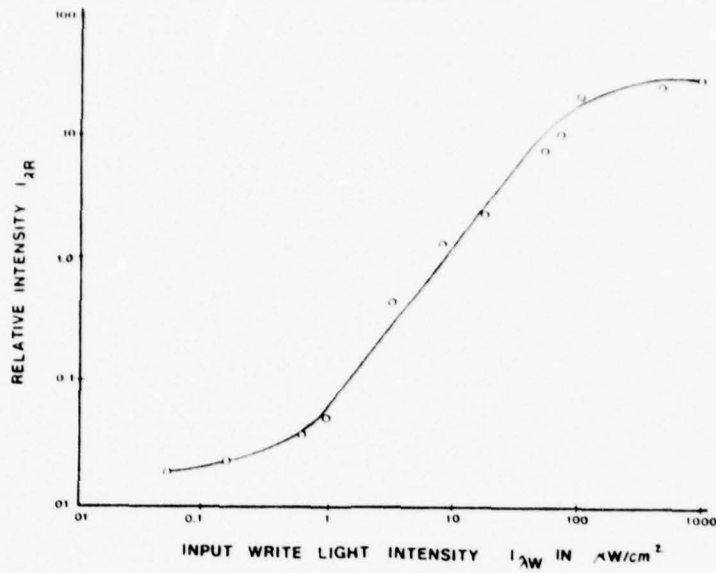
Figure 3.3 Local Sensitometry Curve for the LCLV (6v, 10 kHz) Showing
1500:1 Contrast Ratio and 30,000:1 Dynamic Range

3.2 SENSITOMETRY CONTROL OF A HYBRID FIELD-EFFECT LIQUID CRYSTAL LIGHT VALVE

Abstract

Sensitometry data are presented and analyzed for a hybrid, a.c., field-effect, liquid crystal light valve. The control voltage and its frequency are shown to change the transmission threshold, sensitivity, linear dynamic range and the shape of the device's sensitometry curve. These effects can be explained from an equivalent circuit of the device.

3.2.1 Introduction

The hybrid, field-effect, a.c., liquid crystal light valve (LCLV), manufactured by Hughes Research Corporation, has recently[1] emerged as one of the most viable spatial light modulators[2] for optical data processing. In this paper, we consider the results of a recent experimental investigation of the sensitometry of this LCLV. The first steps in the use of the LCLV are: to select its operating voltage V and a.c. frequency f, and to determine the bias level and useful range of input light intensity. The device's sensitometry curve (transmission τ vs. input write light intensity $I_{\lambda W}$) provides such data.

In Sections 3.2.2 and 3.2.3, we briefly review the model to be used for this device and discuss its τ expression. Experimental data on the effects that varying V and f have on τ, with fixed $I_{\lambda W}$, are included in Section 3.2.4. Sensitometry curves for various V and f values follow in Section 3.2.5.

3.2.2 LCLV Model

The LCLV consists of over 20 thin film layers. The major structural layers are the CdS photo-conductor, CdTe light blocking layer, dielectric mirror, and thin 2.74 μm thick liquid crystal (LC) layer sandwiched between two transparent indium-tin-oxide electrodes. The device is written on in λ_W light incident on the CdS side of

the structure and read in reflection at λ_R from the opposite side of the device with linearly polarized light and observed through a crossed analyzer.

The LCLV equivalent circuit we use was proposed by Fraas, et.al.[3,4], and is shown in Figure 3.4. The photo-activated CdS-CdTe charge storage diode[3] is modeled by R_3, D, C_3, and R_4. The input write light $I_{\lambda W}$ controls R_3 and C_3 (R_3 decreases and C_3 increases as $I_{\lambda W}$ increases). R_1, C_1, and C_2 model the LC layer and dielectric mirror. At low applied frequencies f, the photo-current through the CdS/CdTe layer is a series of high positive pulses (increasing in amplitude proportional to $I_{\lambda W}$) alternating with low negative leakage currents (of longer time duration). At very high frequencies, the photo-current approaches a sinewave. The effective voltage V_{LC} developed across the LC layer is proportional to the integrated current passing C_2.

3.2.3 On-State Model

In this a.c. LCLV, the molecules are initially aligned parallel to the electrode surfaces with a 45° twist present in the orientation of the LC molecules in the layers throughout the LC's thickness d. When V is present across the structure and write light $I_{\lambda W}$ is incident on the CdS, the LC molecules tilt normal to the LC's large faces and the uniform twist across LC molecular layers can be modeled as broken at the center of the LC layer. If we denote the polarization axis of the incident λ_R light as x, then the twist angle ϕ is the angle between the axis and the projection of the optical axis of the LC molecules on the plane of the entrance electrode. The tilt angle 0 (averaged over the thickness of the LC) is the angle between the z axis (along which the input λ_R light propagates) and the optical axis of the LC molecules. The transmission of this device is then given by[5]

$$\tau = \sin^2(2\phi)\,\sin^2(\delta/2) \ , \tag{1}$$

where

$$\delta = (2\pi d/\lambda)\Delta n(\vartheta) \tag{2}$$

is the phase difference introduced between the wave components. Only the second half of the LC layer is of importance in on-state transmission analysis.

The difference $\Delta n(\theta)$ between the two indices of refraction varies with θ, which in turn varies with V. If n_1 and n_2 are the indices of refraction (parallel and perpendicular) to the optic axis of the LC molecule, it can be shown that

$$\Delta n(\theta) = n_1 - n_2 / [\sin^2\theta + (n_2/n_1)^2 \cos^2\theta]^{\frac{1}{2}} \quad . \tag{3}$$

For small $\Delta n = n_1 - n_2$, this reduces to

$$\Delta n(\theta) = \Delta n \sin^2\theta(V) \quad , \tag{4}$$

from which the τ expression given in Reference [6] results

$$\tau = \sin^2(2\phi) \, \sin^2[(\pi d \Delta n/\lambda) \, \sin^2(\theta(V))] \quad . \tag{5}$$

We use this on-state τ vs. V expression and the LCLV equivalent circuit of Figure 3.4 to describe our sensitometry data.

3.2.4 V and f vs. τ for Fixed $I_{\lambda W}$

For our LCLV, $\phi = 45°$, $\sin^2(2\phi) = 1$, $\Delta n = 0.25$, $d = 2.74\mu m$ and $\lambda = 633nm$. From these values, and $\theta = 90°$ (for V=0) and $\theta = 0°$ (for large V), we find τ to vary from $\sin^2(194°)$ to $\sin^2(0°)$. Assuming V to vary linearly with θ, the τ vs. V for the device should track the $\sin^2\psi$ curve from $\psi = 194°$ to $0°$ as V increases from 0. Close inspection will show that such a curve first decreased slightly (as θ decreases from 194° to 180°) and then increases with a $\sin^2$ curve response. (Some reserachers have observed such a small dip in the $\tau - I_{\lambda W}$ curve for the LCLV at low V < 1 volt. These results are explainable from the above analysis.)

To obtain experimental data on the τ vs. V and f performance of the entire LCLV, the device was illuminated with a constant $I_{\lambda W} = 75\mu w/cm^2$ level as V across the entire structure was varied in 1 volt steps from 1 to 10 volts. For all V settings, f was varied in 10 steps from 0.4 to 10kHz. For each of these 100 pairs

of V and f settings, the relative reflected $I_{\lambda RO}$ reading (through crossed polarizers) was measured. This $I_{\lambda RO}$ value is a measure of τ. These data are shown in Figure 3.5. From these curves, we see that as f is increased, the τ vs. V curves shift and τ peaks at higher V values.

These results indicate that higher voltages are required across the LCLV at increased f to obtain the same output light observed at lower f settings. In addition, the slope of the τ vs. V curve is seen to decrease as f is increased. These results follow directly from the equivalent circuit of Figure 3.4 in which V_{LC} (the integrated photo-current) was shown to decrease as f was increased, thus indicating a poorer expected device sensitivity at higher f setting.

3.2.5 Sensitometry

In total, we produced over fifteen LCLV sensitometry curves at different V and f settings with $I_{\lambda W}$ varied from 0.01 to 3000μw/cm^2. Three such curves for the LCLV are shown in Figure 3.6 and for f = 10kHz and three different values of V applied across the entire device. Similar data are shown in Figure 3.6b for three different operating frequencies f with V = 4v. From the equivalent circuit of Figure 3.4 and Eq. (5), we expect V_{LC} to decrease as V is decreased or as f is increased. We thus anticipate poorer device sensitivity at low V levels (and high f levels), since higher $I_{\lambda W}$ levels will be required (at low V and high f settings) to achieve the same τ output obtained at larger V or lower f choices. The results shown in Figure 3.6a verify these results for the case of variations in V, whereas the data in Figure 3.6b confirms the predictions for the case of f variation. Both agree with the results obtained in Figure 3.5.

From Figure 3.6, we find considerable changes in the sensitometry curve for the various V and f choices. The (8v, 10Kz) and (4v, 1kHz) curves are similar to the classic published sensitometry curve[8] for this LCLV, which exhibits a knee at low $I_{\lambda W}$ values. From Figure 3.6, we see that operation at other V and f settings

result in a lower dynamic range for the device and at higher I_{W} levels (e.g., the 4v, 10kHz curve) or a larger and more linear device dynamic range (e.g., the 6v, 10kHz curve).

Fraas, et.al.[3,4], have analyzed the response of the CdS/CdTe layer and have observed no changes with f. However, they used much higher V levels than we did (at low V levels, some variations may be present in their experimental data). Our results (obtained for the entire LCLV device, not just the CdS-CdTe layers) show clearly the ability to control the shape of the LCLV's sensitometry curve by proper choice of V and f. Such control is of immense use: in adjusting the device's sensitivity and $I_{\lambda W}$ threshold for a given set of input data; in controlling the dynamic range and linear response region of the device; and of course, in controlling the shape of the sensitometry curve. Such shape control is of use in optical A/D converters[7] and other applications as well.

One of the more obvious applications of such control is the achievement of contrast reversal of an image recorded on the LCLV by varying the voltage or frequency across the device[8]. In Figure 3.7, we show the sensitometry curve for the LCLV at 8V and 1kHz. In this curve, $I_{\lambda W}$ levels above $1\mu w/cm^2$ in the input image will be contrast reversed. In practice, the control V across the device would be varied to effect such response. However, for the LCLV unit we considered higher voltages (of 20V or so) and low frequencies were needed to effect a contrast reversal over the same input $I_{\lambda W}$ image range without the contrast ratio loss apparent in Figure 3.7. The use of higher voltages (for contrast reversal with improved dynamic range) and lower frequencies (to enhance sensitivity) follow from our $\sin^2$ analysis and extrapolation of the curves in Figure 3.6.

3.2 REFERENCES

1. W. Bleha, et.al., Opt. Engr., 17, 371 (1978).

2. D. Casasent, Proc. IEEE, 65, 143 (1977).

3. L. M. Fraas, et.al., J. Appl. Phys., 47, 576 (1976).

4. L. M. Fraas, et.al., J. Appl. Phys., 47, 584 (1976).

5. M. Born and E. Wolf, Principles of Optics, 2nd Ed., Pergammon Press, New York (1970).

6. J. Grinberg, et.al., IEEE, ED-22, 775 (1975).

7. A. Armand, et.al., Proc. IOCC Conf., London (September 1978).

8. J. Grinberg, et.al., Opt. Engr., 14, 217 (1975).
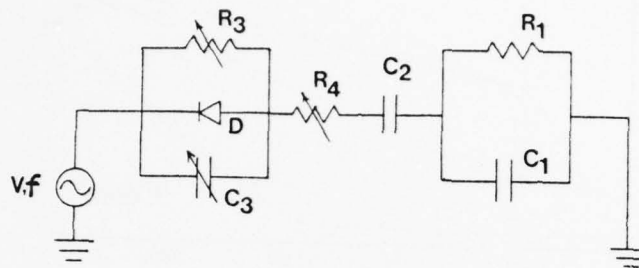
Figure 3.4 Equivalent Circuit for the a.c. LCLV
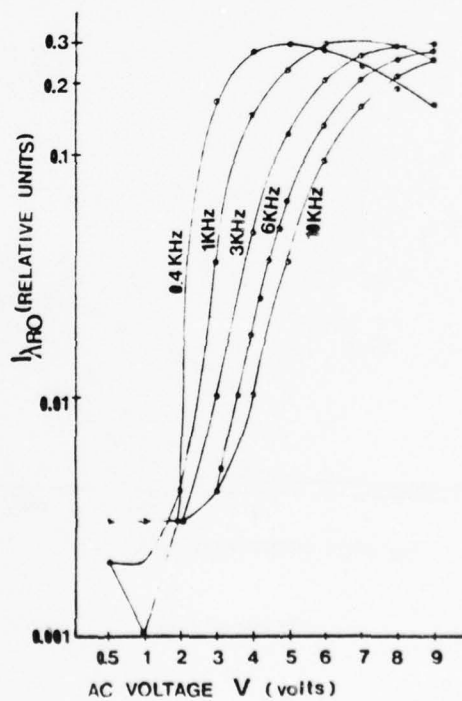
Figure 3.5 Relative Reflected Read Light $I_{\lambda RO}$ (Through Crossed Polarizers)
vs. V across the LCLV (for different a.c. Frequencies f)

34
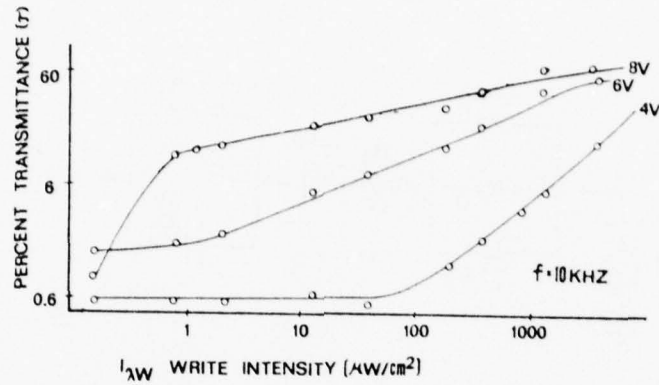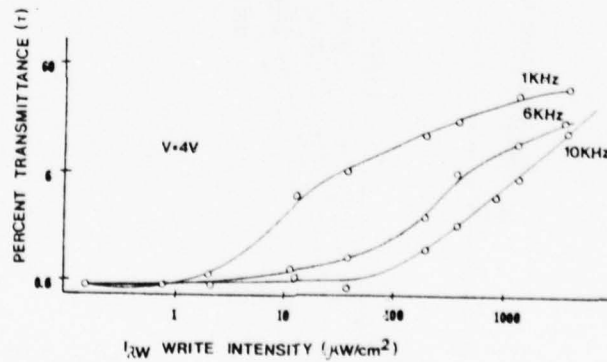
Figure 3.6a

Figure 3.6b

Figure 3.6 Sensitometry Curves for the LCLV (a) at 10kHz and Selected Voltages
Across the Device, (b) at 4v and Selected a.c. Frequencies
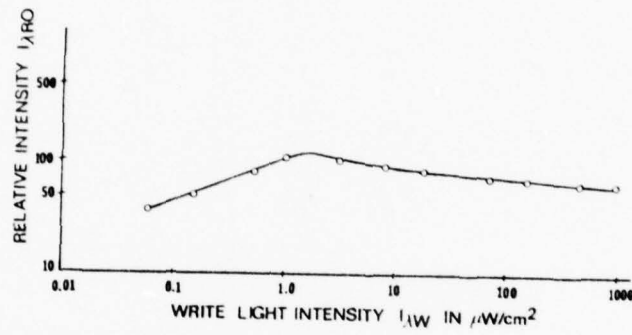
Figure 3.7   Sensitometry Curve for the LCLV Showing Contrast Reversal

4. PHOTO-DKDP EXPERIMENTAL TEST PROGRAM

In this Section, we review our experimental test and evaluation program on the photo-DKDP SLM. A wealth of experimental image reconstruction, contrast reversal, addition, subtraction, plus real-time optical text and aerial image correlation data obtained on this real-time optical transducer are included separately in Chapter 5.

4.1 Introduction

The photo-DKDP SLM [4.1-4.4] is manufactured by LEP in France. They have purchased the entire soft crystal growth facilities, equipment, and DKDP stock of the two prime United States manufacturers of similar DKDP face plates. Many U.S. companies and government facilities have fabricated electron beam address DKDP SLMs over recent years. However, none has reached the maturity of a product that the French electron beam addressed DKDP SLM has. The photo-DKDP SLM that we have investigated in the course of this program is similarly a most matured and engineered SLM. There is no comparable U.S. SLM available. The photo-DKDP unit we have is (to our knowledge) the only one in the U.S.. It is one of the most promising real-time and reusable SLMs, and thus deserves far more extensive test and evaluation (as well as the fabrication of a U.S. version of this device) than this present program has permitted.

In Section 4.2, we describe the fabrication and detail the layers of the device, the operation of the device, as well as the extensive electronic support systems (voltage control, vacuum support system, Peltier cell cooling system, electronic write, read and erase light intensity and time duration systems, as well as synchronization and control circuitry) that we had to fabricate to permit use of and testing of this SLM. The four SLM parameters with which we were most concerned were: sensitometry, write, read and erase operation; resolution; and noise. In Section 4.3, we describe our sensitometry data collection system. In our analysis

of this data, we conclude the write light λ_W sensitometry, the degradation effects of readout light λ_R, the efficiency of erase light λ_E, and hence the entire write, read and erase sequential operation of the device. We include our observed field dependent photo-sensitivity of the Se photo-conductor used in this device. We also note why this observation means that the dynamic data for this SLM will be superior to static data. We also note the effect that this field dependent photo-sensitivity has on interframe operation, such as image addition and subtraction, and we suggest and describe how this effect can be reduced by proper doping of the SLM and controlling its $\mu\tau$ product. In Section 4.4, we include our experimental data on readout and erase light effects. Specifically, we consider the erasure and image degradation effects of readout light λ_R, as well as the efficiency and operation of erasure with λ_E light itself.

In Section 4.5, we consider five resolution experiments performed on the photo-DKDP SLM. These include; imaging, transmission and reflection MTF; linear and non-linear interferometric MTF; as well as edge response MTF test data. The interferometric MTF test procedure is clearly the most attractive and reproducible MTF data acquisition technique. For the photo-DKDP (because of the thin photo-conductor layer), it is also a valid experimental MTF test procedure. We then compare the various MTF data to the theoretically predicted results. Excellent agreement was obtained in this comparison of theory and experiment. In Section 4.6, we discuss the issue of noise in this SLM with attention to the three types of noise: scatter, interharmonic, and phase noise. Test procedures to be used to obtain data on each of these noise sources, as well as quantitative results obtained for each on the photo-DKDP SLM, are included. Brief remarks are then advanced on the relevance of these tests to various SLM applications, as well as on the test equipment to be used.

4.2 The Photo-DKDP

4.2.1 Device Construction

A schematic of the photo-DKDP SLM is shown in Figure 4.1. A photograph of the device is included in Figure 4.2. Details of the various layers comprising this SLM follow.

(a) The SiO_2 readout window has a three degree wedge angle. This was included so that the reflections from the device will appear at six degrees, thus minimizing their effects.

(b) Electrode 1 is a gold electrode.

(c) The Se photo-conductor is deposited with a thickness of about 12μm (10-12μm is normal) with n = 2.8 at 630nm and with ε = 6.

(d) The nine layer dielectric mirror M consists of $\lambda/4$ layers of CaF_2 and ZnS. It is deposited by vacuum techniques. Its measured reflectance at 633nm is 0.985 with respect to air and 0.96 with respect to Se. Its transmittance was likewise measured to be one percent at 633nm and from 70-90 percent below 500nm.

(e) The DKDP crystal itself is wedged. Its thickness linearly varies from 320μm to 0μm over its 35mm width. For $T - T_C \leq 0.5$ degrees (where T_C is the Curie temperature of the crystal), ε_C = 650 and $V_{\frac{1}{2}}$ = 300v at the nominal readout wavelength of 630nm.

(f) The second electrode is In_2O_3 with a transmittance T = 0.98, a reflectance R = 0.01 and an absorption A = 0.01 at 630nm.

(g) The CaF (florite) substrate is also wedged with a thickness varying from 6μm to 4.7μm. This corresponds to a $1^030' \pm 5'$ wedge angle for this substrate.

Geographic differences and other related items have affected our test and evaluation program on this SLM. Lack of adequate device documentation greatly affected our program, also and most especially the analysis of our resultant data. However, this SLM appears to be so superior and well engineered (compared to alternate U.S. SLMs), that the associated frustration of such a research program appeared to be warranted. Once again, the importance of total and

Signal and Noise for the LCLV (a) vs. V for f = 10 kHz,

(b) vs. V for f = 1 kHz and (c) vs. f for V = 5v
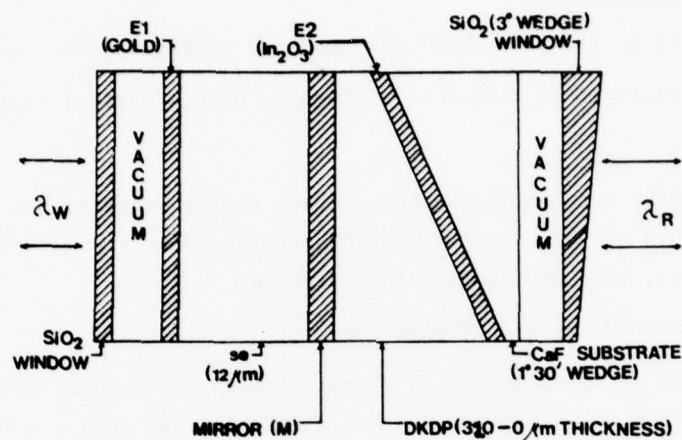
Figure 4.1   Schematic Diagram Showing the Layers of the Photo-DKDP SLM
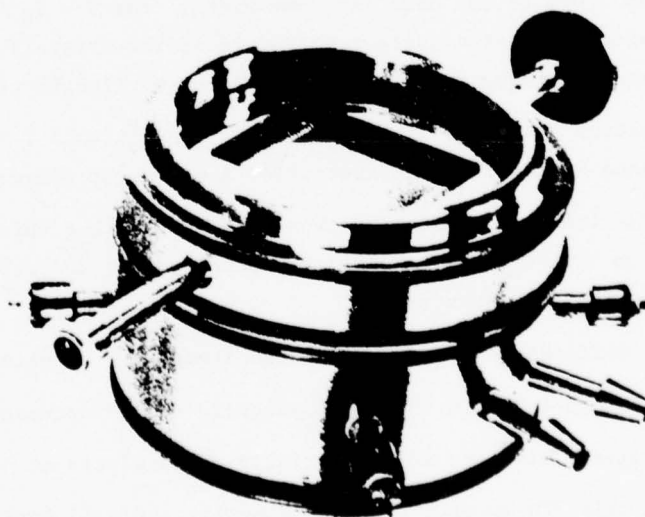
Figure 4.2   Photograph of the Photo-DKDP SLM

detailed documentation of device specifications and prior test performance on such SLMs is vital. Otherwise, constant repetitive tests are necessary by all researchers who choose to consider utilization of such a device. These latter remarks apply in general to all SLMs and all U.S. or foreign SLMs.

4.2.2 Temperature and Electro-Optic Operation

This SLM is operated at the transition temperature T_C of the active photo-DKDP crystal media (about -52°C). A set of Peltier cells around the edges of the structure provide the necessary cooling for the device. The entire device is enclosed in a vacuum housing. The operation at approximately -52°C is necessary so that a long storage time and improved device resolution with lower required device voltages, as well as resolution and storage performance improvements result. These results are most easily realized for this device when it is operated in reflection readout from the DKDP side of the SLM with readout light at λ_R = 633nm. Linearly polarized readout light must be used with this device.

The direction of polarization y of the readout light for this device is also of concern. It should be polarized at 45° with respect to the crystal's induced (x' and y') electro-optic axes for optimum results. A crossed output polarizer (in the reflected λ_R beam) is used to achieve these performance results. In this case, the output I_0 and input I_i light intensities are related to the voltage V across the photo-DKDP layer by [4.5]

$$I_0 = I_i \sin^2[(V/V_{\frac{1}{2}}) \ (\pi)] \ . \tag{4.1}$$

In Equation (4.1), the voltage $V_{\frac{1}{2}}$ is the crystal's half-wave voltage. Other modes of operation are also possible for this SLM. If y is oriented along y' or x', and if the crossed output polarizer is omitted, pure phase modulation results. With y at ±45° to x' and y', amplitude modulation occurs. If an optical bias is added externally, it is possible to obtain a contrast reversed output plane pattern.

42

From Equation (4.1), we see that $\tau = I_0/I_i$ varies spatially with the voltage $V(x,y)$ applied spatially across the DKDP layer. The spatially varying $I_{\lambda W}$ light distribution incident on the Se photo-conductor produces a corresponding spatial voltage distribution $V(x,y)$ across the DKDP layer itself.

4.2.3 DKDP Support Systems

The value of the voltage present across the DKDP SLM and its polarity must be controlled together with the wavelength of the write (λ_W), read (λ_R) and erase (λ_E) light during cyclic operation of this device. This is especially true during image addition and subtraction and contrast reversal operations on the device. The actual voltage level and its polarity necessary are considered later. For now, we simply note that a given voltage and polarity across the electrodes are necessary and that these values must be applied simultaneously with the presence of write, read, or erase light itself.

All DKDP support systems had to be fabricated separately. Funds for such efforts were not available, thus many concessions were necessary in fabrication of the support electronic system that was finally chosen. The five major support systems that had to be fabricated before test and evaluation of this SLM could proceed were:

(1) An electronic voltage and polarity control system.

(2) A light intensity level control system to permit control of the intensities $I_{\lambda W}$, $I_{\lambda R}$, and $I_{\lambda E}$ or the write, read, and erase light beams respectively, as well as the durations T_W, T_R, and T_E of each of these modes of operation.

(3) Synchronization and control of the voltage and light level systems in (1) and (2), specifically the write, read, and erase modes of operation.

(4) Fabrication of the vacuum support system for the device. This included a one month search for and subsequent independent fabrication of several flange and valve connections for the device (no equivalent U.S. part could be located for this European component).

43

(5) Fabrication of an electronic drive system for the Peltier
cooling system. This included a temperature control, as well
as a temperature sensor and measurement system.

The support system for the photo-DKDP light valve is far more complex than the
simple AC voltage required for the LCLV. Operation of the device is complicated by
the need for separate write, read, and erase light sources and the need to cool the
device to about -52°C for optimum performance and to maintain the device in a
vacuum.

The vacuum system used for the photo-DKDP consists of an absolute pump. This
system maintains an 8 m-torr pressure in the DKDP chamber. It requires monitoring
every hour and the addition of liquid nitrogen to the roughing pump every two
hours.

The cooling system used to maintain the DKDP at its operating temperature
consists of four dual Peltier cells (one on each of the large edges of the crystal)
and circulating water flow as a first stage cooling system and for the dissipation
of heat generated by the cells. The water flow should be at a steady rate of
one liter/minute. A flow switch is on order and will be used to regulate this
water flow.

For now, the adjustment is manual and requires monitoring every five minutes.
The present water flow is not steady and may be the cause of operations that cause
difficulty in interferometric tests on this SLM. A better crystal holder that
places less stress on the crystal housing, one that is more rigid and that has
adequate micrometer positioning controls should be designed and fabricated at a
later date.

The current for the Peltier cell cooling system originates from a 10amp/20v
supply. The present water flow system cannot dissipate the heat generated if the
Peltier cells are rapidly cooled. Thus, a slow cool-down rate 4amps/9v is presently
being used. The DKDP crystal's temperature is presently monitored by a platinum
resistance thermometer in an open loop system. This system also had to be designed,

the entire structure was varied in 1 volt steps from 1 to 10 volts. For all V
settings, f was varied in 10 steps from 0.4 to 10kHz. For each of these 100 pairs

fabricated, implemented, debugged, and calibrated. Because of the steep rate of
change of the longitudinal component of the dielectric constant with temperature
near the Curie point of the crystal, the crystal's temperature must be maintained
with 1°C of T_C. This requires almost constant manual monitoring and adjustment of
the Peltier cell cooling system. A closed loop feedback system for the unit
should be designed and fabricated if continuing tests are to be performed.

A mercury arc lamp (300watts) and an argon laser are used as the write light
sources during all experiments, a helium neon laser (50mW) is used as the read
source and a flash lamp assembly with a xenon flash tube (5watts) serves as the
erase source for our experiments. The control voltage across the crystal is
continuously variable from ±150v with electronic shutters S_1 and S_2 in the λ_W and
λ_R beams synchronized to the voltage control unit. When S_1 is opened, a voltage
is applied across the crystal. When S_1 is closed, V = 0 is applied across the
crystal. The erase circuitry is controlled by a manual unit that allows one to
flood the crystal when V = 0 is present across the unit (in effect we write a
uniform 0v pattern across the crystal during erasure).

4.3 Sensitometry

4.3.1 Carrier Effects

The major layers in the photo-DKDP SLM are shown in Figure 4.3. The voltage
levels and polarities to be applied between electrodes (E_1 and E_2) in the various
write (W), read (R), erase (E), and subtract (S) modes of operation are shown in
the figure. The λ_W and λ_R beams and the polarization of the incident and reflected
λ_R lightwaves are also included. For simplicity, separate input (P_1) and output (P_2)
polarizers and a beam splitter (BS) are shown. In practice, a polarizing beam
splitter (PBS) cube is used on readout to provide the plane λ_R incident polarization
and the crossed output polarization.

When λ_W light is incident of the Se, hole and electrons pairs are generated
in a thin layer of the Se near E_1. If E_1 is positive during the λ_W exposure, the

45
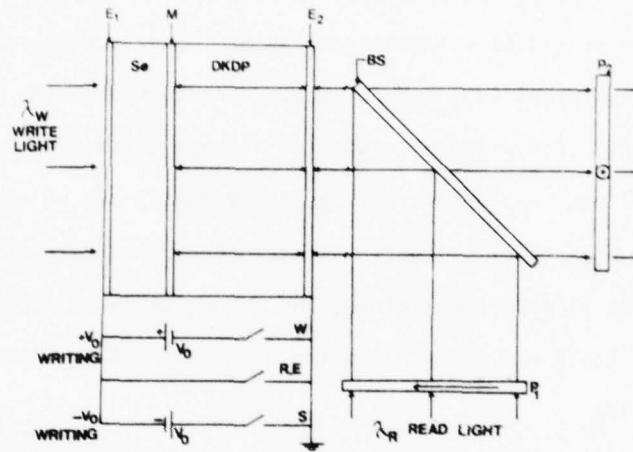
Figure 4.3 Voltage Polarities used for Write, Read, Erase, and Storage on
Photo-DKDP

photo-generated holes in the Se drift to the mirror M interface and the photo-generated electrons combine at E_1. The accumulated positive charge on M is proportional to $I_{\lambda W}$. If $I_{\lambda W}$ varies spatially, so does the charge density at M. These charges are stored in surface traps at M. Thus, the $I_{\lambda W}$ input light distribution has been converted to a latent charge distribution on M. With $E_2 = 0v$, this charge distribution produces a spatial voltage distribution across the DKDP. By the Pockels effect [4.5], this voltage distribution can be converted to a spatial modulation of the $I_{\lambda R}$ light. With crossed polarizers and the polarization of $I_{\lambda R}$ chosen as described before, the output image is a positive version (in λ_R light) of the input pattern written on the Se (in λ_W light) if E_1 is positive during writing.

If E_1 is negative during writing, the photo-generated electrons in the Se determine conduction and the latent charge pattern. Thus, now electrons drift to the mirror M where a negative charge distribution is produced. A combination of positive writing with holes and negative writing with electrons can be used to subtract one input image from the latent stored charge distribution of a prior image.

4.3.2 Charge Carrier Discription

To analyze sensitometry, readout, and erase data, we found it necessary to formulate a description of the photo-DKDP device operation in terms of charge carriers. Such a description and discussion of this SLM has not been previously provided and in fact the applied voltage polarities in many papers describing this SLM are conflicting. Thus, in this one Subsection, we include a complete charge carrier description of various write, read, and erase modes of operation of this device.

In Figures 4.4 and 4.5, we show the voltage distribution (vertical) vs. distance (horizontal) across the various device layers for the four different states of device operation. Figure 4.4a shows the initial device state (with no λ_W light).

In Figure 4.4b, we show the voltage distribution after writing for both bright (BR) and dark (DK) areas of the device (i.e., areas of the device illuminated and not illuminated during writing). For readout, $V_0 = 0$ and the device is illuminated from the right (DKDP side) with λ_R light (as in Figure 4.4c). For erasure, the device is illuminated from the left (Se side) with λ_E light (as in Figure 4.4d).

Most of the applied V_0 appears across the photo-conductor and little across the DKDP for both the $+V_0$ and $-V_0$ writing cases. We consider the $+V_0$ case first (Figure 4.4). When the Se photo-conductor is illuminated with λ_W light, hole and electron charge carriers are generated. With $E_1 = +V_0$, the holes conduct and move to the mirror M. This increases the voltage at M and likewise increases the voltage drop across the DKDP in the illuminated (BR) areas. The electrodes E_1 and E_2 are now shorted ($V_0 = 0$). The voltage distributions shown in Figure C now results and a large $+V_1$ is present across the DKDP (the mirror is positive with respect to E_2) in bright areas. A smaller $+V_2$ is present across the DKDP in dark areas. Thus, the phase retardation (or polarization rotation) introduced into the linearly polarized λ_R light beam is larger in the bright areas than in the dark areas. With crossed output polarizers, a positive output image results (areas illuminated during writing are also bright upon readout). Because of M and since Se is insensitive to λ_R light, no new photo-carriers are generated by the readout process, and thus (to first-order) no degradation occurs due to readout. For erasure, the Se side of the SLM is flooded with λ_E light (usually in the same spectral range as the λ_W light). This process generates holes and electrons in the Se. The holes trapped at M can now migrate back to E_1, equivalently electrons can migrate from E_1 to M, reducing the positive voltage V_1 at M and removing the positive charge stored at M.

Writing with $-V_0$ (Figure 4.5) present on E_1 is somewhat similar, except now electrons migrate to M during writing. This reduces the voltage at M and during readout M is negative. As before, a larger voltage is present across the DKDP in illuminated regions compared to dark areas with M now negative with respect to E_2.

48

(a) $+V_O$ $(I_{\lambda W}=0)$

(b) $+V_O$ (WRITE)

(c) $V_O=0$ (READOUT)

(d) $V_O=0$ (ERASURE)
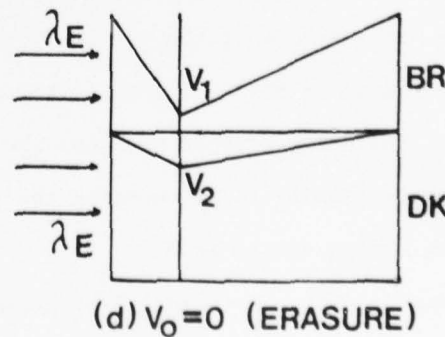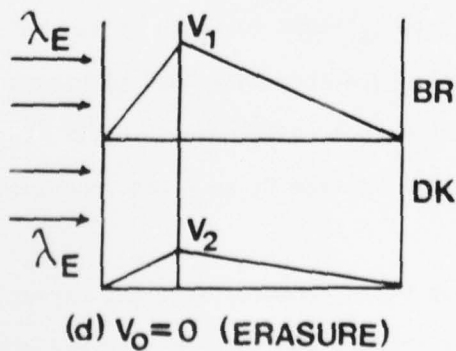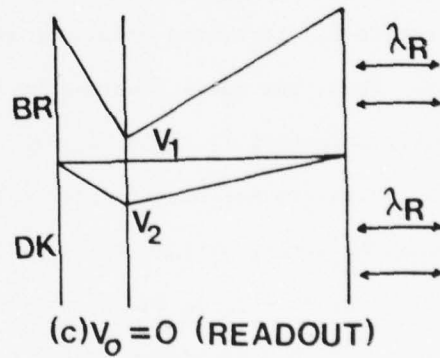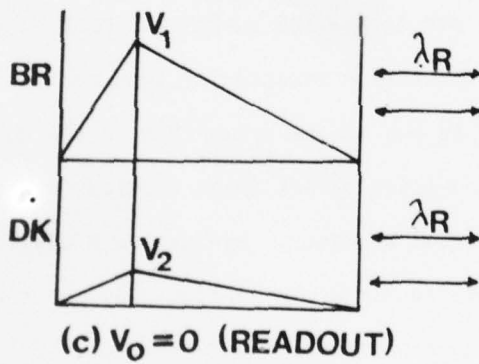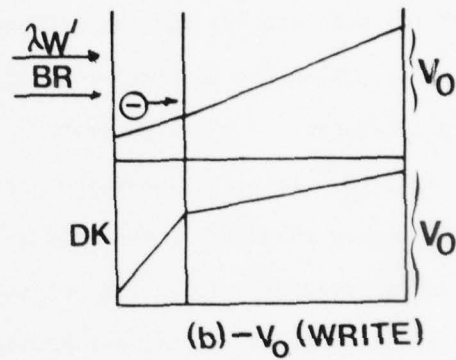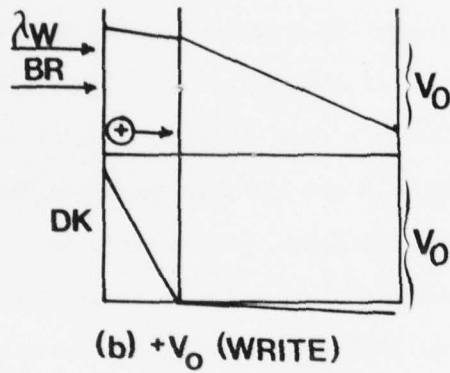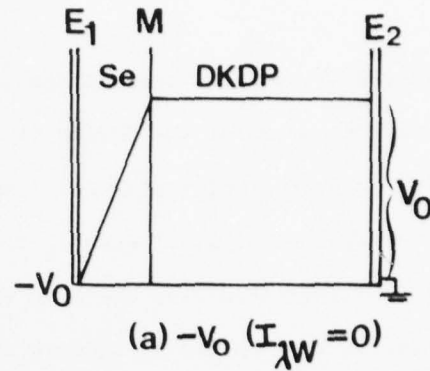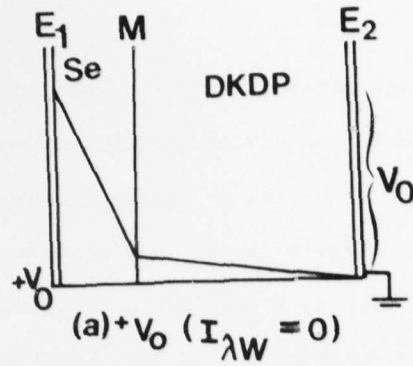
Figure 4.4 Voltage Distribution in the
Photo-DKDP for $+V_0$ (Positive
Writing) Operation

(a) $-V_O$ $(I_{\lambda W}=0)$

(b) $-V_O$ (WRITE)

(c) $V_O=0$ (READOUT)

(d) $V_O=0$ (ERASURE)

Figure 4.5 Voltage Distribution in the
Photo-DKDP for $-V_0$ (Negative
Writing) Operation

In erasure (Figure d), the holes, photo-generated in the Se near E_1, now migrate to M to remove the negative voltage (charge) stored there. Equivalently, electrons at M may now migrate to E_1 and recombine with holes. These processes result in a reduction to 0 of the charge stored or trapped at M.

In subsequent Sections, we will use Figures 4.4 and 4.5 and similar ones to describe our resultant data. For now, we only note that in positive writing ($+V_0$ applied, E_1 positive), writing is by hole conduction. Conversely, in negative writing, conduction is by electron flow. In erasure, electrons migrate from E_1 to M for positive writing and holes migrate for negative writing. Our concern is with the fact that the hole conduction is better than electron conduction in Se and that the conduction efficiency is a function of the field across the Se. From Figures 4.4 and 4.5, we clearly see that these two issues will greatly effect the performance of this SLM. These latter issues are described in greater detail in subsequent Sections.

Because of the long storage time of this SLM, an active erase mechanism is needed to realize fast cycle times. Erasure of a latent charge image is accomplished by flooding the Se with λ_E light with the electrodes E_1 and E_2 shorted as in curves b of Figure 4.4. The λ_E illumination (broadband or narrowband λ_W light) again generates electron-hole pairs in the Se. This decreases the resistivity of the Se which can increase the migration of the holes trapped at M. Recombination and migration of the photo-generated carriers can also contribute to the erase process. The photo-sensitivity of Se improves with larger voltages present across the Se and this implies that a non-zero E_1 level is preferrable for erasure. However, as in the discussion of optimum readout voltage conditions, attention to dark regions indicates that zero voltage across the SLM is preferrable. In practice, a situation where a positive or negative voltage was applied for some fraction of the readout or erase time may be optimum but would be too dependent on the recorded image pattern to allow definitive conclusions to be made.

In subsequent studies, we will consider the above carrier processes in more depth. From these studies, new results have emerged concerning the photo-sensitivity of the photo-DKDP SLM, the device's dark storage, erasure, and its ability to add, subtract, and contrast reverse data.

From Figure 4.4, the storage of the latent charge image at M (in bright areas) is generally better with positive or negative voltage present on E_1. However, considering the entire SLM (specifically the dark regions, as well as coupling between light and dark regions), major attention must be given to dark areas when determining the optimum voltage polarity to be placed across the device during readout. It may appear that E_1 should be negative (for positive writing) or positive (for negative writing) and not 0v during readout to achieve best contrast (i.e., 0v across the DKDP in the dark regions). However, changing the voltage across the DKDP by a small amount requires a large voltage applied to E_1, this will result in a large voltage drop (field) across the Se (in dark regions). Then, during readout, the light leaking through M will be very efficient in carrier generation and photo-conduction in Se. This will result in an increase in the voltage across the DKDP in dark regions. This will increase dark transmittance and decrease overall device contrast. Thus, with $E_1 = 0$ in readout, the reduced voltage drop across the Se reduces degrading readout light effects in dark regions. Thus, by devoting attention to dark regions and practical effects, such as M leakage of λ_R light and the voltage dependent sensitometry of the Se, we find that $E_1 = 0v$ seem to be the preferrable readout operating condition, rather than E_1 positive or negative.

4.3.3 Sensitometry Data

The test system used to determine the sensitometry curve for the photo-DKDP light valve is shown in Figure 4.6. The components used are listed in Table 4.1. The write and reflected readout light (through crossed polarizers) intensities were measured by a photo-diode, connected to an operational amplifier and a digital
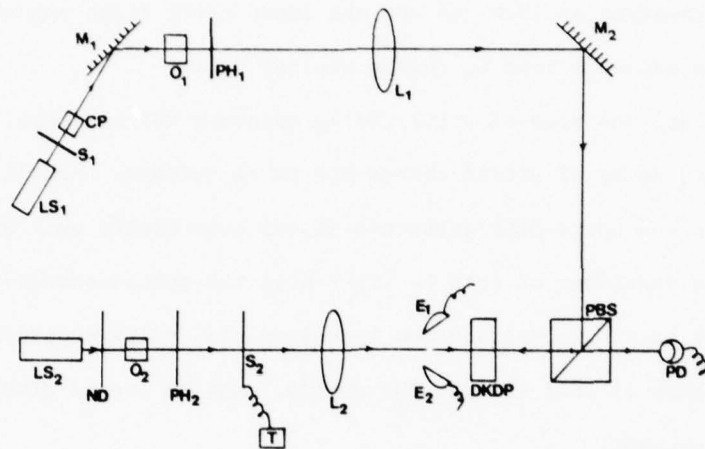
Figure 4.6   Sensitometry Data Acquisition System

Table 4.1   Components used in the Sensitometry Data Acquisition System of
Figure 4.6

LS$_1$:   633nm laser

LS$_2$:   514nm laser

M$_1$ & M$_2$:   Metallized NRC "2" mirrors

CP: Calcite polarizer

O$_1$:   Jondon 20X objective

O$_2$:   Jondon 5X objective

PH$_1$:   10 μ pinhole

PH$_2$:   5 μ pinhole

E$_1$E$_2$:   Erasing flashes

S$_1$:   Shutter for read light

S$_2$ & T: Shutter with electronic
timer (Vincent Associates)

ND: 10% neutral density filter

PD: Photodiode (United Technology)

PBS: Polarizing beam splitter cube

voltmeter. This raw voltage data is then converted into $\mu W/cm^2$ using appropriate amplifier gain and diode senistivity factors. During sensitometry data collection, $I_{\lambda W}$ was held constant at $18\mu W/cm^2$ and the input write light exposure was controlled by varying the exposure time T_W (using shutter S_1).

The λ_R light was blocked until the λ_W exposure was complete. This reduced the degradation and decay of stored charge due to λ_R readout. Recall that the dielectric mirror in the photo-DKDP structure of our unit blocks only about 50% of the λ_R light. The remainder of this λ_R light hits the photo-conductor (which is sensitive to 633nm) causing a degradation in the spatial voltage distribution across the crystal. Because of this effect, the crystal must be erased after each exposure and $I_{\lambda RO}$ measurement.

The sensitometry data for both +150v (Se electrode E_1 positive) and -150v across the SLM with the DKDP side of the SLM assembly always at zero volts are shown in Figures 4.7a and 4.7b. An $I_{\lambda R} = 20\mu W$ light level was used to reduce any degrading effects of λ_R readout on the stored charge distribution.

From these data, we note that the sensitivity of the device is better for +150v writing than for -150v writing (because of the higher efficiency, $\mu\tau$ product and photo-generation for holes than for electrons). The threshold $E_{\lambda WT}$ at which the device responds is about $0.5\mu J/cm^2$ for both polarities of applied voltage. However, the write exposure required to reach 80% of saturation is $E_{W0.8S+} = 75\mu J/cm^2$ for +150v writing and a much larger $E_{W0.8S-} = 290\mu J/cm^2$ value for -150v writing. The write exposure required for full saturation in the two cases was similarly less ($E_{WS+} = 560\mu J/cm^2$) for 150v writing than for -150v writing ($E_{WS-} = 1150\mu J/cm^2$).

4.3.4 Se Photo-Conductor Considerations (E_1 Polarity)

The photo-conductor properties of the amorphous Se photo-conductor used in the photo-DKDP SLM differ significantly from those of CdS and similar photo-conductors used in the LCLV and other SLMs. CdS photo-conductors cannot be deposited on photo-DKDP because of the high deposition or annealing temperature necessary in CdS to
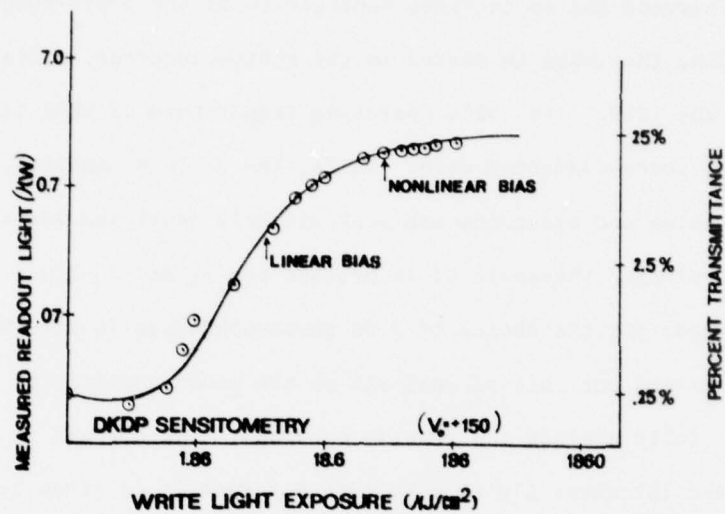
Figure 4.7a Photo-DKDP Sensitometry Data with $+V_0$ Applied (E_1 Positive)
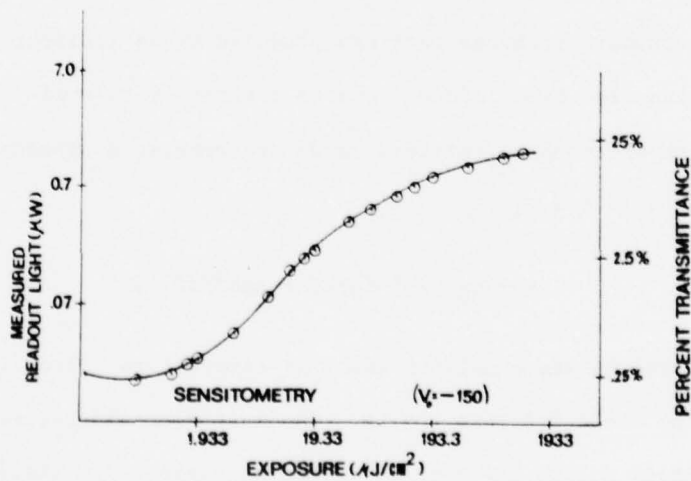
Figure 4.7b Photo-DKDP Sensitometry Data with $-V_0$ Applied (E_1 Negative)

reduce dark current and to increase sensitivity of the photo-conductor. In the photo-DKDP SLM, the image is stored in the photo-conductor. This is contrary to the case in the LCLV. The $-52°C$ operating temperature of DKDP also effects the choice of the photo-conductor used. In Se, the $\mu\tau$ (μ = mobility, τ = lifetime) product for holes and electrons are approximately equal and large, even at $-50°C$. The sharp wavelength threshold of Se between the λ_R and λ_W light used is the fifth and final reason for the choice of a Se photo-conductor in this SLM.

We now extend our initial analysis of the photo-sensitivity of Se. This is necessary to fully explain the results obtained. The current in a material of mobility μ and thickness L with a voltage V across it is given by

$$\frac{dq}{dt} = \frac{N(t)e\mu V}{L^2} , \qquad (4.2)$$

where e is the charge of a carrier and N(t) is the number of drifting carriers. We describe N(t) by

$$N(t) = N_0 \exp(-t/\tau_m) , \qquad (4.3)$$

where N_0 is the number of charge carriers produced by an incident <u>pulse</u> of light and τ_m is the mean free time before a charge carrier is trapped. The quantum efficiency η with which photo-carriers in Se are generated depends upon the field E across the Se as [4.6-4.7]

$$\eta = \eta_0 \exp[-E_0/kT + B_0 E^{\frac{1}{2}}/dT] , \qquad (4.4)$$

where η_0 and b_0 and E_0 are constants and T is temperature. From (4.4), we see that η varies with the field E across the Se. The initial field across the Se is approximately 100v across a 10µm layer or 10^5v/cm. At these large field levels, η is initially approximately 20%. However, during exposure to the writing pattern, the voltage across the Se decreases and that across the DKDP layer increases. This means that during long exposures, photo-electric conversion in Se will be better

for the initial part of the exposure (a large field is present across the Se then) than for the latter part of the exposure (when a lower field is now present across the Se).

Next, we consider the efficiency with which a spatial charge pattern will be transferred across the bulk of the Se layer. This efficiency is proportional to

$$R = \tau/t_r , \qquad (4.5)$$

where τ is the lifetime and t_r is the transit time of the charge carriers. Since transit time is proportional to the thickness d of the Se divided by the drift velocity

$$v = \mu V/d , \qquad (4.6)$$

we find

$$t_r = d^2/\mu V . \qquad (4.7)$$

For d = 10μm, we find t_r = 10μsec for holes and a far larger 50μsec value for electrons. R and hence the transfer efficiency across the bulk of the Se layer is thus

$$R = \tau/t_r = \mu\tau(V/d^2) . \qquad (4.8)$$

From (4.8), we see that R increases with V, decreases with d, and is proportional to the $\mu\tau$ product of the carrier.

For times larger than the transit time, then charge q is accumulated as

$$q = (N_0 eV\mu\tau/L^2) \ [1-\exp(-t/\tau)] . \qquad (4.9)$$

The exponential term is 0 for large t and q is proportional to $\mu\tau$. This $\mu\tau$ product for holes is $1.3 \times 10^{-6} cm^2/V$, whereas, for electrons it is less ($3.2 \times 10^{-7} cm^2/V$) by a factor of 4.06. From this, we expect holes to be more efficient than electrons

during writing. Thus, we expect positive writing (E_1 = positive, Se positive) to produce better results than negative writing. The data of Figures 4.7a and b confirm these results. In the low (0.3sec) exposure range, we find a difference of 4:1 in sensitivity between positive and negative writing. At longer exposures, we find a lower difference factor (approximately 3). This indicates that the quantum efficiency η and the μτ product are simultaneously field, as well as carrier dependent and that the difference in writing efficiency for holes (positive writing) and electrons (negative writing) is less for longer exposures.

The consequences of these observations (that hole writing is more efficient than electron writing and the field dependence of the photo-sensitivity of the Se photo-conductor) are that dynamic writing (with low duration pulses) will yield better sensitometry data than will long exposures. For applications such as image addition or subtraction, the field dependent sensitometry of Se will require alternate μτ products than presently exist. This will enable addition and subtraction operations to be readily performed.

Dumont, et.al., [4.8] imply that the sensitometry for holes and electrons are approximately equal. However, as our data of Figure 4.7 and the above analysis demonstrats, hole writing ($+V_0$) is approximately four times more efficient than electron writing ($-V_0$). This factor of four differences in hole and electron transport efficiency or μτ product has been noted by others [4.6-4.7]. Our results and these observations on this sensitivity difference in Se merit note, may be of concern in other SLMs, certainly effect SLM test procedures, and mean that dynamic sensitivity would be far better than static sensitometry data. In Figure 4.8, we repeat Figure 9 in Reference [4.6]. The curves in this Figure indicate that for certain μτ ranges ($3 \times 10^{-7} - 10^{-5}$), μτ variations by even a factor of 10 yield little difference in transmittance. However, in the larger absolute μτ ranges ($3 \times 10^{-7} - 10^{-8}$), small μτ differences yield large differences in transmittance.
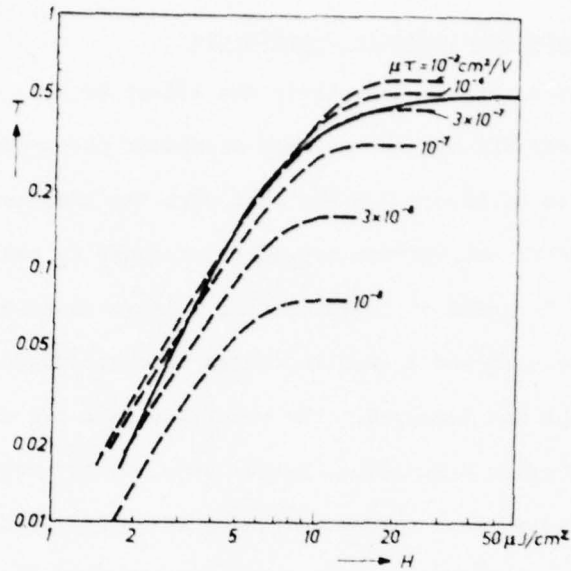
Figure 4.8 Transmittance vs. Exposure Characteristics of DKDP for
Various μτ Products [4.8]

It appears that the μτ products in our photo–DKDP SLM are in the 10^{-8} range
and that by increasing them to 10^{-7} - 10^{-6}, we can achieve comparable response for
hole and electron writing. Thus, it is possible to control the sensitivity of
positive and negative writing in this SLM. The lower $E_{\lambda WS}$ = 20μJ/cm^2 saturation
exposure given in Figure 4.8 compared to our Figure 4.7 data reflects the more
optimum λ_W = 401nm write light wavelength used in Reference [4.8] than the λ_W =
514nm write light intensity used in our experiments.

The low 18μW/cm^2 write light intensity available to us required long 10–100sec
exposures to achieve saturation. The voltage change across the Se during this long
exposure time made the voltage dependence of η quite important. Such effects may
well occur in other SLMs. In this particular device, better results are expected
at lower exposure times (dynamic).

Trapping of carriers within the bulk of the Se appears to be the origin of
the residual modulation and incomplete erasure noted by some researchers [4.9].

4.3.5 Long Exposure Sensitometry Experiments

To more fully determine and verify the effect of long exposure times and the sensitometry of this SLM and the voltage dependent photo-conductivity of the Se, the exposure system of Figure 4.9 was used with the components listed in Table 4.2. In these experiments, the voltage between electrodes E_1 and E_2 was fixed at ± 50, ± 100, and $\pm 150V$. For each of these initial voltage distributions, fixed $I_{\lambda W}$ levels $(0.167mW/cm^2)$ were used and T_W was increased to over 100sec. For each case, the reflected $I_{\lambda R}$ light was measured. The resultant data are shown in Figure 4.10. As expected from our prior discussion, better sensitometry results when positive rather than negative voltages were used (confirming the better sensitometry of hole than electron conduction) and when larger voltages were used (confirming the increased photo-carrier generation and transport efficiency at larger voltages).

The differences in the various exposure curves are due to: the long exposure times used, the change in voltage across Se with exposure time, the dependence of the photo-sensitivity of the Se on the voltage across the layer, and the variations in the time constant of the Se (photo-sensitivity increases with increased voltage, and the time constant decreases with increasing exposures). The dark time constant of Se ($\tau_{Se} = 50sec$) decreases to approximately 0.1-1sec or more with λ_W exposure (due to the decreased resistivity of the Se). At low exposure times (with respect to τ_{Se}), the resistance of the Se, M, and DKDP layers determines the voltage across the device. Since the resistivity of Se decreases with increasing write light exposure, so does τ_{Se}. At low exposure times ($T_W \ll T_{Se}$), we can consider T_W and voltage transfer across the DKDP to be linear. However, at large $T_W > T_{Se}$ (as in our experiments), the voltage division between layers of the device depends upon the resistance of the different layers. At sufficiently long exposure times, saturation is expected (and will be more pronounced at larger applied voltages). The saturation of the $\pm 150v$ sensitometry curve exhibits this effect, whereas saturation does not occur at lower initial applied voltages. From Figure 4.8, we see

that a lower exposure threshold $E_{\lambda WT}$ or exposure time T_W is required as V is increased ($T_W < 0.5$sec at V = +150v, $T_W = 0.5$-5sec at V = +100v, and $T_W + 5$-50sec at V = +50v). At the long 50sec exposures used, the dark current of the Se increases by itself simultaneous with the decrease in resistivity of the Se as light increases. Thus, at both low and high exposures, multiple effects enter to determine the shape of the resultant sensitometry curves. In general, at long exposures, the T_{Se} is more of a function of the voltage across the Se.

These observations of the dependence of the photo-sensitivity on the voltage across the photo-conductor and on the long exposure times comparable to the time constant of the Se, greatly effects sensitometry data that will result. In general with an SLM such as photo-DKDP, in which an integrating and storage mode SLM is used with a photo-conductor whose photo-sensitivity is voltage dependent, deserves special attention in obtaining sensitometry data. Care should be taken that the exposure times and write light intensity levels $I_{\lambda W}$ used in collecting sensitometry data, are compatible to what one would expect in actual real-time practice. As the data of Figure 4.10 shows, low $I_{\lambda W}$ levels and long T_W times (comparable to the time constant of the photo-conductor) cannot be used without an expected large difference in the resultant sensitometry data. This effect is considerably different from the reciprocity failure noted in other SLMs. Specifically, in the photo-DKDP, shorter exposure times improved the device's performance. Since all photo-generated carriers then see a large initial voltage that results in excellent photo-sensitivity and sensitometry. In future Sections, we consider other potential effects of this voltage dependent sensitivity and different sensitometry for holes and electrons. These applications include erasure (in which the voltage on the Se must be decreased to zero) and image addition and subtraction (in which second exposures are used to add or subtract a charge distribution from the latent charge distribution across the DKDP). The data of Figure 4.10c are included to show that the voltage transferred to the DKDP is approximately ½ of the initial voltage between the electrodes. For
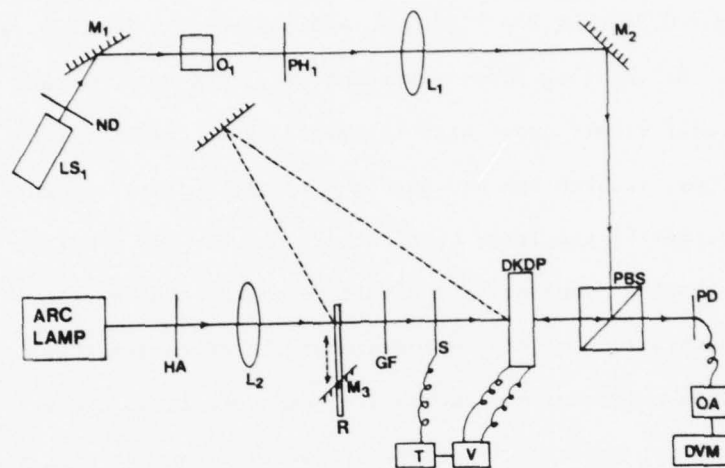
Figure 4.9   Modified Sensitometry Data Acquisition Test System

Table 4.2   Components used in the Sensitometry Data Acquisition Test
System of Figure 4.9

LS_1: 633nm laser

ND: ND filter

M_1M_2: Mirrors to fold the beam

O_1: 5x objective

PH_1: 10 μ pinhole

L_1 & L_2: 381mm collimating lens

HA: Heat absorbing glass

GF: Green filter (5105 ± 45Å)

S & T: Vincent Associates
shutter timer

V: Voltage controller

DKDP: P-DKDP assembly

PBS: NRC polarizing beam splitter
assembly

PD: United Technology wideband
photodiode

OA: Op. amp.

DVM: Digital voltmeter

R, M_3, M_4: Rail & mirrors for
erasure
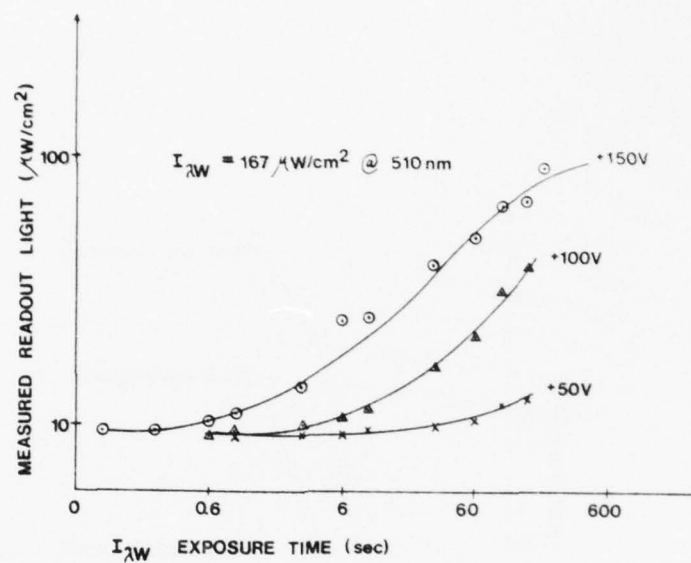
Figure 4.10a   Sensitometry for Photo-DKDP, Different Applied Positive Voltages
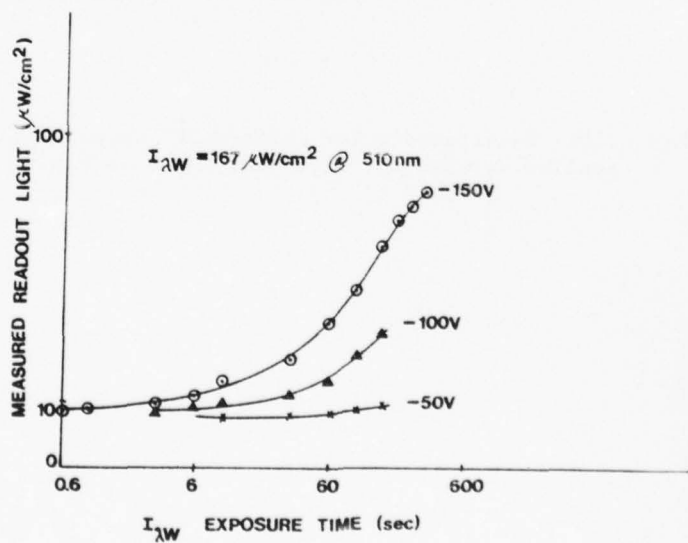
Figure 4.10b   Sensitometry for Photo-DKDP, Different Applied Negative Voltages
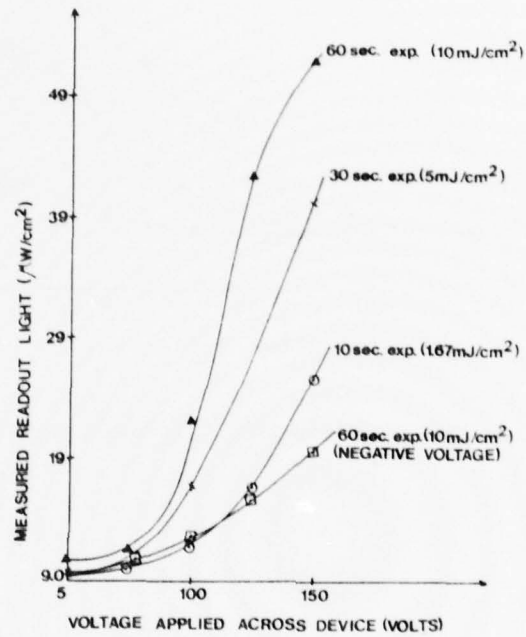
Figure 4.10c Sensitometry for Photo-DKDP, Output Light vs.
Applied Voltage for Different Exposure Times.

operation at -52°C, $V_{\frac{1}{2}} \simeq$ 300v. With 150v initially applied between electrodes, voltage transferred to the DKDP is $\frac{1}{2}$ of this or 75v. This is equivalent to $\pi/4$ retardation. The linearity of $I_{\lambda R}$ vs. $I_{\lambda W}$ or V is thus expected to be quite good over most of the input exposure range.

4.4 Erasure

In considering the erasure of a pattern stored on the DKDP, we isolate three cases: (a) dark storage (no λ_R light) in which the stored pattern simply decays with no external assistance, (b) destruction of a stored pattern under λ_R readout, and (c) erasure by illumination of the Se with λ_E (or broadband λ_W light) with the electrodes shorted.

4.4.1 Dark Storage

To analyze the state of the DKDP, we consider the RC equivalent circuit for the device shown in Figure 4.11. This approach is novel and unique. R_1C_1 is the time constant of the Se in the dark. Resistance R_p is the photo-controlled resistance which depends upon $I_{\lambda W}$ and λ_W used. The time constant R_2C_2 of the mirror is far less defined, but it appears that R_2 is small and C_2 is large. We represent the DKDP layer itself by an R_3C_3. From References [4.6-4.10], we find $R_1C_1 \simeq$ 50sec, whereas the time constant under illumination decreases to 0.1 to 1sec. Since the DKDP crystal is wedged (Section 4.2), we use average R and C values to model the DKDP crystal. The operating temperature T_C of this SLM greatly effects the resistivity ρ and dielectric constant ε of the DKDP as below [4.1,4.3],

$$\rho_{DKDP} = 10^{(-0.73 + \frac{2740}{T_K})} \, \Omega m \qquad (4.10a)$$

$$\varepsilon_{DKDP} = 650 \qquad (4.10b)$$

where the clamped case is considered. The thicknesses of the device's layers are [4.10]:

$$d_{DKDP} = 160\mu m$$

$$d_{Se} = 12\mu m .$$

For Se, we find [4.8,4.10]

$$\rho_{Se} = 10^{12}\Omega m \text{ (dark)} \tag{4.11a}$$

$$\varepsilon_{Se} = 6 . \tag{4.11b}$$

From this, the τ values for Se and DKDP are found to be

$$\tau_{Se} = 53.04 sec \tag{4.12a}$$

$$\tau_{DKDP} = 2671 sec . \tag{4.12b}$$

To obtain the R and C values for our DKDP model, we use $C = A\varepsilon\varepsilon_0/d$ and $R = \rho d/A$ where $A = 1cm^2$ is the area used.
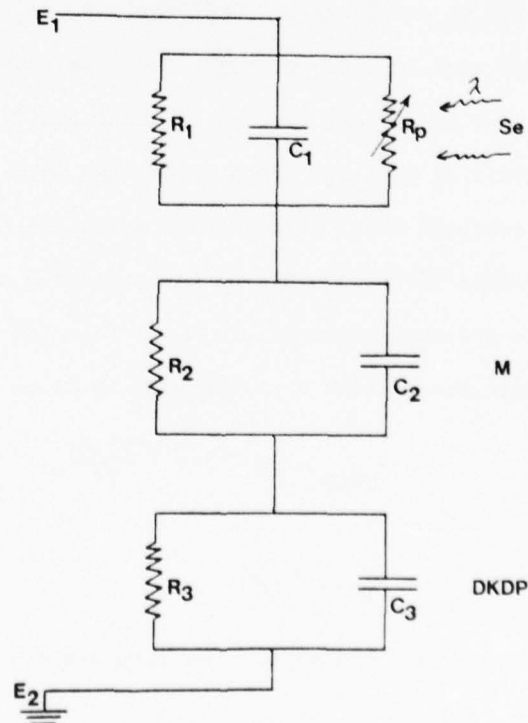
Figure 4.11 Equivalent RC Circuit Model for the Photo-DKDP SLM

At the output, we monitor the intensity I which is proportional to $\sin^2$ (kV). For low V, this is proportional to V^2 and since the dark decay time constant is τ_{DKDP} = 2671, the measured dark decay time constant for output intensity is $\tau/2$. From other data, we find the largest voltage across the DKDP to be approximately 75v, corresponding to a $\pi/4$ phase retardation. Thus, the above approximate results appear adequate. We thus expect a measured intensity decay time constant of 1340sec. The system of Figure 4.12 was used for dark decay measurements. The components used are listed in Table 4.3. To determine the exact effects of dark decay and its effects on contrast ratio, modulation, and resolution of a recorded image, a 5cy/mm squarewave pattern was recorded on the photo-DKDP (rather than a uniform pattern), and the intensity of the DC and first-order terms (I_0 and I_1) in the Fourier transform of this input were monitored vs. time, for all three erase mechanisms. For the dark storage measurements, a very low intensity readout light level ($I_{\lambda R}$ = 10µW/cm^2) was used. It was pulsed on for 5sec every 60sec for over one hour. For each readout light pulse, I_0 and I_1 were measured.

The resultant dark decay data for the DC or input bias level I_0 and the first-order modulation term I_1 are shown in Figure 4.13. From this Figure, we find that the DC and first-order modulation term decay at essentially the same rate. This implies that the dark storage decay of this SLM results in a loss of charge and thus output light without a loss of definition or modulation (measured as the I_1/I_0 ratio). From the data of Figure 4.13, we find a dark decay time constant, τ_I = 1680sec. This agrees well with the theoretical value calculated from (4.12) and from the equivalent circuit of Figure 4.11.

4.4.2 λ_R Readout Decay

The above experiment was repeated with a constant 50µW/cm^2 = $I_{\lambda R}$ light level. The data shown in Figure 4.14 indicates that λ_R readout light does degrade a stored pattern, since the τ_R time constants for the DC and first-order terms are τ_{RO} = 26min and τ_{R1} = 19min. From this, we see that the first-order intensity or

used in the LCLV and other SLMs. CdS photo-conductors cannot be deposited on photo-DKDP because of the high deposition or annealing temperature necessary in CdS to

66
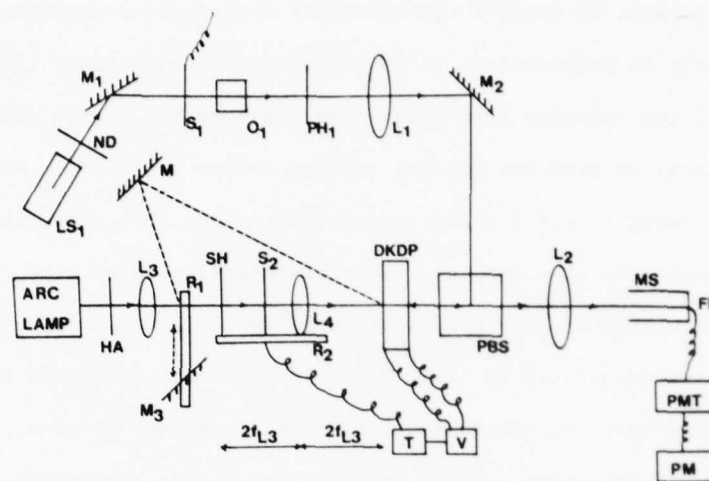
Figure 4.12 Experimental Test System Used for Dark, Readout, and Erase Decay Tests

Table 4.3 Components Used in the Test System of Figure 4.12

LS$_1$: 633nm laser

ND: ND filter

M$_1$,M$_2$: Mirrors to fold the beam

S$_1$,S$_2$: Vincent Associates shutters

0$_1$: 10x objective

PH$_1$: 5 μ pinhole

L$_1$: 762mm collimating lens

PBS: Polarizing beam splitter cube

L$_2$: 762mm FT lens

MS: Microscope with no objective

FP: 150μ fiber probe

PMT & PM: Scientific Photomulti-plier tube & photometer

HA: Heat absorbing glass

L$_3$: 831mm collimating lens

SH: Slide holder for the grating

S$_2$,T: Vincent Associates shutter & timer

V: Voltage control

R$_2$: Rail

R$_1$,M$_3$,M$_4$: Rail & mirrors for erasure

DKDP: P-DKDP assembly
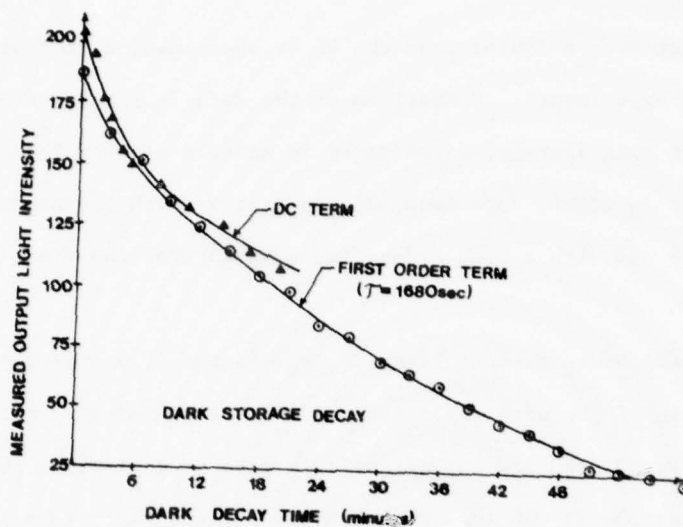
Figure 4.13 Measured Output Light Intensity vs. Time for Dark Storage Decay
of the DC and First-Order Terms in the FT of a 5cy/mm Squarewave
Grating Recorded on the Photo-DKDP SLM
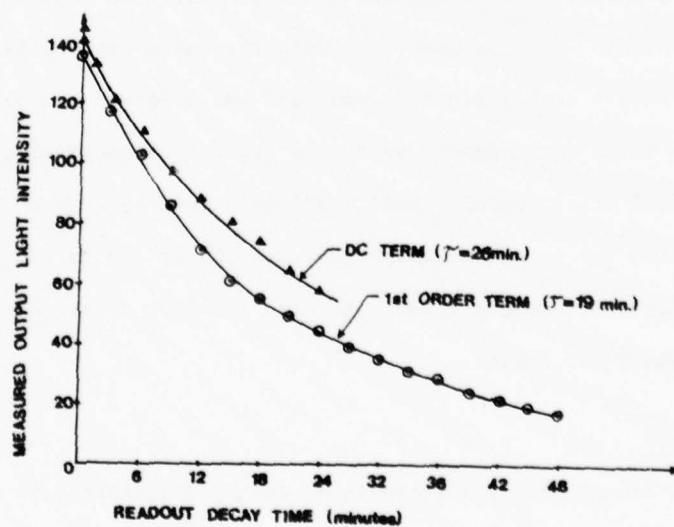
Figure 4.14 Measured Output Light Intensity vs. Time for Continuous Readout with
a 50μW/cm^2 λ_R Source for the DC and First-Order Terms in the FT of a
50cy/mm Squarewave Grating Recorded on the Photo-DKDP SLM

68

data modulation decays faster than the DC or bias level data (compared to the dark storage decay experiment). Comparison of the data in Figures 4.12 and 4.13 indicates that, in dark storage, image decay is uniform with no loss in definition; whereas, under λ_R light, data modulation decreases with readout (although only slightly, 11%) and with a long decay time constant for the first-order FT term of 19min.

Any effects of λ_R readout light on degradation of a stored image should be minimal because of the high reflectance (0.98) of the mirror at the λ_R = 633nm readout wavelength used and the essentially zero or negligible photo-sensitivity of the Se at this 633nm. The 1-2% of the readout light that leaks through M generates photo-carriers at the M interface which could degrade the latent pattern stored there. These carriers can destroy or degrade the stored charge pattern. However, the efficiency of these λ_R = 633nm photo-carriers is far less than for those produced at the λ_E or λ_W wavelength. It should be noted that the mirror in our photo-DKDP SLM has a transmittance of 50% at λ_R = 633nm and this could be the cause of the λ_R effects noted. Nonetheless, even with the large transmittance of the mirror in our device, a very long 19min time constant was observed and although modulation of the recorded image was degraded by the λ_R light, the decrease in modulation was quite minimal (11% after 30min). This modulation loss appears to be due to lateral carrier conduction due to increased photo-conductivity due to the readout light. The repeatability of these experiments is also somewhat questionable (due to the available equipment and funds).

4.4.3 λ_E Erasure

To erase a latent image, electrodes E_1 and E_2 are shorted to ground and the Se side of the device is flooded with λ_E light (broadband λ_W light from an arc lamp). The basic idea in this induced erasure is that a zero volt or uniform dark light pattern is written on the device. However, the mechanism of erasure is far different from writing of a uniform zero voltage pattern. Specifically, when illuminated with

λ_E light (with a stored latent charge pattern on the mirror), photo-induced electron and hole pairs are generated at the surface (near E_1) and in the depth of the Se (we believe). There are four mechanisms that enter into the active $_E$ erase process. The purpose of erasure is to remove the positive charge (for positive writing) or the negative (for negative voltage writing) charge trapped at the mirror and to reduce the voltage across the Se and the DKDP to zero volts. The mechanisms that occur during erasure include:

(a) Decrease in resistivity of the Se by charge carriers created at the interface.

(b) Recombination without charge migration.

(c) Migration of charge carriers (electrons) to the mirror to neutralize the positive charge there.

(d) Migration of electrons and holes and their recombination with other charge carriers within the volume of the DKDP.

Another factor that has a major effect on the erasure process is the voltage dependence of the photo-sensitivity of the Se. In erasure, the voltage across the Se (and likewise the DKDP) is initially large (75v from the data of Figure 4.10c) and in the final state V is zero. Because of the voltage dependence of the photo-sensitivity of Se, removal of residual charge on the mirror and the voltage across the device layers is difficult. The exponential decay curves of Figures 4.13 and 4.14 verify this. Application of a positive voltage (for the mirror negative) or a minus voltage (for the mirror positive) could improve the erase process in the bright regions. However, in the dark regions this would result in a charge build-up at the mirror (as occurs in writing). Application of a positive or negative voltage for a fraction of the erased time may be advantageous in the overall erasure process. This remains to be experimentally verified and quantified.

Erasure is clearly not the equivalent of writing, since the charge accumulated while writing must be transported back to E_1. This is not equivalent to creation of an equal number of charge particles of opposite charge. Rather, erasure is

achieved by modification of the transport properties of the Se (specifically an increase in its conductivity). An order of magnitude verification of the erase time (4-5sec, with 8mW/cm^2 of broadband arc lamp λ_E light) is possible. From [4.8] and [4.10] we find a 10^2 - 10^3 difference between the maximum photo-sensitivity and dark photo-sensitivity of the Se. The observed erase time constant τ_E = 4sec in Figure 4.15 is in this range of 10^2 - 10^3 less than the observed dark decay time constant.

The voltage dependence of the photo-sensitivity of Se and its wavelength dependence complicates analysis of the erase time data. In the experiments of Figure 4.10, 10mJ/cm^2 was required to saturate the SLM (at very long 60sec exposures). The faster 4sec erase time constant is due in part to more efficient broadband λ_E light used (the peak of the photo-sensitivity of the Se is 400nm) and the larger 8mW/cm^2 I_{λ_E} used. The larger initial voltage (150v) present across the Se at the start of writing vs. the lower (75v) present across the Se at the start of erasure makes writing more efficient than erasure (the initial write light energy is more efficient than the initial erase light energy). If the same λ_E and λ_W were used with comparable write and erase intensity and if the photo-sensitivity and voltage dependence of the Se were not factors, comparable write and erase times would result. In general, we find the write and erase speeds and hence the cycle time of the DKDP to be limited by the transit times of holes and electrons. With the efficiency and speed of writing or erasure with holes superior to that of electrons, only one process (writing or erasure) can be optimized. With equal $\mu\tau$ products and further device work, erasure can be optimized also. However, as in writing, large erase intensities and short erase times yield far better results than lower intensities and longer erase (or write) times. As in writing, we have found erasure by holes (corresponding to $-V_0$ writing) to be superior to erasure by electrons (corresponding to $+V_0$ writing).

In all of the data in Figures 4.11 - 4.14, the Fourier transform spot size $\lambda f_L/d$ was 138μm and the measuring fiber optic probe used was of diameter 150μm.

71
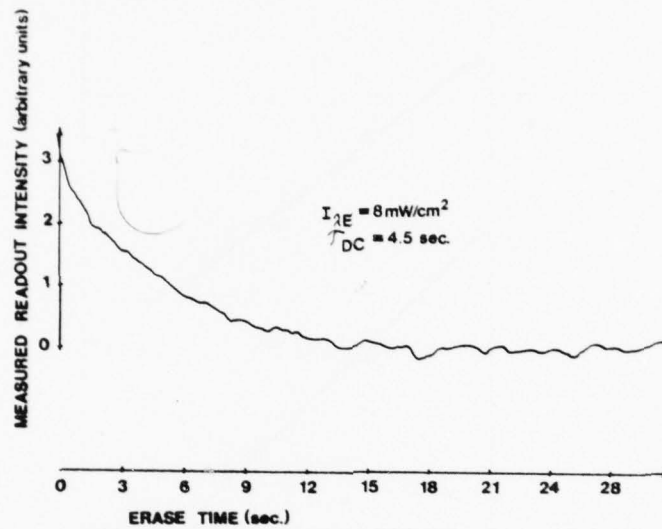
(a) DC Term
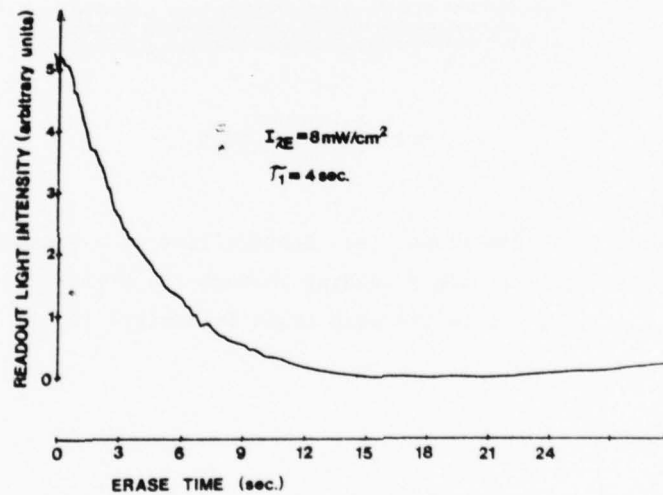
(b) First-Order Term

Figure 4.15 Measured Output Light vs. Time (for Continuous Erasure with a Broadband $8mW/cm^2$ Erase Source) for the (a) DC and (b) First-Order Term in the FT of a 5cy/mm Squarewave Input Recorded on the Photo-DKDP

72
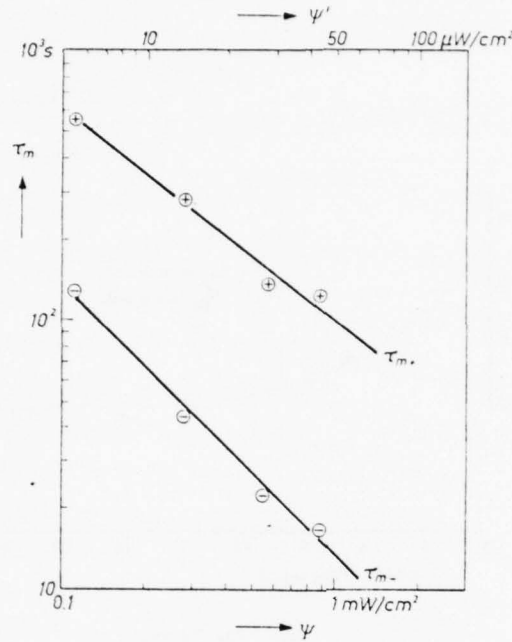
Storage time τ_m as a function of the intensity ψ of the read-out light. The upper curve (τ_m+) is for a positive latent image, the lower curve (τ_m-) for the negative one. ψ' is the residual intensity of the light that has passed through the dielectric mirror and is absorbed by the selenium. Wavelength of the read-out light 579 nm.

(c) Leakage Light

Figure 4.15 Continued (c) Storage Time as a Function of
$I'_{\lambda R} = \psi'$ Light Leaking Through the Mirror M
($I_{\lambda R} = \psi$ is the Read Light Intensity) [4.8].

DKDP). The data of Figure 4.10c are included to show that the voltage transferred to the DKDP is approximately ½ of the initial voltage between the electrodes. For

This large probe size equal to the diffraction limited Fourier transform plane spot size allows measurement of the total energy in the DC and first-order spots and their change with time (compared to the time decay of only the peak of the DC and first-order components of the input pattern). Attention to such measuring and data acquisition techniques are necessary. The degradation of the charge pattern at the mirror interface is limited by two processes: (a) thermal activation of charges from surface traps and (b) annihilation of trapped charges by capture and recombination of free charges of opposite sign. In the first process, the charges diffuse laterally resulting in progressive erasure and loss of definition. In the second process, the bias of the images decreased without any degradation in its definition (sharpness of edges). As our data in Figures 4.12 - 4.14 show, the second process is dominant in practice.

Under λ_R readout, the efficiency with which the λ_R light ψ' leaking through the mirror M generates free carriers (some of which recombine with charges of the latent image at M, thereby erasing the latent charge pattern at M) is low. In Figure 4.15c, we show data on the storage time T_s as a function of the incident $I_{\lambda R} = \psi$ and the λ_R light ψ' leaking through M (a 5% mirror transmittance is assumed). From these data and a given application scenario, the $I_{\lambda R}$ light level that can be used for a given desired T_s can be determined. These data were obtained from [4.8] and it is not known if they are theoretical or experimental. But at the λ_R = 579nm used in these data, the Se is far more photo-sensitive than at the 633nm wavelength we used. In addition, as we noted earlier, the mirror in our DKDP was found to have a 50% transmittance at 633nm. Thus, direct quantitative data comparisons are not possible. From Figure 4.15, we see that λ_R destructive readout of a positive image is less than for a negative image. This is explainable by assuming that some of the holes generated by the λ_R light leaking through M disappear by bimolecular recombination. This is clearly not the only process, since if it were the carrier density would be proportional to the square
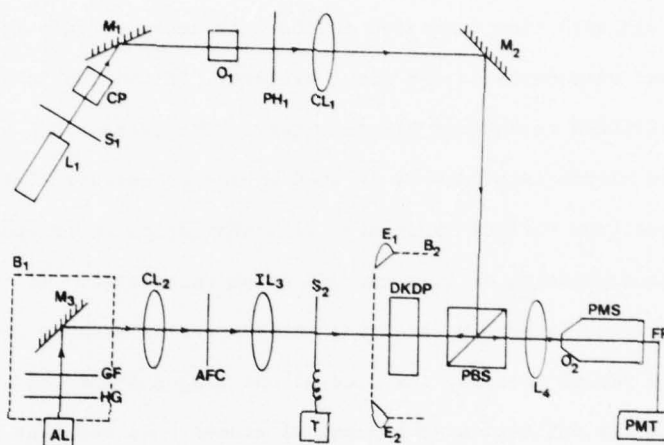
Figure 4.16 Photo-DKDP Imaging MTF Data Acquisition System

Table 4.4 Components Used in the Imaging MTF System of Figure 4.16

L_1: Read laser (633nm) by Spectra Physics

CP: Calcite polarizer

S_1: Shutter for read light

M_1, M_2, M_3, M_4: mirrors

O_1: 20x objective

CL_1: 762mm collimating lens

PBS: Polarizing beam splitter cube

L_4: 105mm relay lens

O_2: 10x objective

FP: 50 μ Fibre optic probe

B_1 & B_2: Black enclosures

AL: Arc lamp

HG: Heat absorbing glass

GF: Green filter (5105Å with $\Delta\lambda = 90$Å)

CL_2: 381mm lens

IL_3: Imaging lens (8¼", F/4.5)

S_2 & T: Shutter with electronic timer

AFC: Air Force 3 bar resolution chart

PMS: Photometric microscope

PMT: Photo-multiplier tube

E_1 & E_2: Erasing flashes

Figure 4.10b Sensitometry for Photo-DKDP, Different Applied Negative Voltages

75

root of the luminious intensity and the slope of the T_s vs. time curve in Figure
4.15 would be ½. The faster decrease in T_s for a negative image seems to indicate
an additional recombination process due to holes injected into the Se from the
front electrode E_1. These photo-injected holes are attracted to the minus charge
latent image with a density proportional to $I_{\lambda R}$ resulting in a T_s inversely pro-
portional to $I_{\lambda R}$.

4.5 Resolution, Contrast, Modulation, and MTF

The resolution of an SLM is one of the most elusive parameters to measure and
quantify. The resolution test system and measurement test procedure used must be
well documented, as well as the equations used to reduce the data obtained to
resolution, contrast, modulation or MTF graphs. Particular attention must be
given to: the definitions of the terms used, distinguishing between amplitude and
intensity modulation, properly documenting test conditions, such as input modula-
tion levels used, and avoidance of normalized modulation and MTF data. In Chapter
2, these items were adequately addressed. Thus, in this Section we present the
results of only five MTF tests performed on the photo-DKDP: (a) imaging MTF
(Section 4.5.1), (b) interferometric MTF (Section 4.5.2), and two new methods
(c) reflectance imaging MTF (Section 4.5.3) and (d) edge MTF (Section 4.5.4). In
Section 4.5.5, we quantify our resultant MTF data and compare it to the theoreti-
cally expected results. We conclude in Sections 4.5.6 and 4.5.7 with a discussion
of the appropriateness of the various MTF tests to diverse real-time optical data
processing applications and with several general remarks on the equipment, parti-
cularly the polarizers, beam splitters, and polarizing beam splitters to be used.

4.5.1. Imaging MTF

The imaging MTF test system used with the photo-DKDP is shown in Figure 4.16.
The components used are listed in Table 4.4. To obtain a better extinciton ratio,
a calcite polarizer (CP) was included. Enclosures B_1 and B_2 were used to shield

the DKDP from the stray arc lamp light. To reduce the degrading effects of read
light, continuous readout was not used. Rather, the fiber optic readout probe w
focused on a single bar on the output image (using several repeated exposure and
erase cycles to obtain best focus). The shutter S_1 was then opened and the reco
structed image of one three-bar pattern was quickly scanned and the minimum or
maximum intensities were recorded. A low $I_{\lambda R} = 3\mu W/cm^2$ light level was used. T
test was then repeated to ensure that no degradation in the recorded pattern had
occured.

A write intensity $I_{\lambda W} = 150\mu W/cm^2$ was used to illuminate a $2cm^2$ region of t
crystal. Two exposures of 2.1 and 4.1 second duration were made of the various
bar element patterns in the test chart. Both of these exposures ($315\mu J/cm^2$ and
$615\mu J/cm^2$) were repeated twice and were repeated again for both $\pm150v$ across the
DKDP assembly. From the sensitometry data of Figures 4.7, we see that these ex-
posures lie near the saturation end of the sensitometry curve for $\pm150v$ writing
and in a more linear region further from saturation for the $-150v$ writing.

In Figures 4.17 and 4.18, we show the resultant MTF data (unnormalized) ob-
tained as described in Chapter 2 for $V_0 = \pm150v$ and using 2.1 and 4.1 second
exposures. Comparing these data, we note lower modulation for $\pm150v$ writing tha
for $-150v$ writing. This may be due to the sensitometry issues noted in Section
4.3. A superior cooling system and better mounting of the crystal holder may be
sources of experimental error. However, as noted in Chapter 2, the repeatabilit
of imaging MTF data and its susceptibility to operator attitude, etc., are our
primary objections to such MTF data acquisition methods.

The 10 - 12cy/mm resolution obtained at 50% of the peak modulation for this
SLM can be improved. This was done later by use of a better alignment technique
for the imaging system and the SLM in Figure 4.16. The readout system and DKDP
were aligned using a point beam in these advanced tests. Initially, the light
transmittance through the mirror was used to align the imaging system. However,
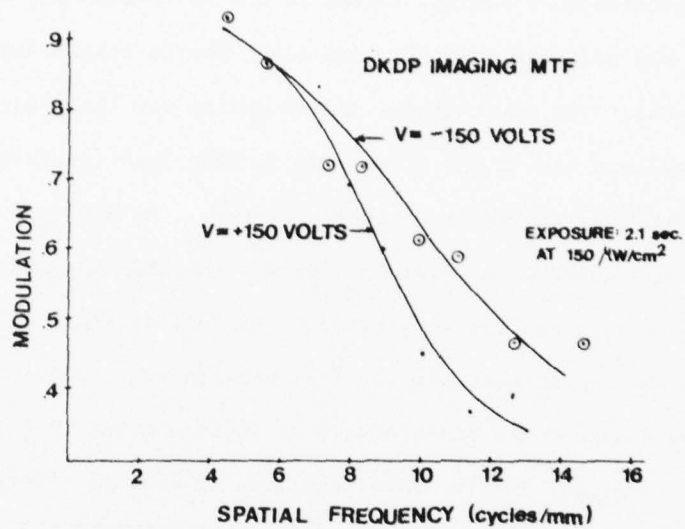
Figure 4.17   Imaging MTF for ±150V for Photo-DKDP (2.1sec Exposure)
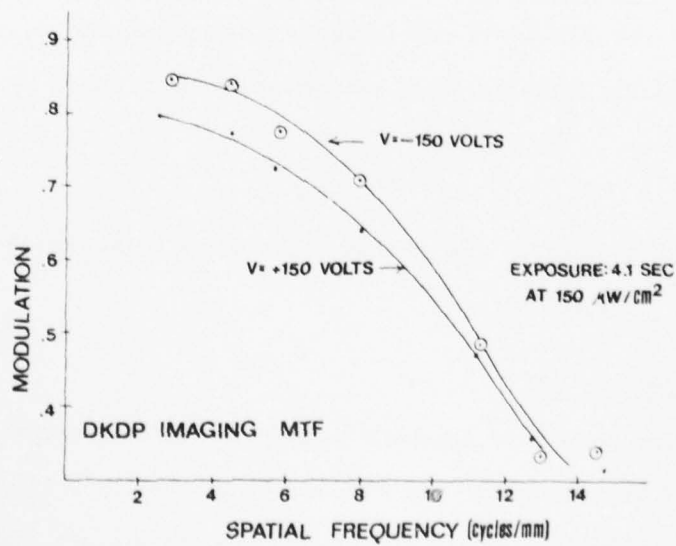
Figure 4.18   Imaging MTF for ±150V for Photo-DKDP (4.1sec Exposure)

when it was determined that several layers in the photo–DKDP SLM were wedged, the above technique was modified (the arc lamp light source itself was useless for alignment purposes). The first change in the system was the change from 1:1 imaging. This allowed use of the Nikkor F/3.5, 55mm lens (depth-of-field above 1000μm). This lens and the entire system except for the DKDP was aligned using a point beam from the 633nm laser readout source. The DKDP unit was then inserted and aligned. The resultant system yielded observable resolutions beyond 20cy/mm.

We note at this point that the IL_3 lens used in acquiring the test data of Figures 4.17 and 4.18 had a depth-of-focus of 200μm or over 20 times the thickness of the Se photo-conductor layer. Thus, any lens or imaging effects and differences in imaging interferometric MTF data will not occur. The 2.1 and 4.1 second exposures at 150μW/cm^2 correspond to exposure energies of 300 and 600μJ/cm^2. From the sensitometry data of Section 4.3, we see that these exposures correspond to the saturation region of the device. Thus (as noted in Chapter 2), only binary MTF data results from such an imaging MTF test. This is another objection we have to such an experiment. The write light intensity is measured in a 1cm^2 all bright area in front of the DKDP. For the longer 4.1 second exposures, the dark of I_{min} output levels clearly increase, thus making measurements of

$$M_{out} = \frac{\overline{I} - \underline{I}}{\overline{I} + \underline{I}} \tag{4.13}$$

difficult. Input modulation was assumed to be unity in all tests (since a chromium plated AF chart was used).

4.5.2 Interferometric MTF

Were sinewave pattern of adequate quality in various spatial frequencies available, they could be imaged onto the SLM, and hence the SLM's linear recording tested. However, sinewave inputs of adequate quality are not easily obtainable, especially at high spatial frequencies. These problems and the other disadvantages present in an imaging MTF test can be avoided if the input data is interferometri-

cally recorded as discussed in Chapter 2. The experimental system used to achieve this is shown in Figure 4.19 and the components used for it are listed in Table 4.5. The recording system's operation is basically to interfere two plane waves on the SLM. These beams are combined at the BS and the angle θ between them (and hence the spatial frequency of the recorded sinewave) is adjusted by tilting mirror M_6. The intensity ratio of the two beams, and hence the modulation of the recorded sinewave pattern is varied by the VBS. The average exposure for the SLM is adjusted by controlling the intensity of the laser using a timer and shutter in the output laser beam. The sinewave pattern incident on the SLM is in focus over the entire thickness of the device, thus reducing input focusing errors. Since the Fourier transform plane pattern is examined and since it contains only three spots of light, output plane focusing problems are likewise greatly reduced.

The read system is similar to those described before. The Fourier transform of the sinewave pattern recorded on the SLM is formed by the Fourier transform lens of the Fourier transform plane (FP) where it is scanned with a photometric microscope. For a pure recorded sinewave only a DC and ±first-order FT plane spots should appear. The presence of second-order spots indicates a non-linear input recording, the amplitude of the second-order spots indicates the amount of the non-linearity.

To measure the MTF from this test system, we simply measure I_0 and I_1 (the intensity in the DC and one first-order spot in the FT plane) to obtain M (out). The process is repeated for different tilts of the mirror M_6 in Figure 4.19. This results in different interference angles θ and sinewave spatial frequencies α in the recorded pattern. We distinguish two types of MTF data (linear and non-linear). In the linear MTF test, we select the average input intensity to lie in the center of the linear region of the device's sensitometry curve. We increase the input modulation while monitoring I_2 (the intensity in the second-order spot in the FT plane pattern). We maintain I_2 at 20dB below the level of I_1. This setting ensures
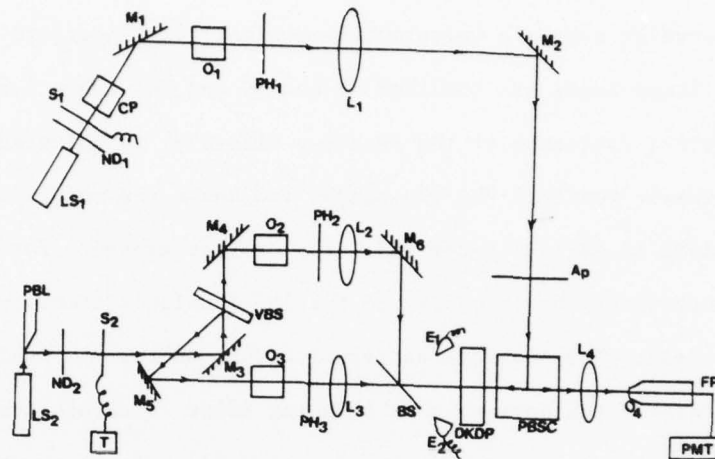
Figure 4.19 Photo-DKDP Interferometric MTF Data Acquisition System

Table 4.5 Components used in the MTF System of Figure 4.19

LS_1: 633nm laser

LS_2: 514nm laser

S_1: Shutter for read light

CP: Calcite polarizer

M_1,M_2,M_3,M_4,M_5,M_6: Mirrors

O_1 & O_4: 20x objectives

O_2 & O_3: 5x objectives

PH_1: 10 μ pinhole

PH_2 & PH_3: 5 μ pinholes

L_1: 762mm collimating lens

L_4: 762mm FT lens

L_2 & L_3: 381mm collimating lenses

PBSC: Polarizing beam splitter cube

FP: 50 μ Fibre optic probe

PMT: Photomultiplier tube

PBL: Periscopic beam filter

ND_1: Neutral density filter for read light

ND_2: 10% ND filter

VBS: Variable beam splitter

BS: NRC beam splitter

DKDP: The crystal; E_1 & E_2: Erasing flashes

that the output sinewave is linear within 1%. Alternate ratios between I_1 and I_2 can be used and will result in even more linear interferometric sensitometry data. We then recorded I_1/I_0 and from it calculated M_{out}. We plot unnormalized M_{out} vs. α and note the average exposure and input modulation on the corresponding Figure.

In our experiments, the average exposure $I_A + I_B$ was measured to be $80.37\mu W/cm^2$ and the input modulation to be 98.6% for these tests. With the 762mm focal length transform lens used, each 1mm displacement of an FT plane spot from DC was calculated to correspond to 2.074cy/mm of input spatial frequency. Locations of these first-order FT plane spots were used to determine the input spatial frequency recorded. This technique was found to be far superior and more accurate than attempting to measure the small angle between the two interfering input beams.

With an $80\mu W/cm^2$ write average input light intensity and an 80msec exposure time, the average write light intensity was calculated to be $6.50\mu J/cm^2$. This exposure level lies in the linear region of the t-E exposure curve for this SLM as shown in the sensitometry data in Chapter 2. Thus, this MTF test is referred to as a linear MTF test. For a non-linear interferometric MTF test, the exposure time was increased to 750msec; the corresponding average exposure is now $60.3\mu J/cm^2$. This value is seen to lie toward the saturation region of the sensitometry curve in a far more non-linear region of the t-E curve for the SLM. We thus refer to the MTF test conducted with this bias exposure as a non-linear interferometric MTF test.

As described in Chapter 2, the sinewaves were interferometrically recorded on the DKDP SLM and the resultant FT plane pattern was scanned. In all linear MTF tests, no measurable second-order FT plane spot was visible. This implies a very linear input recording exists. In addition, the dark field in the FT plane was found to be unmeasurable, even using the scanning photometric detector. For the non-linear interferometric tests, the exposure times used were varied until a second-order FT plane spot was at least visible (it was still more than 20dB below the intensity of the first-order FT plane spot). The modulation obtainable was

calculated from the ratio I_1/I_0 of the intensities of the first-order and DC order terms in the FT plane pattern. The resultant MTF curves for both linear and non-linear bias exposure cases are shown in Figures 4.20 and 4.21.

From these data, we see that the resolution of the DKDP light valve at 50% of the peak modulation was larger for the interferometric MTF tests (14-15cy/mm) than for the imaging MTF tests (10-12cy/mm). We attribute this to the focusing and measurement ease present in the interferometric MTF tests compared to the imaging MTF test.

The input modulation for all experiments was maintained at 98.6%. The output modulation m_{out} is defined as in Chapter 2 as

$$M_{out} = \frac{4\sqrt{I_1/I_0}}{1 + 4I_1/I_0} \quad . \tag{4.14}$$

Equation (4.14) was used in assembling the data of Figures 4.20 and 4.21. We now consider several other aspects of this interferometric MTF data. First, exposure times in these MTF tests were only 0.75sec. The corresponding 60 J/cm^2 point on sensitometry data in Section 4.3 for this SLM required exposures in excess of 5sec. These observations and our sensitometry remarks are advanced in Sections 4.3 and 4.4. They can be used to explain the larger modulation (0.9) observed for the linear MTF case than for the modulation (0.5) observed for the non-linear MTF case. In practice, the actual sensitometry curve for the DKDP SLM is higher in transmittance than is indicated and is shifted to the left more than is indicated in the data of Sections 4.3 and 4.4. These phenomenon we refer to as long exposure saturation. This effect occurs because of the long write times (long with respect to the RC time constant of the SLM). Thus, the "non-linear" bias point used is actually a linear bias point at the actual experimental conditions used. The longer exposure necessary in the non-linear bias MTF experiment also increases the dark light level. These effects combine to produce larger modulation for the linear input data case. The low (75v) voltage present across the DKDP SLM and the
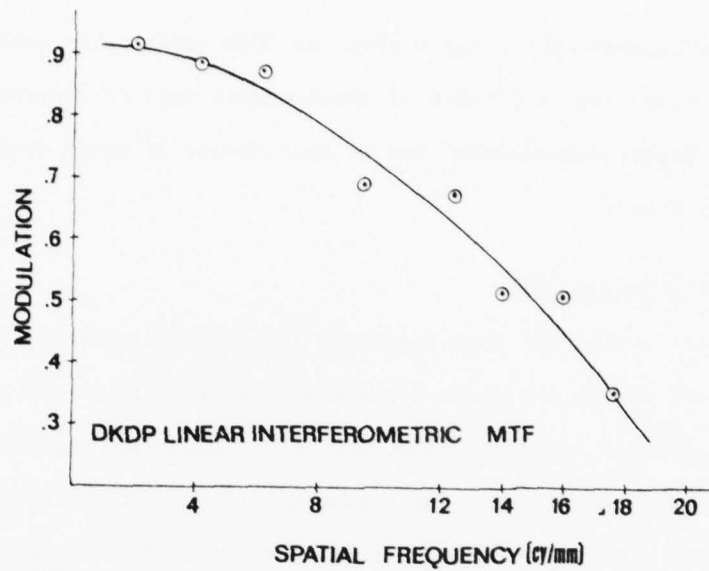
Figure 4.20   Interferometric MTF (Linear) for the Photo-DKDP
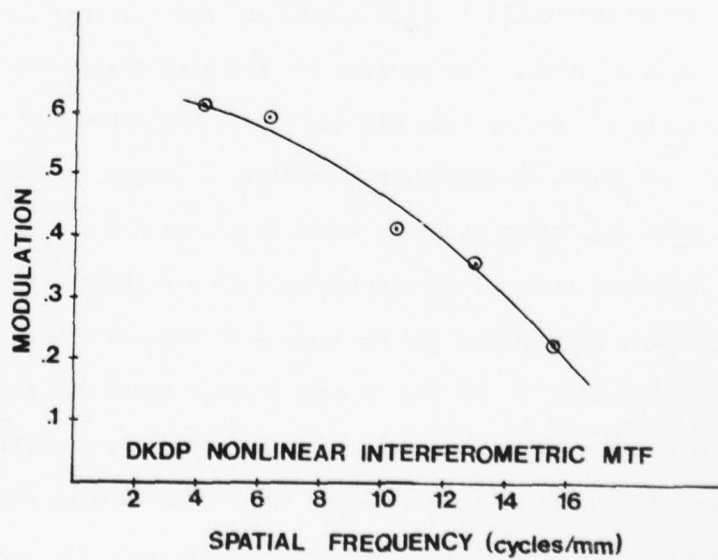
Figure 4.21   Interferometric MTF ("Non-Linear") for the Photo-DKDP

lack of observed second-order terms within the 20dB level of I_1 tend to verify the above remarks. Thus, the importance of sensitometry data of accuracy and compatibility with the actual experimental use of this device is again demonstrated to be of paramount importance.

4.5.3 Reflectance Imaging MTF

An alternate imaging MTF test conducted involved illuminating a reflectance (chromium) version of the Air Force 3-bar chart in reflectance and subsequently focusing this reflected image onto the DKDP SLM. The reconstruction of this image was then scanned and the MTF data was produced as before. This test system used is shown in Figure 4.22. The components used in it are listed in Table 4.6. Since this system differs only slightly from the prior MTF ones, we do not repeat our prior system description of it. Only the ±150v positive writing case was considered in these experiments. The write light intensity was set at $26.1\mu W/cm^2$ and a 2.5sec exposure was used. This resulted in a $65.25\mu J/cm^2$ bias exposure level.

The resultant reflective MTF data is shown in Figure 4.23. Comparing it to the other MTF data in Sections 4.5.1 and 4.5.2, we find a lower 7cy/mm resolution at 50% of the peak modulation. Our purpose in this test system was primarily to experimentally assess the use of this MTF technique. An extensive laboratory session in which the system alignment, collimation, focusing, and the output detector system used were completely revised, would have resulted in improved MTF data for this test. However, rather than attempting such a quantitative experimental program on an MTF data acquisition system plagued by various other disadvantages, we choose to merely comment on the use of such a reflectance MTF test system.

In such a reflective MTF experiment, there is significant scatter which greatly increases the background noise level, thereby decreasing the output modulation. In a transmission imaging MTF test, one can increase the light as much as possible and easily place it well into saturation. In this present test, the background noise rises as the input write light exposure is increased. One can

DKDP MTF USING REFLECTED AF CHART
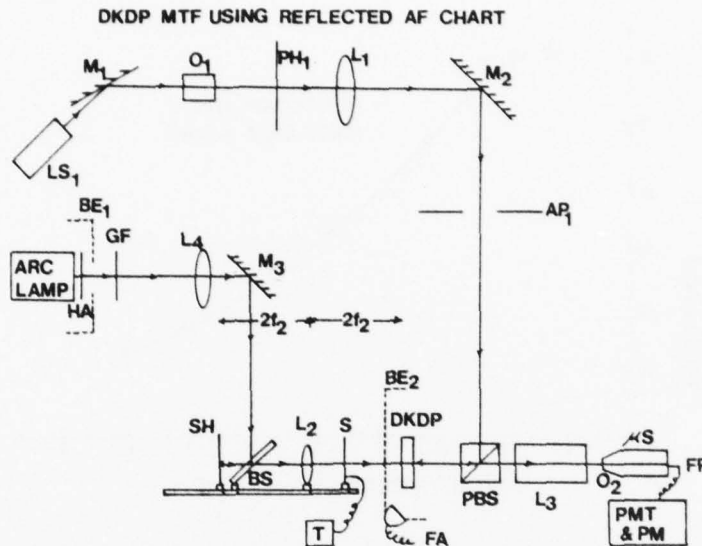
Figure 4.22   Photo-DKDP Reflective Imaging MTF Data Acquisition System

Table 4.6   Components used in the Reflective Imaging MTF System of Figure 4.22

LS_1:   633nm laser

0_1:   10x objective

PH_1:   10 μ pinhole

L_1:   381mm collimating lens

M_2 & M_3:   Mirrors

AP_1:   Aperture to cut extraneous light

PBS: Polarizing beam splitter cube

L_3:   Nikon 105mm imaging lens

0_2:   5x objective

μS: Microscope

FP: 50 μ Fibre probe

PMT & PM: γ scientific photomultiplier tube & photometer at 500V

HA: Heat absorbing glass

GF: Green filter (5105 Å with $\Delta\lambda$ = 90Å)

L_4:   381mm collimating lens

BS: 2" dielectric beam splitter

L_2:   8¼" f/4.5 imaging lens

S & T: Shutter & timer

FA: Flash assembly

DKDP: DKDP assembly

SH: Slide holder w chrome AF chart (negative)

f_2:   Focal length of L_2

Note: SH, L_2 & DKDP form 1:1 imaging system
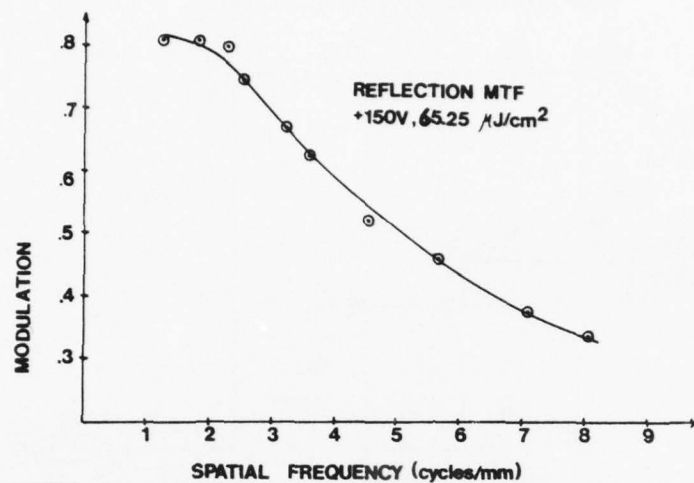
Figure 4.23 Reflective MTF for the Photo-DKDP
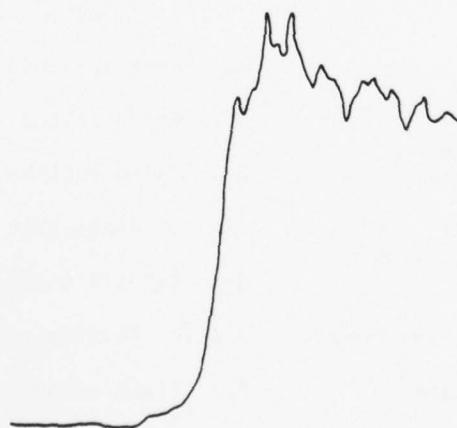
SCAN OF AN EDGE IMAGED ON DKDP

$I_{max} = 145$ (RELATIVE UNITS)
$I_{min} = 4.5$

Figure 4.24 Edge MTF Output Data for the Photo-DKDP

increase modulation at lower spatial frequencies by increasing the light level, but the increased background noise level then greatly decreases the modulation at higher spatial frequencies. This issue is closely connected to the procedure we use to obtain the best MTF from such an imaging experiment. To obtain the best resultant modulation, the input write light level and the readout light intensity are increased until the minimum output light level is as low as possible. However, this minimum output light level must be measurable and it must be above the system and detector noise levels. In this reflective MTF experiment, the larger minimum output reconstructed intensity (due to increased scatter) makes adjustment of the system difficult. In conclusion, reflective imaging MTF should yield results comparable to those of a transmission imaging MTF experiment. However, far greater care and operator technique is necessary. This measure of MTF is useful when the actual input data in the real system application is of low contrast and has a large bias level (e.g., aerial imagery, imaging from a T.V. monitor or an ambient scene). However, since the interferometric MTF system can achieve similar control and is far easier to use and results in a far more reproducible output data, it is again preferable.

4.5.4 Edge MTF

An alternate technique for obtaining the MTF of an SLM involves imaging an edge onto the output detector using the SLM as a relay. A cross-sectional scan of the reconstructed edge will not be a step function, but will have a finite slope together with overshoot and ringing. The post-processing required to extract MTF information from such an output edge image is described in [4.11-4.13].

Theoretically a step response of a system should give the exact system transfer function. [4.11-4.13 and 4.22] discuss how to obtain the MTF of a lens or a photographic system from reconstructed images of an edge (or a step) through the system. After considerable experimentation, we found out that it was very

difficult to perform this test on SLMs. We outline a general approach to this MTF acquisition method, and discuss the implementation and other problems we have found.

The five steps involved in this MTF data acquisition method follow:

(a) An edge scan is obtained by sampling the reconstructed image of an edge image recorded on the SLM. The sampling interval necessary in the output detector is determined by the Nyquist criterion. The actual edge spread function is related to these sampled values by the sampling theorem

$$E(x) = \sum_{n=-\infty}^{\infty} E(n\epsilon) \ sinc(\pi(\frac{x}{\epsilon} - n))$$

where ϵ is the sampling interval.

(b) Small errors in recording or measuring (due to the grain of film) should be removed by smoothing. In case the scan or samples are obtained using a non-linear recording or measuring instrument, one must correct the edge spread function obtained above using the sensitometry of the recording medium.

(c) MTF is defined as the modulus of the optical transfer function, which in turn is the Fourier transform of the line spread function. The edge spread function is related to the line spread function by

$$E(x) = \int \ell(x)dx$$

The edge spread function is used because it is easily obtained by imaging.

(d) As derived in [4.11], the OTF is given for $f < f_c$ by

$$OTF(f) = \sum_{n=-\infty}^{\infty} j2\pi f \ \epsilon E(n\epsilon) \ e^{-j2\pi f(n\epsilon)}$$

where ϵ is sampling interval and $f_c = \frac{1}{2}\epsilon$.

The problems associated with using this test on SLMs were many. We used a 25μm fiber probe with a 5x objective. This should theoretically give a sampling interval of 5μm. However, due to statistical errors associated with the scanning

eyepiece and the chart recorder maximum achievable sampling interval was much larger. Even when a good lens (which is highly spatially uniform) is tested, the data analysis required to extract MTF information from an edge image, requires the use of very complex computations [4.13]. In comparison to a good lens, the SLM was found to be highly non-uniform in its response. Thus, the test has to be repeated for a large number of points and one would have to literally obtain a point-by-point MTF.

The scan we obtained is reproduced in Figure 4.24. As one can visually see, it does not conform to what one would expect. We thus considered that pursuing this test was unwarranted in our present effort.

4.5.5 Quantitative MTF Theoretical Comparison

In this Section, we consider a resolution model for the DKDP SLM and the agreement between our experimental MTF data and the theoretically predicted results. Roach [4.14] and other [4.15-4.16] have adequately considered the resolution of such SLMs. Assuming a DKDP thickness "a" and a dielectric mirror of thickness "b", charge accumulation at the interface is considered and the ε_z and ε_x dielectric constants for the DKDP and ε_D for the mirror are assumed. Laplace's equations are then solved in the two media for the potentials at the various interfaces using Maxwell's equations.

$$D_{1z} - D_{2z} = \sigma , \qquad (4.15a)$$

for the mirror,

$$\nabla^2 V_1 = 0 . \qquad (4.15b)$$

Similarly for DKDP,

$$\frac{\partial^2 V_2}{\partial_x{}^2} + \frac{\partial^2 V_2}{\partial_y{}^2} + \frac{\varepsilon_z}{\varepsilon_x} \frac{\partial^2 V_2}{\partial_z{}^2} = 0 . \qquad (4.16)$$
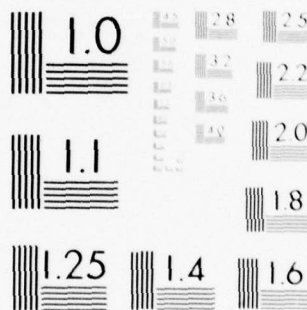
MICROCOPY RESOLUTION TEST CHART
NATIONAL BUREAU OF STANDARDS 1963 A

These Equations are then solved with the boundary conditions of matching the voltages between the two regions and assuming a surface charge density

$$\sigma = \sigma_0 \cos 2\pi\nu x \qquad (4.17)$$

to be of a single frequency ν. The resultant voltage V across the DKDP is then found to be

$$V = V_2(\nu)\cos 2\pi\nu x + \text{Bias} \qquad (4.18)$$

where

$$V_2(\nu) = \frac{\sigma_0/2\pi\nu\epsilon_0}{(\epsilon_z\epsilon_x) \ \text{Coth}[(\epsilon_x/\epsilon_z) \ 2\pi\nu a] + \epsilon_D \ \text{Coth}(2\pi\nu b)} \ . \qquad (4.19)$$

From (4.19), we see that as the spatial frequency ν increases, $V_2(\nu)/V_2(0)$ decreases. This V_2/V_0 vs. ν Equation is the amplitude modulation m_A or yields the amplitude MTF. The resultant output MTF is then

$$m = \frac{2m'}{1 + m'^2} \ . \qquad (4.20)$$

Substituting values for our photo-DKDP SLM and the physical constants of the various layers, we obtain the theoretical MTF plot shown in Figure 4.25. Comparing it to the interferometric MTF data, we find excellent agreement between theory and experiment. This agreement between theory and experiment, together with the close agreement between the different MTF data (differences are due mainly to the ease with which the various MTF tests can be performed and the precision required to obtain the various MTF data) implies that our experimental procedure was most accurate.

4.5.6 Application Relevance of MTF and Other Tests

In Chapter 2, we considered various noise tests that we feel should be performed on SLMs. The FT of a square input aperture is of use in determining the

Figure 4.25   Theoretical MTF for the Photo-DKDP

system's scatter level and the interharmonic distortion present in an input signal due to the system's linear MTF. The detector noise level can also be isolated from these experimental investigations by such a test. Use of a small input aperture can alleviate many of these problems at the test and experimental level. The importance of accurate SLM sensitometry data has been clearly demonstrated in our prior tests. The need for spatial data of this type was also p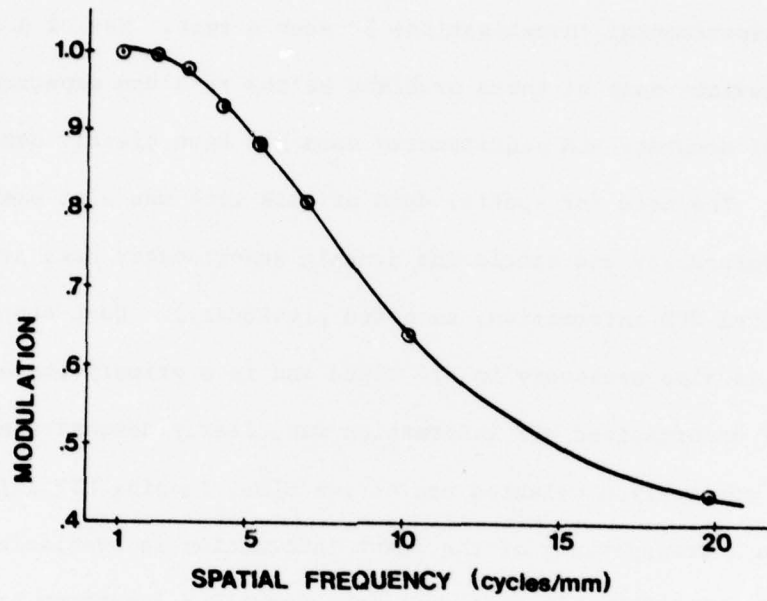reviously demonstrated. Reciprocity and static and dynamic sensitometry data are necessary (as well as spatial OPD information, as noted previously). Dark state minimum data information is also necessary in MTF tests and is a primary issue of concern. The need for unnormalized MTF information was clearly demonstrated in Chapter 2.

In the application oriented use of the SLMs, imaging MTF information is of concern when a transparency of the input information is available and is imaged onto the real-time SLM. In this case, the input SLM functions primarily as a non-coherent to coherent optical converter.

We now consider the depth-of-focus of the lenses used (especially the imaging lenses used in MTF tests and in imaging the input data onto an SLM). An ideal lens focuses a plane wavefront to a point of zero dimensions. However, all lenses have some aberrations and a non-infinite aperture. Thus, in practice, there are variations δx, δy, δz in the focused spot. The depth-of-focus variation δz (along the optical z axis) determines the accuracy with which the image plane (the SLM) must be positioned. For an SLM this $dz = \delta f_L$ variation is related to the allowable thickness of the photoconductor layer in the SLM. Conversely, if the SLM and its photoconductor are fixed (as is usually the case), then the necessary depth-of-field δf_L of the associated imaging lens is determined.

Specifically, if the photoconductor is d μm thick, then the associated imaging lens must have a depth-of-focus $\delta f_L > d$ μm. Accordingly, the spatial frequency limit to which such a system should be used is $\overline{V}max = 16 f_L/D\delta f_L cy/\mu m$. Conversely, if the lens used has a $\delta f_L = d_L \mu m$, then the SLM's photoconductor should be less

than d μm thick and imaging MTF data beyond the same V_{max} limit should not be taken. The above values assume that the photoconductor is active throughout its entire volume or thickness and ignores photoconductor response variations normal to the optical axis.

In practice a lens with a $\delta f_L < d$ may be acceptable depending upon the magnification used and the photo-carrier generation and charge distribution formulation process. The best philosophy is to use a lens with $\delta f_L > d$.

The depth-of-focus of a lens of focal length f_L and aperture D used at wavelength λ in a 1:1 imaging system is [4.17]

$$d = \delta f_L = 8\lambda(f_L/D)^2 \tag{4.21}$$

the uncertainty in the location of the focus in the plane perpendicular to the optical axis is [4.17]

$$\delta y = (\lambda/4) \ (f/D) \ . \tag{4.22}$$

The three major shortcomings of imaging MTF experiments are: the lack of gray scale SLM information and the reliance on binary imagery, the lack of second harmonic distortion information about the SLM, and primarily the dependence of such an experiment on operator attitude and experimental error. In Section 4.5.7, we discuss the depth-of-focus of the lens issues associated with such experiments and its relevance to the SLM thickness. These issues are of major concern in SLMs such as the prom in which the SLM is itself both electro-optic and photo-conductive and is thick. In the photo-DKDP SLM, the photo-conductive layer is thin and determines the depth-of-focus requirement of the associated imaging optics used.

In most practical applications, a transparency of the input data is not available for imaging onto the SLM and thus the results of such an MTF test are of little practical use and actual applications in which the SLM will finally be used. In

most practical imaging SLM applications, the input is an ambient scene, the image from a TV monitor or similar cases. In such instances, the bias level of the input scene will be large and its contrast low. The reflective imaging MTF test was an attempt to produce such a realistically equivalent MTF test system. High bias level, scatter, and large background noise are the key features that characterize such an input. Experimental component and output measurement system difficulties make the practical use of such an MTF technique less attractive.

When the input data is recorded point-by-point on an SLM, the edge MTF test is appropriate since it directly models the actual data recording situation. However, experimental difficulties associated with this MTF technique add even more stringent difficulties to an already unreproducible imaging MTF experimental procedure.

Interferometric MTF measurement techniques are clearly the most easily performed and most reproducible ones. The major difficulty associated with such tests is whether the lens system and data recording technique actually used has the adequate depth-of-focus and focusing accuracy of the interferometric recording method. The interferometric MTF technique yields the largest possible resolution for the device. If the bias level of the recorded data and the input modulation in such a test are properly chosen to model the actual case, the results of such a test are appropriate. In Section 4.5.7, we discuss the depth-of-field issue associated with the lenses in such an experiment. In SLMs with separate photo-conductor and electro-optic layers, the thickness of the photo-conductor determines the depth-of-focus necessary in the lens system. This MTF test method is appropriate for all interferometric filter plane SLM applications. It is also appropriate for most signal processing applications in which the input signal is recorded on a carrier.

4.5.7 Test Component Selection

The polarizers used in the SLM test system should have a contrast ratio ten times larger than that of the SLM. The glass plate polarizers (dichroic polarizers) from Miles Grinot have been found to be the best of this type. In most experiments,

beam splitter cubes were used. In the FT of the square aperture and in the square-wave tests, a two inch metalized beam splitter was employed. When calculating rms OPD and for similar DKDP interferogram tests, a six inch dielectric beam splitter was used on the readout light side and a two inch dielectric beam splitter on the write side.

The available beam splitters are generally specified for a given direction of polarization. We have found that all beam splitters are polarization dependent, i.e., the ratio of the intensities of the two split beams changes with the polarization of the input light. We have also found that the metalized beam splitter has less polarization dependence (50/50 to 40/60) than the dielectric beam splitters (50/50 to 30/70). The beam splitters we utilized have anti-reflective coatings on one side and beam splitter coatings on the other. Care should be taken to orient the beam splitter coatings to the input side to reduce spurious reflections. Thus the corresponding spatial frequency at which one will encounter problems in the use of such a lens is determined by δy as

$$\nu_{max} = \tfrac{1}{2}\delta y \ .$$

(4.23)

For three imaging lenses in our laboratory, we have tabulated the necessary lens parameters in Table 4.7.

Table 4.7   Imaging Lens Parameters

LENS	f_L(mm)	f_L/D (min/max)	δf_L(um) (min/max)	δy(um) (min/max)	ν_{max}(cy/mm)
NIKON MICRO-NIKKOR	55	3.5/32	62/5185	0.55/5	900/99
NIKON MICRO-NIKKOR	105	4/32	81/5185	0.63/5	789/99
RAPTAR COPY	206	4.5/32	102/5185	0.71/5	702/99

As we can see, there is no depth-of-field problem associated with the use of any of these lenses for the photo-DKDP SLM. Thus, we prefer to use our best lens

(Nikon, 55mm, F/3.5) since the above Table does not include other aberration effects present in all lenses. Because of the thin 10μm thickness of the Se photoconductor in the photo-DKDP SLM and because the charge carriers are generated within a thin (approximately 1μm for short exposures) layer of the Se, any imaging lens with a depth-of-focus above 10μm (or possibly 1μm) will be adequate and will yield equivalent resolution data to that obtained from an interferometric MTF test.

In our experiments, long exposures were used. So, let us assume that the sensitive thickness of the Se is 10μm. We thus require an imaging lens with δf_L = 10μm. f_L is related only to the F- number f_L/D of the lens and the wavelength λ of the light used. From (4.21)

$$f_L/D < \left(\frac{\delta f}{8\lambda}\right)^{\frac{1}{2}} = \frac{10}{8(0.63)}^{\frac{1}{2}} = (1.97)^{\frac{1}{2}} = 1.4 \quad , \tag{4.24}$$

or a lens with f number 1.4 will suffice and would let us reach a frequency limit of

$$_{max} = \frac{16(f_L/D)}{\delta f_L} = 2.26 \times 10^3 \text{cy/mm} \quad . \tag{4.25}$$

Clearly, other aberrations will start dominating before we reach this limit since our analysis has assumed diffraciton limited case only.

4.6 Noise Experiments

Our general approach to the evaluation of noise in an SLM was advanced in Chapter 2. Here, we thus only highlight our experimental data and test systems for the photo-DKDP SLM.

4.6.1 Interferometric OPD

The most common measure of noise in a SLM for coherent optical data processing applications is the use of an interferometric system to obtain OPD data. As we have described elsewhere [4.18,4.19], spatial OPD maps as functions of the aperture and spatial frequency are necessary. An automated spatial OPD data acquisition system

[4.20] has also been described by us. Such data has been obtained by us [4.21] for the LCLV. In this test and experimental program, only interferogram data were obtained. The test system used is shown in Figure 4.26. The components used are included in Table 4.8. In the interferometer the photo-DKDP acts as a mirror in one of the arms of the interferometer. This arrangement with the photo-DKDP operated in reflectance rather than transmission mode is in agreement with the actual use of the device in practice. The surface quality of the Se layer is also not of concern since it is usually written on with non-coherent light. The six inch beam splitter used in this test system was employed because of the wide field of view it provides at the 45° angle at which it is operated.

In Figure 4.27, we show the resultant fringe pattern obtained on the DKDP at room temperature, at -20°C and -50°C. In each of these photographs, the fringe pattern was allowed to stabilize before the photograph was taken. From these fringe patterns, we see that the OPD of this SLM is poor by comparison to others (λ to $\lambda/2$ over the full area, λ to $\lambda/4$ over the central $2 \times 2 \text{cm}^2$ region) and that the OPD pattern changes with temperature. This change is due to stresses in the SLM, non-uniform cooling, the vibration effects of coolant flow through the first stage Peltier cell cooling system, and physical changes in the thickness of the DKDP layer with temperature.

4.6.2 Scatter Level Tests

Another source of noise in the SLM besides phase or OPD errors is scatter level noise. To measure this noise source and its effects, we form the FT of a square aperture using the photo-DKDP SLM as a relay and without the photo-DKDP. The test system used is shown in Figure 4.28 and the resultant output data in Figures 4.29a and b. A $7 \times 7 \text{mm}^2$ input aperture was used to better enable the full output FT plane pattern to be scanned. A larger input SLM area should be used in practice and alternate lens and detector scanning systems employed. The square input aperture is reflected from a mirror in place of the photo-DKDP through the same lens system.
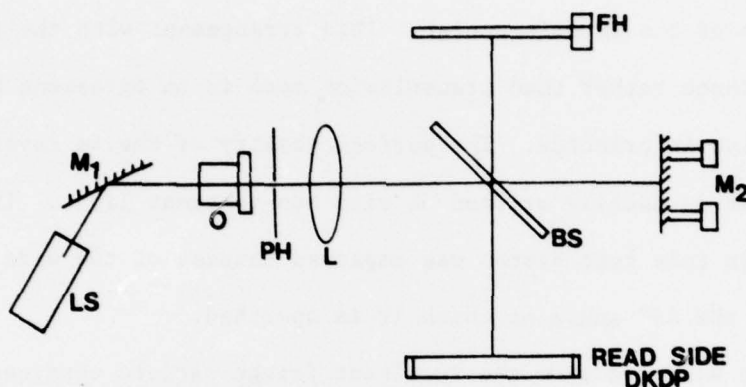
Figure 4.26   Interferometric OPD System for the Photo-DKDP

Table 4.8   Components used in the Interferometric OPD System of Figure 4.26

LS: 633nm laser

M_1:   Mirror

M_2:   Dielectric mirror 4"

BS: NRC 6" dielectric beam splitter

DKDP: DKDP crystal assembly with read side towards the
        beam splitter

FH: Polariod film holder

O: 20 x objective

PH: 5 μ pinhole

L: 381mm collimating lens

(a) Room Temperature
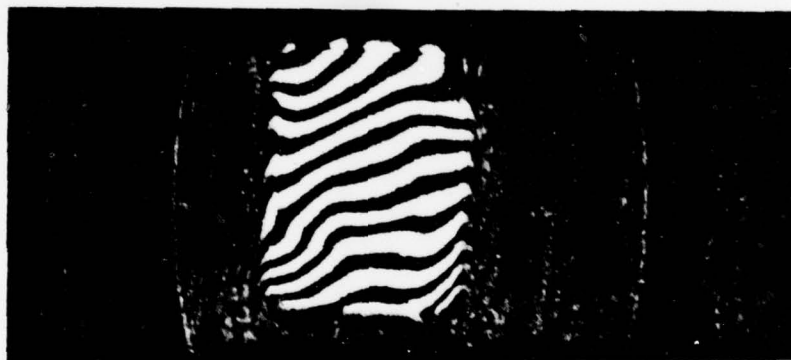
(b) −20°C
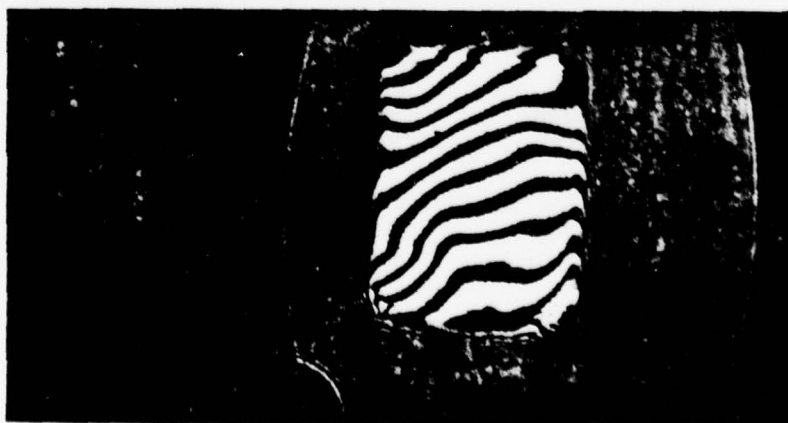
(c) −50°C (Transition Temperature)

Figure 4.27 Interferograms Obtained from the Photo-DKDP at Different Temperatures

This determines the maximum obtainable scatter level or system dynamic range due to the optics alone. Comparing the plots in Figure 4.29, we find that the photo-DKDP adds an additional 2-4dB to the system noise level and decreases the dynamic range obtainable by the same amount. The optical system alone shows a 51dB dynamic range or scatter level, whereas the photo-DKDP system exhibits nearly a 50dB dynamic range or scatter level.
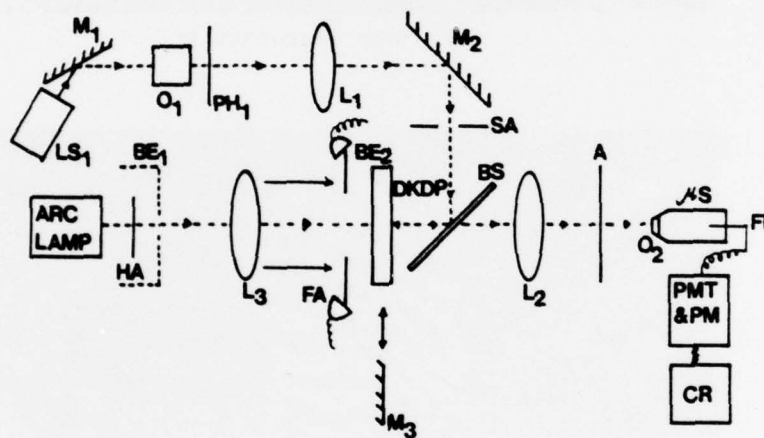
Figure 4.28   Scatter Level Data Acquisition Test System

4.6.3   Squarewave FT Tests

From the FT of a squarewave pattern imaged onto the SLM, we can (by analysis of the presence of and magnitude of the various odd and even orders) determine the interharmonic distortion and thickness variations in an SLM. This test is usually most appropriate and is noted here. In the photo-DKDP SLM, the many wedged layers in the device resulted in numerous spurious defracted orders in the FT pattern. Thus, for this SLM, this test was not as useful as it has proven to be for other SLMs.

4.6.4   Non-Linear Interferometric MTF Experiments

In Chapter 2, we very clearly demonstrated the usefullness of linear and non-linear interferometric MTF data in determining interharmonic distortion and the
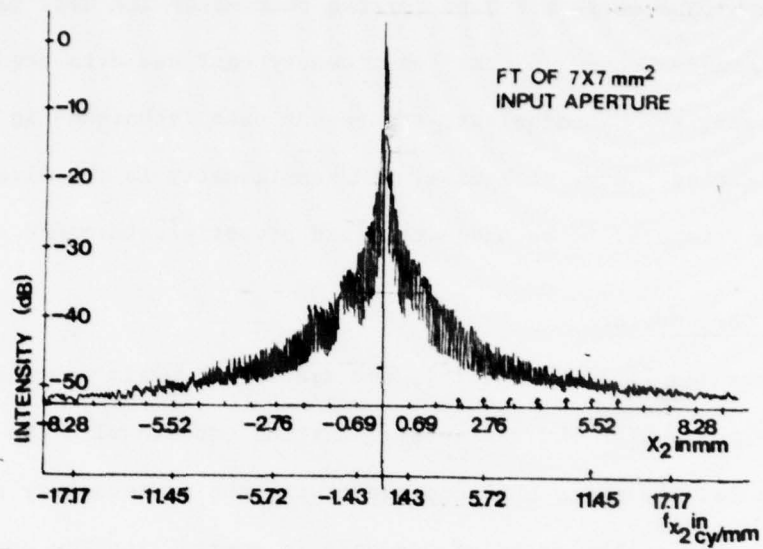
(a) Empty Aperture
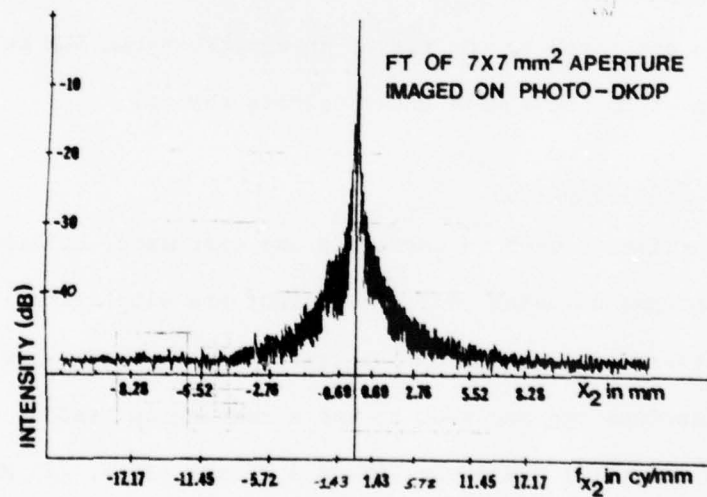
(b) Real-Time Using the Photo-DKDP

Figure 4.29   Scatter Level Tests Performed on the Photo-DKDP SLM
(FT of a Square Input Aperture)

linearity of the sensitometry and MTF data on the SLM under test. Our linear and non-linear interferometric MTF data for the photo-DKDP SLM were far less impressive in their difference because of the sensitometry test and data acquisition system issues noted earlier. Nonetheless, the use of such techniques is a vital key SLM test and evaluation issue. Likewise, SLM sensitometry is the first and most important SLM parameter to be adequately and properly determined.

4.7 Bravais Compensator

In References [4.2] and [4.16], the use of a Bravais compensator in conjunction with the photo-DKDP SLM was noted. Initial concern with the importance of the use of this accessary photo-DKDP component were not as necessary as first felt. Specifically, this component is of use only in controlling the optical bias of the SLM. A simple $\lambda/4$ wave plate performs equally well and is far less expensive. The purpose of this component is simply to introduce a uniform phase shift or retardation across the SLM. This technique is most attractive to produce contrast reversal or positive to negative conversion and equiluminous contour generation. Such a technique can be automated by the use of an electro-optic SLM to uniformly rotate the polarization of an input wave under voltage control.

4.8 Cone Angle Considerations

In the experiments we have performed and discussed, collimated readout light was used. Advantages of using collimated light are simplification of readout optics and maximum contrast available from the crystal as we shall show later. However, in practical applications one may need to use a converging readout beam. Obvious applications of this are: (1) use of an SLM in a filter plane, (2) magnification of an image on the DKDP without sacrificing read light energy and (3) use of a converging beam FT system to achieve scale change and reduce lens requirements.

The effect of operation of the DKDP in a converging light of a given cone angle has been studied in [4.5] and [4.14]. It has been shown that the first-order

effect is to produce output light in the off-state, even with crossed polarizers. This reduces the total contrast available from the crystal. As we shall show, the effect varies as the fourth power of the cone angle. DKDP is a uniaxial crystal in the absence of an external voltage. In a readout scheme using collimated light, linearly polarized light is incident along the optic axis ofter reflection from the mirror, it emerges from the crystal without change and is thus cancelled by the analyzer. Now consider the case when the incident light is incident at an angle to the optic axis of the crystal.

The necessary geometry is shown in Figure 4.30. We consider the geometry where: a is the DKDP crystal thickness = 160μm; θ_i is the half angle of the cone of the converging light; θ_r is the angle of refraction in DKDP; Z is the optic axis of DKDP; n_0 = 1.4677 is the index of refraction along x and y; and n_e is the index of refraction along the optic axes.
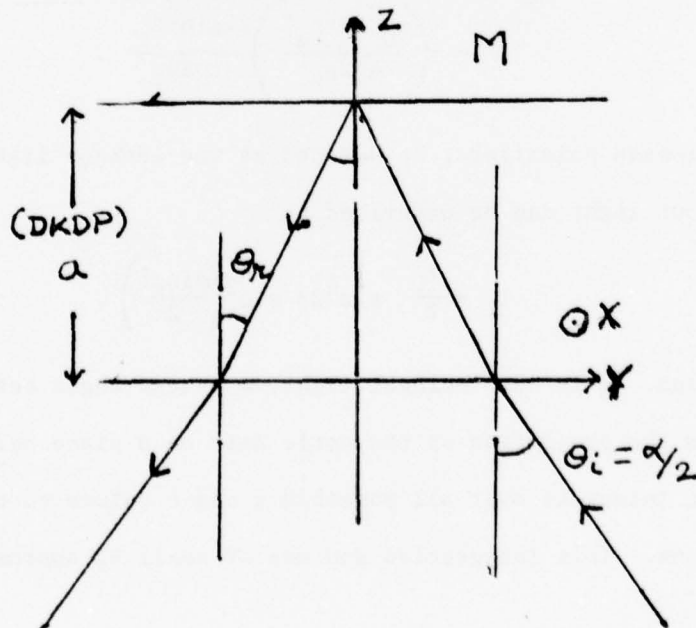

Figure 4.30 Geometry for Cone Angle Calculations

Light polarized normal to the plane of incidence of the crystal sees a refractive index n_0, whereas input light polarized in the plane of incidence of the crystal sees a refractive index that depends on θ_r, n_e and n_0. As we showed [Chapter 3], this index is

$$n_e(\theta_r) = \frac{n_e}{\sqrt{\sin^2\theta_r + \frac{n_e^2}{n_0^2}\cos^2\theta_r}} \quad . \tag{4.26}$$

This expression can be derived using Maxwell's equations and Fresnel's equations for wavenormals. We are interested in the phase introduced between the two polarizations of the wave. This depends on $\Delta n(\theta_r) = n_0(\theta_r) - n_e(\theta_r)$. Using a samll angle approximation, we obtain

$$\Delta n(\theta_r) = \frac{n_0}{2}\left(\frac{n_0^2 - n_e^2}{n_e^2}\right)\sin^2\theta_r \quad . \tag{4.27}$$

The observed phase shift is given by $[2\pi\Delta n(\theta_r)d]/\lambda$, where $d = 2a/(\cos\theta_r)$ is the path travelled in the crystal. Approximating $n_0\sin\theta_r$ by $\sin\theta_i$, we obtain an expression for the phase shift given by

$$\Gamma = \pi\left(\frac{n_0^2 - n_e^2}{n_e^2 n_0}\right)\frac{2a\sin^2\theta_i}{\lambda\cos\theta_r} \quad . \tag{4.28}$$

For a pair of crossed polarizers, I_L defined as the leakage light due to the converging readout light can be described by

$$I_L = \frac{I_0}{2}\sin^2 2\phi \sin^2\left(\frac{\Gamma(\theta_r)}{2}\right). \tag{4.29}$$

In this expression, I_0 is the incident light, ϕ is the angle between the incident polarization and the projection of the optic axis on a plane perpendicular wavenormal. We must integrate over all possible ϕ and θ values to consider all the rays within a cone. This integration and use of small θ_r approximations yields the expression

$$I_L = \frac{I_0}{2} \left(\frac{1}{6}\right) \frac{\pi}{2} \left[\left(\frac{n_0^2 - n_e^2}{n_e^2 n_0}\right) \left(\frac{2a}{\lambda}\right) \left(\frac{\alpha}{2}\right)^2\right]^2 \tag{4.30}$$

This expression shows that I_L increases proportional to α^4 (i.e., the fourth power of the convergent beam angle $\theta \propto \alpha$). The maximum light available from the DKDP light valve (with our specifications) is $I_0/2$. Thus, the available contrast is found to be

$$\text{Contrast(max)} = 6 \left[\frac{2}{\pi} \left(\frac{n_e^2 n_0}{n_0^2 - n_e^2}\right) \left(\frac{\lambda}{2a}\right) \left(\frac{2}{\alpha}\right)^2\right]^2 = \frac{I_{max}}{I_{min}} . \tag{4.31}$$

For $\alpha = 1/10$ rad. this contrast is $\simeq 10^3$. In practical applications one would have cone angles below 1/5 radians. Even in this worst case, converging light is not a problem since one still has contrast of 75.

4. REFERENCES

4.1   G. Marie and J. Donjon, Proc. IEEE, 61, 942 (1973).

4.2   G. Marie, et.al., Advances in Image Pickup and Display Devices, B. Kazan, Editor, Academic Press, New York, pp. 225-302 (May 1974).

4.3   D. Casasent, IEEE, ED-20, 1109 (1973).

4.4   D. Casasent and W. Keicher, J. Opt. Soc. Amer., 64, 1575 (1974).

4.5   B. H. Billings, J. Opt. Soc. Amer., 39, 797 (1949).

4.6   J. L. Hartke and P. J. Regensgurger, Phys. Rev., 139, A 970 (1965).

4.7   D. M. Pai and S. W. Ing, Jr., Phys. Rev., 173, 729 (1968).

4.8   F. Dumont, et.al., Phillips Tech. Rev., 34, 274 (1974).

4.9   Private communications from RTC LA Radiotechnique - Compelec.

4.10 M. D. Tabak and P. J. Warter, Jr., Phys. Rev., 173, 899 (1968).

4.11 B. Tatian, J. Opt. Soc. Amer., 55, 1014 (1965).

4.12 K. Rosenhauer and K. J. Rosenbruch, Optica. Acta., 4, 221 (1957).   (German)

4.13 D. Dutton, Appl. Optics, 14, 513 (1975).

4.14 W. R. Roach, IEEE, ED-21, 453 (1974).

4.15 J. Donjon, et.al., Acta. Electronica, 18, 187 (1975).   (French)

4.16 G. Marie, Ferroelectrics, 10 (1976).

4.17 M. Born and E. Wolf, Principles of Optics, New York, Macmillan (pp. 436-440, Depth-of-Focus) (pp. 669,771, Cone Angle) (1964).

4.18 Reference 6.1.

4.19 T. Luu and D. Casasent, Appl. Optics, 18, 791 (1979).

4.20 Reference 6.2.

4.21 D. Casasent, BMDATC Report (unpublished) (1978).

4.22 J. C. Dainty and R. Shaw, Image Science, Academic Press, New York (pp. 244-6) (1974).

5. PHOTO-DKDP LIGHT VALVE IN OPTICAL DATA PROCESSING

Abstract

Various real-time optical data processing experiments using the photo-DKDP spatial light modulator are described. These include the performance of image subtraction and contrast reversal directly on the light valve and their application to practical pattern recognition situations in which the input and reference objects differ. Examples of real-time optical correlation on coded waveforms for signal processing are presented and the accuracy of the optically produced ambiguity function outputs are compared to the theoretically expected ones. Real-time optical image pattern recognition experiments are also presented together with comparative data obtained with off-line correlations performed using film.

5.1 Introduction

To fully utilize the advantages of an optical processor, real-time and re-usable replacements for film are necessary in most data planes of an optical system. The system components used to achieve this are known as spatial light modulators (SLMs) [5.1,5.2]. In this paper, we consider the use of the photo-DKDP [5.3-5.5] SLM in various optical data processing applications. Following a brief description of this SLM and its operation (Section 5.2), we describe its use in various real-time optical data processing applications. Since this SLM is an integrating and storage mode transducer, several special operations are possible with it. These include image addition, subtraction, and contrast control, as noted earlier [5.6]. Several new examples of these operations are presented in Section 5.3 together with a discussion of their use in several practical pattern recognition applications in which the input and reference imagery differ. Since correlation is one of the most powerful operations possible in an optical (or any) data processor, we emphasize such applications in image pattern recognition (Section 5.4) and signal processing

with coded waveforms for ambiguity function generation (Section 5.5). Included in our study is a discussion in Section 5.6 of the accuracy of optically produced ambiguity function outputs and a comparison of the optical pattern recognition correlations obtained using the DKDP SLM to those obtained using film.

5.2 Photo-DKDP Spatial Light Modulator

The photo-DKDP SLM is manufactured by LEP in France. The unit we have evaluated and experimented with is one of the first available outside of France and the first one within the United States. It has been extensively described in many papers [5.1-5.6] and thus the present description is brief. The device consists of a $40 \times 30mm^2 \times 160\mu m$ thick potassium dideuterium phosphate (DKDP) crystal, nine layer dielectric mirror (M) and $10\mu m$ thick Selenium (Se) photoconductor sandwiched between two transparent outer electrodes (E_1 and E_2). The SLM is housed in a vacuum enclosure and is operated at the transition temperature ($-52°C$) of the DKDP.

Data is written on the device by exposing the Se side of the SLM to λ_W write light (we used $\lambda_W = 514nm$, although the photo-sensitivity of the Se photoconductor peaks at 400nm) with the front electrode E_1 positive or negative. With E_1 positive, a positive latent charge image is produced on M and across the DKDP in the exposed areas. With E_1 negative, a negative latent charge image results, with holes providing the charge transport when E_1 is positive and electrons when E_1 is negative. For readout and storage, E_1 and E_2 are shorted to ground. The latent charge image across the DKDP is readout in reflection from the DKDP side of the SLM. By the Pockels' effect [5.7], the spatial voltage distribution across the DKDP produces a corresponding spatial variation in the reflected output light (we used $\lambda_R = 633nm$) observed between crossed polarizers. Pure phase modulation is also possible if the direction of polarization of the λ_R light and the crystallographic axes of the DKDP are properly chosen. Erasure is achieved by flooding the Se side of the SLM with λ_E erase light (either narrowband or broadband λ_W light) with E_1 and E_2 shortened to ground.

The first SLM data necessary is its sensitometry. Because image addition and subtraction applications were to be considered (in which the DKDP was subjected to multiple exposures with the polarity of E_1 unchanged for addition or reversed for subtraction), sensitometry data were obtained both with E_1 positive and with E_1 negative. Because of the dependence of the photo-sensitivity of Se on the field across it [5.5], the resultant sensitometry curves were found to differ, depending on the polarity of E_1. We found this difference to be more apparent when long exposure times are used. Since such sensitometry data are necessary to determine the input bias level and input exposure range to be used, attention must be given to obtaining sensitometry data that adequately models the subsequent image and pattern recognition applications. We thus obtained sensitometry data on the photo-DKDP SLM for both polarities of applied voltage at exposure times comparable to those used in subsequent data processing applications.

5.3 Image Addition, Subtraction and Contrast Reversal

By successively exposing the photo-DKDP to two images with E_1 positive in both cases, the latent charge patterns for each image are added across the DKDP. However, because of the voltage dependent photo-sensitivity of the Se photoconductor, an exact addition of the two images may not result. Short exposure times (as would be used in most practical applications) can appreciably reduce such differences. To realize image subtraction, the photo-DKDP is successively exposed to two images with the polarities of writing (holes are the transport carriers when E_1 is positive and electrons when E_1 is negative) and without a voltage dependent photo-sensitivity for Se, erasure should be feasible. By properly doping Se, $\mu\tau$ (μ is mobility and τ is carrier transit time) and quantum efficiencies for holes and electrons can be obtained in the proper ranges that equal sensitometry results for hole and electron transport. Short exposure times can greatly decrease the field dependence of the photo-sensitivity of the Se during initial writing of one image. However, in image addition and subtraction applications, when multiple exposures are used, a spatially

varying latent charge pattern will exist across the DKDP due to the first exposure. Thus the field dependence of the photo-sensitivity of Se must be considered and is of concern in all image addition and subtraction applications.

A more detailed discussion of such device issues will be the subject of a future paper. For now, we concentrate on the use of operations such as image addition and subtraction. In most practical image pattern recognition applications, the input and reference imagery differ for many reasons. Two applications which we have extensively considered involve the correlation of infrared and multi-sensor imagery [5.8]. In such cases the dominant portions that are common between two such images are the edges [5.9]. Thus, to correlate two such images, an obvious preprocessing step is to differentiate one or both images prior to correlation. This preprocessing operation can be realized in real-time directly on the photo-DKDP SLM by exposing the device to one image with E_1 positive and then exposing the SLM to a displaced or defocused version of the same image with E_1 negative. The net result of two such exposures is the subtraction of the two images. The resultant latent charge pattern across the DKDP is the horizontal or vertical 1-D derivative of the first image (if the second image is a displaced version of the first image) or a 2-D derivative (if the second image is a defocused version of the first image).

Dumont and other French researchers [5.5,5.6] have described such operations in detail. However, their applications to the aforementioned optical pattern recognition problems, the issues of voltage dependent photo-sensitometry, non-equal sensitometry for holes and electrons and the issue of long exposure times are noted here for the first time. In Figure 5.1, we show the reconstructed image of an Air Force test chart recorded on the photo-DKDP with E_1 positive (Figure 5.1a) and with E_1 negative (Figure 5.1b) and the result of a double exposure with the image displaced horizontally (Figure 5.1c) and then vertically (Figure 5.1d) between exposures. In obtaining Figures 5.1c and 5.1d, the polarity of E_1 was reversed between the two

exposures. Because of the long exposure times involved in this experiment, its use at present was restricted to binary imagery. It is also possible to realize low-pass, band-pass or high-pass filtered versions of an image by conventional Fourier transform plane spatial filtering. An example of such true real-time high-pass filtering or image differentiation using photo-DKDP is shown in Figure 5.2. In this experiment, the original input pattern was recorded on photo-DKDP (its reconstruction is shown in Figure 5.2a). The reconstructed output image (with a high-pass Fourier plane filter in place) is shown in Figure 5.2b. Such filtering operations are also of use in image enhancement and restoration [5.11].

5.4 Real-Time Image Pattern Recognition

The schematic of the optical system used for all image pattern recognition correlation experiments is shown in Figure 5.3. This basic optical system is a frequency plane correlator [5.12]. Although many other optical pattern recognition system architectures exist [5.13] (many of which are more appropriate for different practical applications and for use with real-time SLMs), the frequency plane correlator is most appropriate for cases in which the reference image is known in advance. The conventional frequency plane correlator system has been extensively modified as shown in Figure 5.3 to allow the use of the photo-DKDP SLM as the input transducer. The input data to be processed is placed at P_{01} and imaged onto the photo-DKDP at P_{02} in white light by lens IL (209mm focal length) with 1:1 imaging. The Fourier transform of the data recorded on the photo-DKDP is formed by lens FL_1 at P_1. To record the matched spatial filter to be used at the Fourier transform plane P_1, the polarization of the signal and reference beams must be the same for interference to occur. The pattern recorded on the photo-DKDP is thus readout in reflection using a vertically polarized He-Ne laser beam. However, because of the cross polarizer readout, the light leaving the polarizing beam splitter (PBS) in reflection from the DKDP is horizontally polarized. The vertical polarization of the reference beam was thus converted to horizontal polarization by the combination of the $\lambda/4$

plate and linear polarizer (POI) as shown. The interference of these signal and reference beams are then formed at P_1. The subsequent pattern at P_1 is the desired matched spatial filter of the reference pattern initially recorded on the photo-DKDP.

Once the matched spatial filter of the key or reference object to be located has been recorded at P_1, the reference pattern on the photo-DKDP is erased and a new image (one that includes the key object) is placed at P_{01} and imaged onto the photo-DKDP at P_{02}. When this input image on the photo-DKDP is read out and imaged through the matched spatial filter at P_1 (with the reference beam blocked), the correlation of the input and reference images appears at P_2. In Figure 5.4a and 5.4b, we show the real-time reconstruction of a 23 x 25mm^2 input and the 6 x 6mm^2 portion of this image used as the reference or key object to be located. In Figure 5.4c, a pseudo 3-D isometric view of the real-time optically produced output correlation plane pattern is shown. A shorter 300mm focal length second Fourier transform lens (FL$_2$) was used to provide a more concentrated output plane P_2 intensity pattern. Scans of this output correlation plane pattern obtained with a scanning photometric microscope showed an output correlation plane SNR of 10:1.

In Figure 5.5, we show analogous results for an optical word recognition application. In this case, the word PROFESSOR was recorded on the photo-DKDP SLM and a matched spatial filter of it was recorded on Kodak high-speed holographic film plates at P_1 as described above. When the input text of Figure 5.5a (with 4 occurrences of the key work, PROFESSOR) was placed at P_{01}, imaged onto the photo-DKDP at P_{02}, and read out in reflection (with the reference beam blocked), the output correlation again appears at P_2. A pseudo 3-D isometric view of the output P_2 correlation plane pattern is shown in Figure 5.5b. From these data, we see that 4 output correlation plane peaks occur and that their locations correspond to the four locations of the key work PROFESSOR in the input text of Figure 5.5a. From cross-sectional scans of the output correlation plane pattern, the peak intensities of the four output correlation peaks corresponding to each key word in the input were found to be 30, 28,

and 27 (in relative units) and the maximum cross-correlations were found to lie between 6 and 7 units (same relative scale). In Section 5.6, we examine these correlation plane outputs for this optical word recognition application in more detail and include comparative data on analogous output correlations obtained using film rather than the photo-DKDP as the input media.

5.5 Real-Time Optical Signal Processing Applications

Many diverse optical correlator systems have been used to process coded signal waveforms [5.14]. In the most sophisticated cases, the desired signal processing system output is the ambiguity function [5.15] (a plot of range vs. Doppler using the received signal and the coded reference waveform). In this Section, we discuss two new optical ambiguity function generation systems and include examples of their realization in real-time using the photo-DKDP SLM as the real-time input transducer.

One of the simplest and thus one of the most attractive optical ambiguity function processors was first described by Said, et.al. [5.16] and more recently by Marks [5.17]. In this optical ambiguity function processor, a 1-D coded signal $f(x) = f(t)$ is first replicated in the vertical or y direction, yielding a 2-D function $f(x,y)$. If this input pattern is then rotated by an angle θ, the resultant function becomes $f(x \cos \theta + y \sin \theta)$. For the particular case when $\theta = +45°$ or $-45°$, we find that the input pattern reduces to $f[(x \pm y)/\sqrt{2}]$. Superimposing these $\pm 45°$ replicated and rotated versions of the original pattern, we find the resultant input plane function to be described by

$$f[(x+y)/\sqrt{2}]f[(x-y)/\sqrt{2}] \quad . \tag{5.1}$$

For a simple single pulse input signal of width T, the resultant superposition of these two functions is a diamond-shaped pattern. The 1-D horizontal Fourier transform of Equation (5.1) is

$$U_2(\nu,y) = \int_{-\infty}^{\infty} f\left(\frac{x+y}{\sqrt{2}}\right) f\left(\frac{x-y}{\sqrt{2}}\right) \exp(-j2\pi\nu x)dx \quad , \tag{5.2a}$$

where ν is the frequency variable associated with x. With the variable substitutions x' = $(x+y)/\sqrt{2}$ and y = τ, we obtained

$$U_2(\nu,\tau) = \sqrt{2} \exp(j2\rho\nu\tau) \int_{-\infty}^{\infty} f(x')f(x' - \sqrt{2}\tau) \exp[-j2\pi(\sqrt{2}\nu)x']dx'$$

$$= \sqrt{2} \; \chi(\sqrt{2}\nu,\sqrt{2}\tau) \exp(j2\pi\nu\tau) \quad . \tag{5.2b}$$

The observed output plane intensity distribution is thus

$$|U_2(\nu,\tau)|^2 = 2|\chi(\sqrt{2}\nu,\sqrt{2}\tau)|^2 \quad . \tag{5.3}$$

This output plane pattern is a scaled version of the radar ambiguity function χ defined by

$$\chi(\nu,\tau) = \int_{-\infty}^{+\infty} f(x) \; f(x-\tau) \exp(-j2\pi\nu x)dx \quad . \tag{5.4}$$

The waveform used to experimentally produce the ambiguity function described in Equation (5.3) was a double pulse signal with pulse width T and separation T between pulses. This waveform is described mathematically by

$$f(t) = (1/\sqrt{2}T) \; rect \; [(t\pm T)/T] \quad . \tag{5.5}$$

After replacing this function in the y direction and superimposing $\pm 45°$ rotated versions of it, the resultant input plane pattern consists of 4 diamond-shaped subpatterns as shown in Figure 5.7a. To produce the desired ambiguity function for such a double pulse input, we form the 1-D horizontal Fourier transform of this pattern as required in Equation (5.2a). This is accomplished by the system shown in Figure 5.6. In this system the pattern at P_{01} (Figure 5.7a) is imaged onto the photo-DKDP SLM at P_{02}. Cylindrical lens L_c and Fourier Transform lens FL in Figure 5.6 image vertically and form the Fourier transform horizontally. The 1-D horizontal Fourier transform of Equation (5.5) thus appears at P_1. It consists of 3 terms:

$$x(\nu,\tau) = \begin{cases} (1/T) \ (T-|\tau|)\text{sinc}[\nu(T-|\tau|)]\cos\,(2\pi\nu T)\,\exp\,(-j\pi\nu\tau) & |\tau| \le T \\ (1/2T)(T-|\tau|)\text{sinc}[\nu(T-|\tau|)]\exp\,(-j\pi\nu\tau) & T \le |\tau| \le 2T \\ (1/2T)(3T-|\tau|)\text{sinc}[\nu(3T-|\tau|)]\exp\,(-j\pi\nu\tau) & 2T \le |\tau| \le 3T \\ 0 & |\tau| \ge 3T \end{cases} \tag{5.6}$$

Each of these items is located in a different region of P_1 and P_1 is zero elsewhere. As before, τ is the range shift parameter and ν is the Fourier transform spatial frequency variable. The resultant ambiguity function, optically produced in real-time at P_1 using the photo-DKDP SLM at P_{02}, is shown in Figure 5.7b. An isometric pseudo 3-D output display is used to better convey the output plane pattern. To analyze this pattern in more detail, we consider the theoretical cross-sectional scan of Equation (5.6) along the Doppler (ν) axis

$$|\chi(\nu,0)|^2 = (1/\pi\nu T)\ [\cos(2\pi\nu T)\ \sin(\pi\nu T)]^2 \tag{5.7}$$

and along the range or τ axis

$$|\chi(0,\tau)|^2 = \begin{cases} [(T-|\tau|)]^2 & |\tau| \le T \\ [(T-|\tau|)2T]^2 & T \le |\tau| \le 2T \\ [(3T-|\tau|)/2T]^2 & 2T \le |\tau| \le 3T \\ 0 & |\tau| \ge 3T \end{cases} \tag{5.8}$$

Extensions of this system to complex functions are described in [17].

The A-scope cross-sectional scans of the optically produced ambiguity function in Figure 5.7b are shown in Figure 5.7c and Figure 5.7d. In Section 5.6, we consider the accuracy of these real-time optically produced outputs, compared to the expected shapes predicted by Equations (5.7) and (5.8). For now, we note that along the ν axis we expect a sinc function distribution with a cosine carrier as in Equation (5.7) and as shown in Figure 5.7c. Along the τ axis we expect 3 peaks (as predicted by Equations (5.6) and (5.8) and as shown in Figure 5.7b with amplitudes predicted by Equation (5.8) and as shown in the cross-sectional scan in Figure 5.7d.

The second optical signal processing ambiguity function processor to be considered addresses a very different application. In this scenario [5.18], the input signals (whose ambiguity function is desired) are narrow-band, basebanded complex time-histories of the passive signals received form a single source at two separated detectors. The objective of the required processing is to determine the differential range $(\tau_1 - \tau_2)$ and Doppler $(\nu_1 - \nu_2)$ of the source from the passive, narrow-band, received signals. The resultant real-time version of the optical signal processor used in the analysis of such data is shown schematically in Figure 5.8. In this case, a modified image plane correlator optical system architecture (first described by Cutrona, et.al. [5.19] and modified as shown) for real-time application to produce complex correlations by single sideband filtering and input preprocessing is used. In this system, the basebanded narrow-band signals received at the two detectors are converted to real and positive signals (s_1 and s_2) by quadrature modulation and addition of a bias term (this is achieved by digital and electronic preprocessing). The signals, received at one detector is replicated on all N lines at P_{01} in Figure 5.8 and subsequently imaged onto the photo-DKDP light valve at P_{02} of Figure 5.8. When readout with the $\lambda_R = 633$nm light shown, this P_{02} pattern is imaged onto P_2 in Figure 5.8. At P_2, the quadrature modulated and biased version of the second received signals are recorded on N lines with a τ or range shift introduced on successive vertical lines. At P_1, single sideband filtering is applied to produce a complex signal pattern incident on P_2.

In more mathematical terms, we describe the original basebanded received signals as

$$s(x) = s^R(x) + js^I(x) \quad , \tag{5.9}$$

and the preprocessed input signals (real and positive) by

$$s'(x) = s^R(x) \cos \omega_c x + s^I(x) \sin \omega_c x + B \quad , \tag{5.10}$$

where ω_c is the spatial frequency carrier used to achieve quadrature modulation and B is the bias term used to ensure that the input is positive. The signal recorded at P_{01} and subsequently imaged onto the photo-DKDP light valve at P_{02} can be re-written as

$$s_1'(x) = [s_1^R(x) - js_1^I(x)] \exp(j\omega_c x) + [s_1^R(x) + js_1^I(x)] \exp(-j\omega_c x) + B . \quad (5.11)$$

This same signal is recorded on all N lines at P_{01}.

Incident on P_2 after single sideband filtering at P_1, we find the signal to be described by

$$s_1''(x) = [s_1^R(x) + js_1^I(x)] \exp(-j\omega_c x) . \quad (5.12)$$

With the transmittance of P_2 analogous to Equation (5.11) for s_2, we find the light distribution leaving P_2 to be

$$s_1''(x)s_2'(x) = [s_1^R(x) + js_1^I(x)][s_2^R(x) - js_2^I(x)]$$

$$+ [s_1^R(x) + js_1^I(x)][s_2^R(x) + js_2^I(x)] \exp(-j2\omega_c x)$$

$$+ B[s_1^R(x) + js_1^I(x)] \exp(-j\omega_c x) . \quad (5.13)$$

The 1-D horizontal Fourier transform of Equation (5.13) obtained at P_3 of Figure 5.8 is then (along the $\tau = 0$ axis in the central $x_3 = 0$ region of P_3):

$$U_3(x_3) = \mathcal{F}\{[s_1^R(x) + js_1^I(x)][s_2^R(x) - js_2^I(x)]$$

$$= \mathcal{F}[s_1 s_2^*] = \chi(0, \nu) . \quad (5.14)$$

Considering the signal on all vertical lines, we obtain at P_3:

$$U_3(x_3, y_3) = \mathcal{F}[s_1(x)s_2^*(x+\tau)] = \chi(\tau, \nu) , \quad (5.15)$$

which is the desired passive ambiguity function. The coordinates (x_3, y_3) of the output ambiguity plane are proportional respectively to the differential range $(\tau_1 - \tau_2)$ and Doppler $(\nu_1 - \nu_2)$ of the source emitting the radiation [5.18].

In Figure 5.9, we show the real-time optically produced output ambiguity function obtained using the photo-DKDP light valve for a linear FM input signal test pattern. The location and shape of the optically produced passive ambiguity function shown are in excellent agreement with the theoretical result [5.18], both in terms of the angle at which the ridge of the ambiguity function occurs and in terms of its shape and width in range and Doppler [5.18].

5.6 Accuracy Comparisons

We now consider the accuracy of the optically produced output signal and image correlation patterns presented in Sections 5.4 and 5.5. We first consider the signal processing ambiguity function outputs (Figure 5.7), since the resultant output pattern is easy to describe mathematically for such cases. From Equation (5.7) for the 1mm wide pulses used, we find a theoretically predicted width in Doppler of

$$\Delta u = \lambda f_{FL}/2\sqrt{2} = 0.170 mm \quad . \tag{5.16}$$

From Figure 5.7c, we find a measured output correlation for the central lobe of 0.173mm in excellent agreement with theoretically predicted value from Equation (5.16). In the range or τ direction, Equation (5.8) predicts a central pulse width of

$$\Delta\tau = 2\sqrt{2} \ f_{FL}/f_{LC} = \sqrt{2} \ (762/300) = 7.2 mm \quad . \tag{5.17}$$

From Figure 5.7d, we find a measured central pulse-width of 7.25mm, as before, in excellent agreement with the theoretical correlation pulse width predicted by Equation (5.17).

In Figure 5.7b, we see three correlation peaks in range. The theoretical peak-to-sidelobe ratio expected for these peaks should be four. The measured values of peak-to-sidelobe levels in Figure 5.7d show this ratio to be 4.3. These values are again in good agreement with those predicted by theory. In general, the accuracy

of the measured optically produced output patterns are limited by: (a) the 50μm probe size used to scan the output correlation plane patterns, (b) the accuracy with which the input patterns are recorded and (c) the degree to which the system was aligned in the correlation experiments.

We next consider the accuracy of the real-time optical word recognition application (Figure 5.5). Specifically, we compare the optically produced correlation outputs using photo-DKDP as the real-time input transducer to the analogous results obtained using film as the input medium. An analysis of the input text pattern showed that the input character stroke-width was 80μm. The expected width of the corresponding correlation plane peaks is thus 160μm. Considering the f_{FL1}/f_{FL2} = 762/300 = 2.54 reduction factor introduced into the output correlation plane, the expected correlation peak widths are 63μm. To scan an entire line of the output correlation plane P_2 pattern, a 50μm fiber-optic point probe with a 2.5 X objective lens was interfaced to a scanning photometric microscope and X-Y chart recorder, resulting in an effective output correlation plane scanning probe size of only 20μm. From an analysis of these cross-sectional scans of the output correlation plane patterns, correlation peak intensities I_p of 30, 28, 28, and 27 (relative units) were measured from the real-time optical correlation outputs.

When the entire experiment was repeated with a film input, correlation peak intensities of 37, 34, 32, and 29 (relative units) were obtained (in excellent agreement with the results found using photo-DKDP as the real-time input transducer, considering the different system topologies and P_1 media used). To compare the experimentally obtained correlation peak widths obtained using the photo-DKDP light valve and film as the input media, attention must be given to the spatial frequency u' at which the beam balance ratio K (ratio of signal-to-reference intensity) is set equal to 1 (see Reference [5.20] for a more detailed description of this experimental procedure). With K set equal to one at x = 4mm (8.3cy/mm) in both the photo-DKDP and film cases (note that the spatial frequency corresponding

to the stroke width of the character in the optical word recognition input is
$\frac{1}{2}$ x 30 m = 6.25cy/mm, which is close to the chosen u' value), the output correla-
tion peak widths obtained were 90μm for the case of an input recorded on photo-
DKDP and 60μm for the case of a film input. We attribute this 30% difference in
experimentally measured correlation peak widths to the lower gamma (slope of the
transmittance vs. linear exposure curve), resolution, and modulation found for
our photo-DKDP SLM as compared to film. For the photo-DKDP, we found a peak
modulation of 30% and a resolution of 12cy/mm at 50% of this peak modulation
value.

5.7 Conclusion and Summary

The use of the photo-DKDP SLM in various optical data processing applications
has been experimentally demonstrated. In the image addition and subtraction appli-
cations, the appropriateness of image subtraction in real-time directly on the SLM
has been noted to be a viable method for correlating imagery from different sensors
or infrared imagery taken at different times. Two new optical pattern recognition
applications of this SLM in image (gray scale) and text (binary image) optical
pattern recognition have been demonstrated. From the comparative data obtained
using film inputs, the effect of optical path difference errors in the SLM and
anticipated space-variant SLM defects were found experimentally to be of minimum
concern. The correlation peak values for all four occurences of the key word were
experimentally verified to be comparable to the corresponding values obtained
using the film inputs. Correlation width differences in these two data sets were
found to be due to the limited resolution, modulation, and gamma of the photo-DKDP
SLM. Finally, from two optical signal processing correlation function applications
in which an optically generated ambiguity function was produced, the agreement
between the theoretically predicted and experimentally obtained outputs were found
to be excellent. Although the input patterns were imaged onto the DKDP light valve
in all described experiments (this was done to better allow comparison data from

which the degrading effects of the DKDP SLM could be determined), real-time
scanners and imaging methods would be utilized in practice in all applications
considered.

5. REFERENCES

5.1 Optical Engineering, Special Issue on Spatial Light Modulators, Vol. 17, July (1978).

5.2 D. Casasent, Proc. IEEE, 65, 143 (1977).

5.3 J. Donjon, et.al., IEEE, ED-20, 1037 (1973).

5.4 G. Marie and J. Donjon, Proc. IEEE, 61, 942 (1973).

5.5 F. Dumont, J. Hazan and D. Rossier, Philips Tech. Rev., 34, 274 (1974).

5.6 G. Marie, et.al., Chap. in Advances in Image Pick-Up and Display Devices, (B. Kazan Ed., Academic Press, New York, May 1974), pp. 225-302.

5.7 B. H. Billings, JOSA, 39, 797 (1949).

5.8 D. Casasent and Y. Barniv, SPIE, 137, 57 (1978).

5.9 R. Y. Wong, IEEE, SMC-7, 836 (1977).

5.10 E. L. O'Neill, IRE, IT-2, 56 (1956).

5.11 P. Consodine and R. Gonsalves, Chap. in Optical Data Processing: Applications, (D. Casasent Ed., Springer-Verlag, Heidelberg, 1978).

5.12 A. Vander Lugt, IEEE, IT-10, 139 (1964).

5.13 D. Casasent, "Optical Pattern Recognition," Proc. IEEE, May (1979).

5.14 D. Casasent, Chap. in Optical Data Processing: Applications, (D. Casasent Ed., Springer-Verlag, Heidelberg, 1978).

5.15 A. Rihaczek, Principles of High Resolution Radar, McGraw-Hill, New York (1969).

5.16 R. Said and D. Cooper, Proc. IEE (England), 120, 423 (1973).

5.17 R. Marks, et.al., Appl. Opt., 16, 746 (1977).

5.18 D. Casasent and B. V. K. Kumar, Appl. Opt., (Accepted).

5.19 L. Cutrona, et.al., Proc. IEEE, 1026 (1966).

5.20 D. Casasent and A. Furman, Appl. Opt., 16, 1652, 1662 (1977).
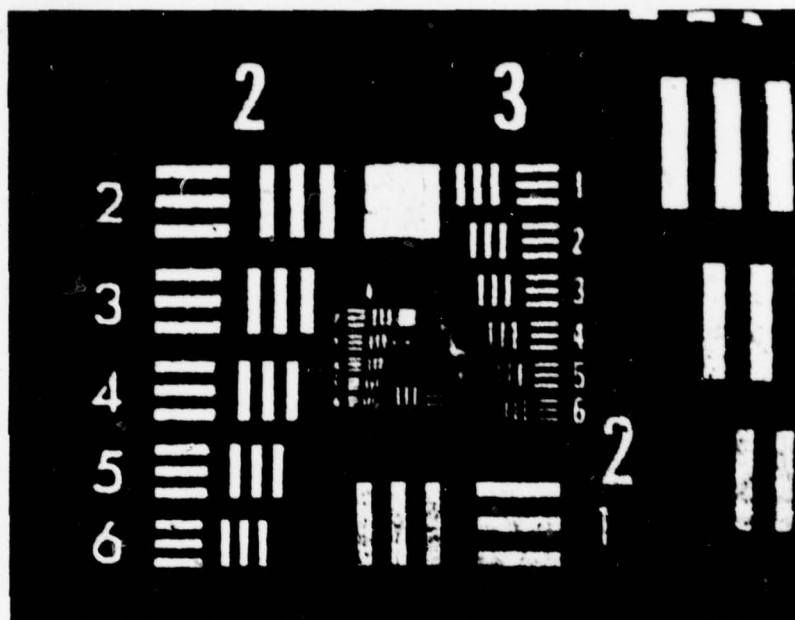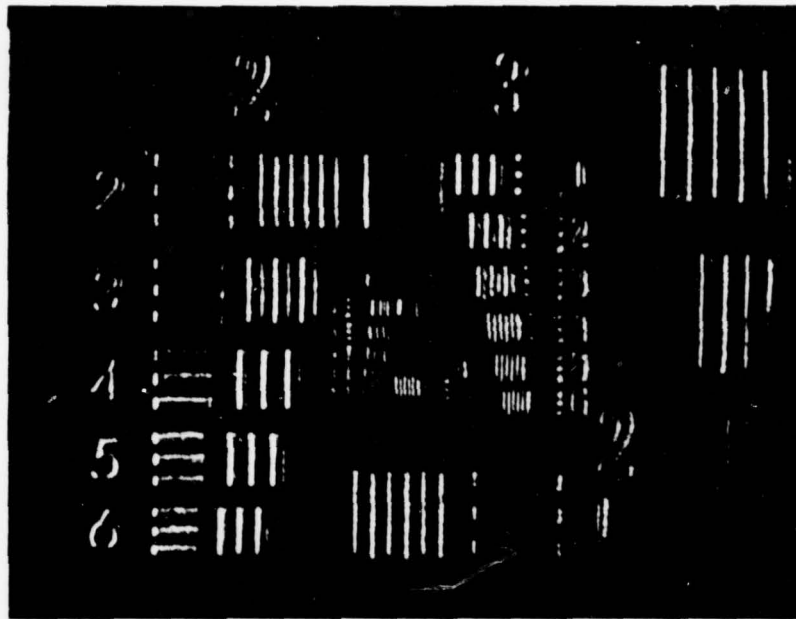
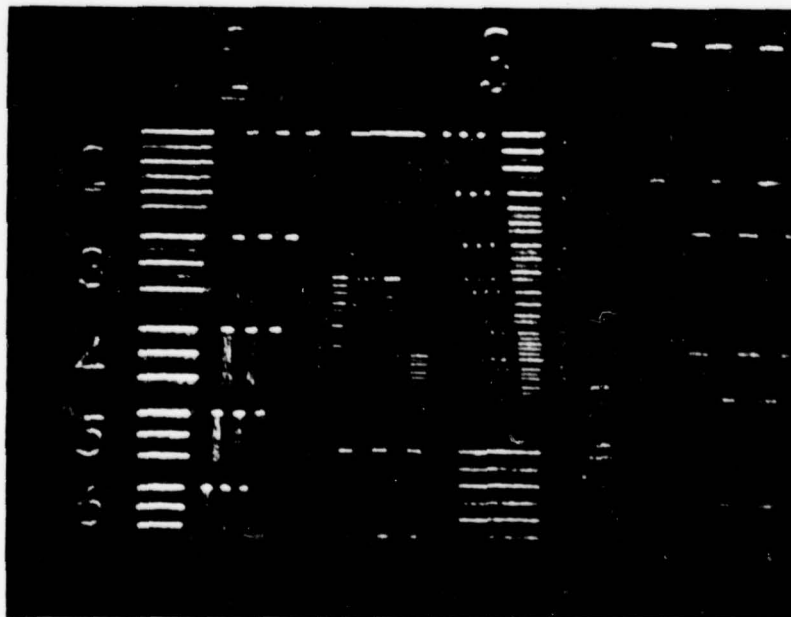(a) Positive Image (E_1 = 150V)
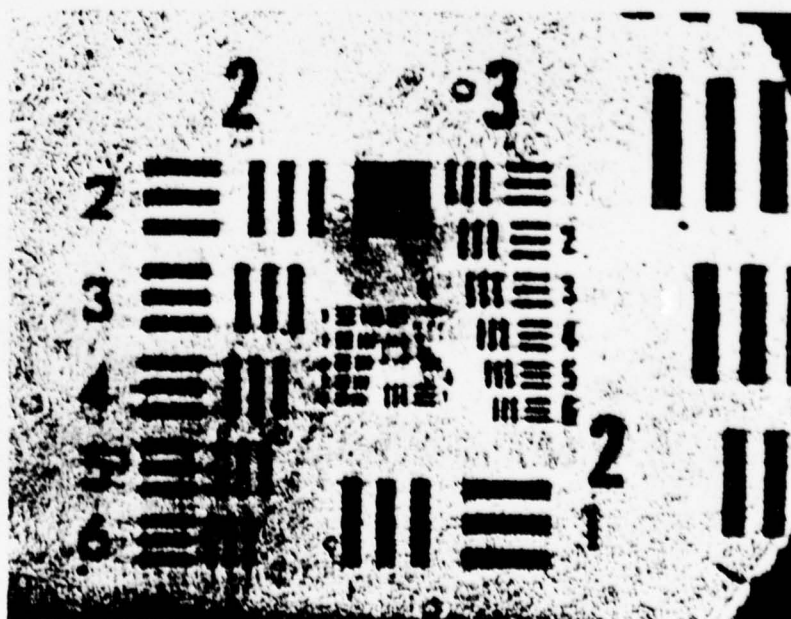
(b) Negative Image (E_1 = -150V)

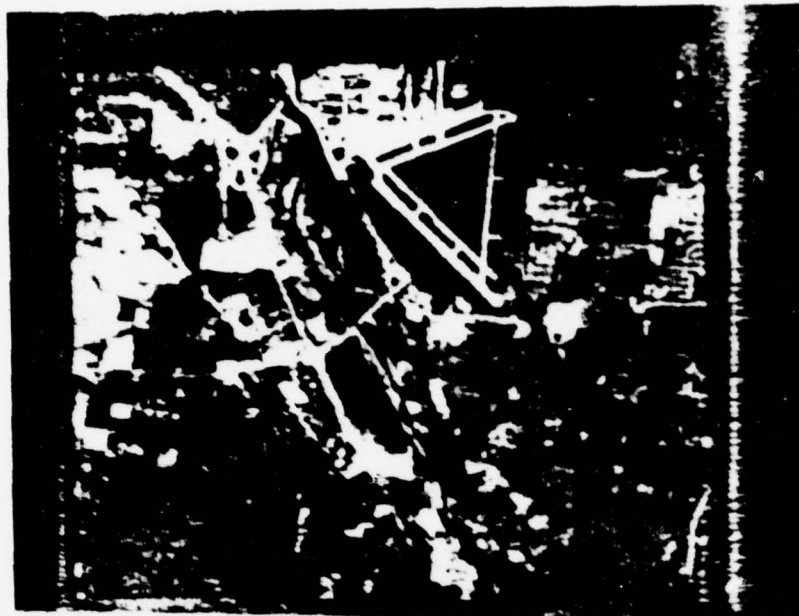Figure 5.1 Real-Time Reconstructed Imagery Using Photo-DKDP SLM

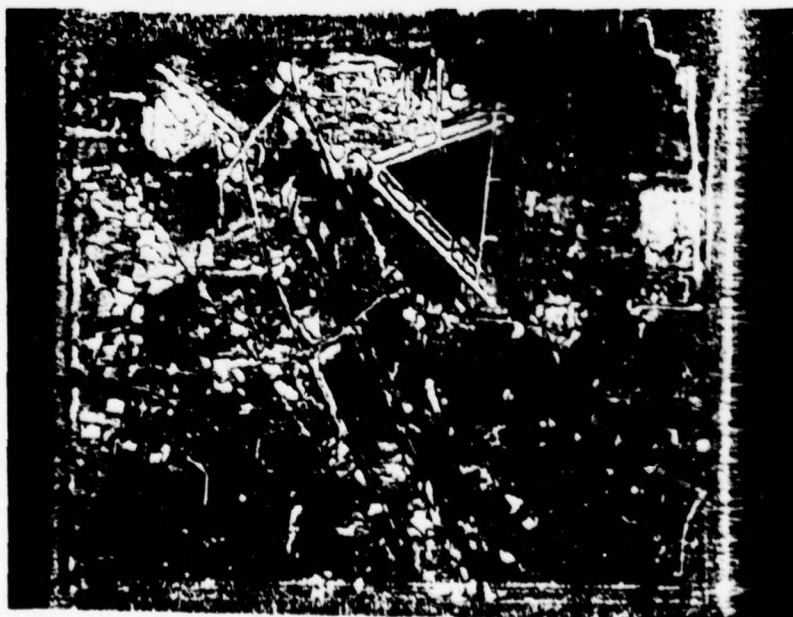(c)   Horizontal Differentiated Image

(d)   Vertically Differentiated Image

Figure 5.1   Real-Time Reconstructed Imagery Using Photo-DKDP SLM (Cont.)

(a) Input

(b) High-Pass Filtered Reconstructed Output Image

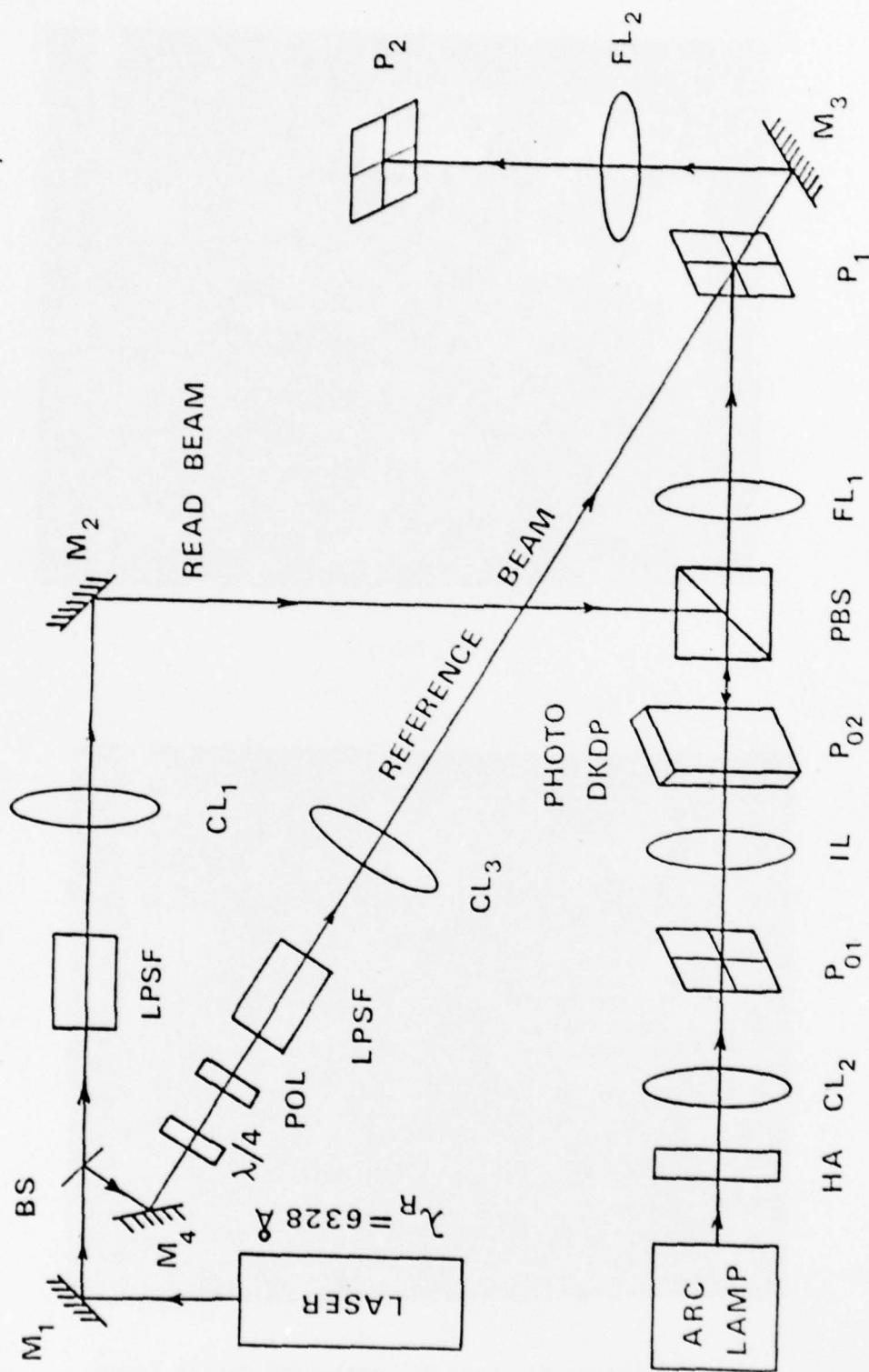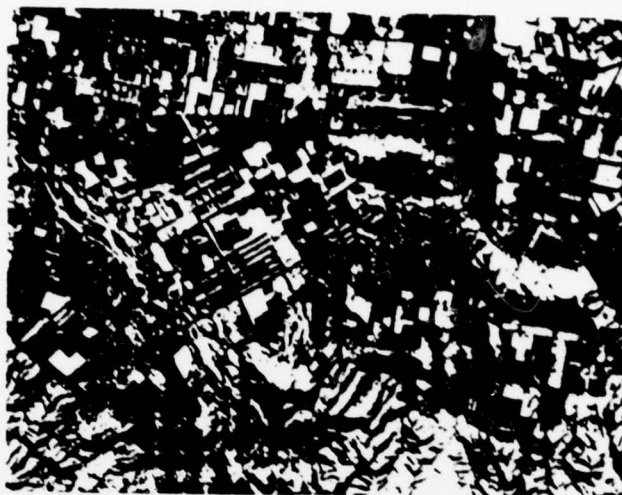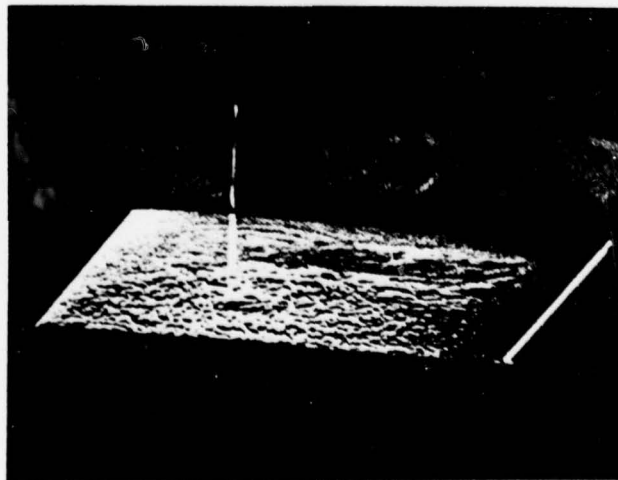Figure 5.2 Real-Time Reconstructed Aerial Image High-Pass Filtering Using Photo-DKDP

Figure 5.3 Schematic Diagram of Real-Time Optical Pattern Recognition Correlation System
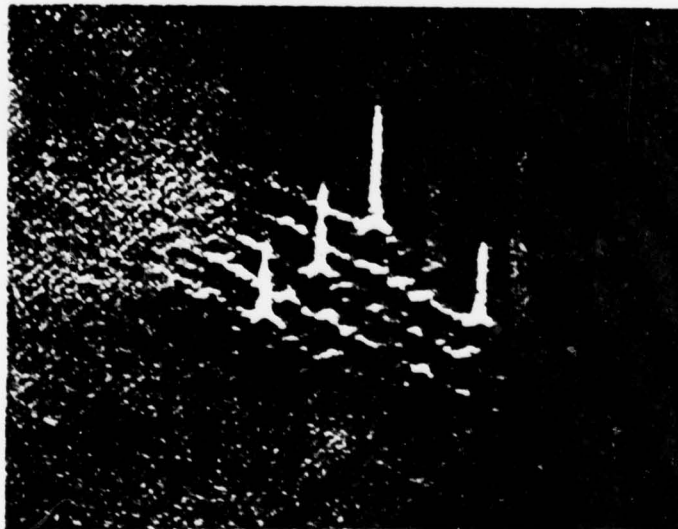
(a)

(b)

(c)   Isometric Pseudo 3-D Output

Figure 5.4   Real-Time Aerial Image Correlation Using Photo-DKDP

INPUT

CORRELATION OUTPUT

(b) Isometric Pseudo 3-D Output

Figure 5.5 Real-Time Optical Word Recognition Text Correlation Using Photo-DKDP
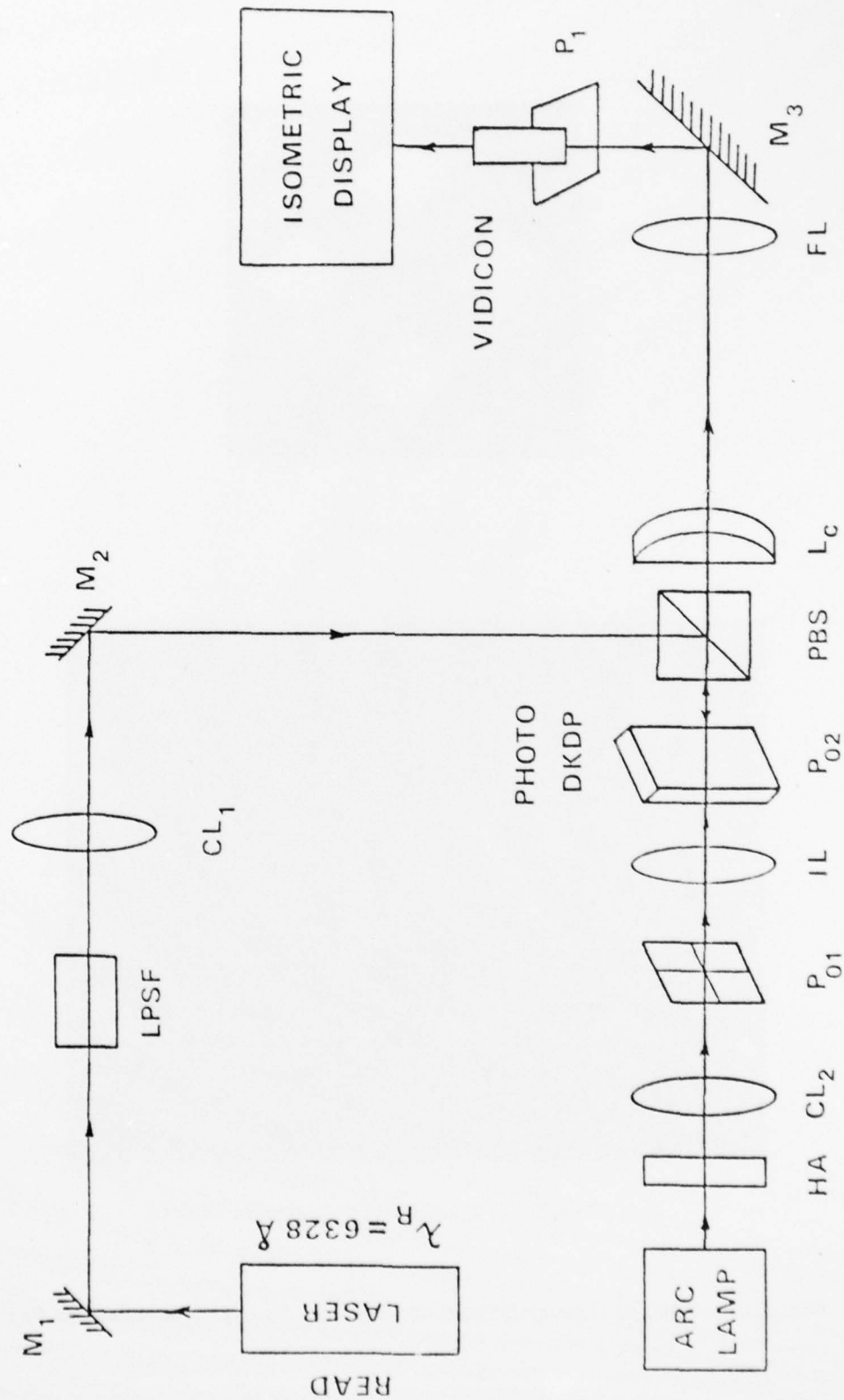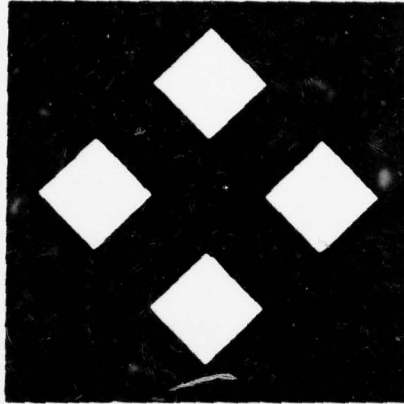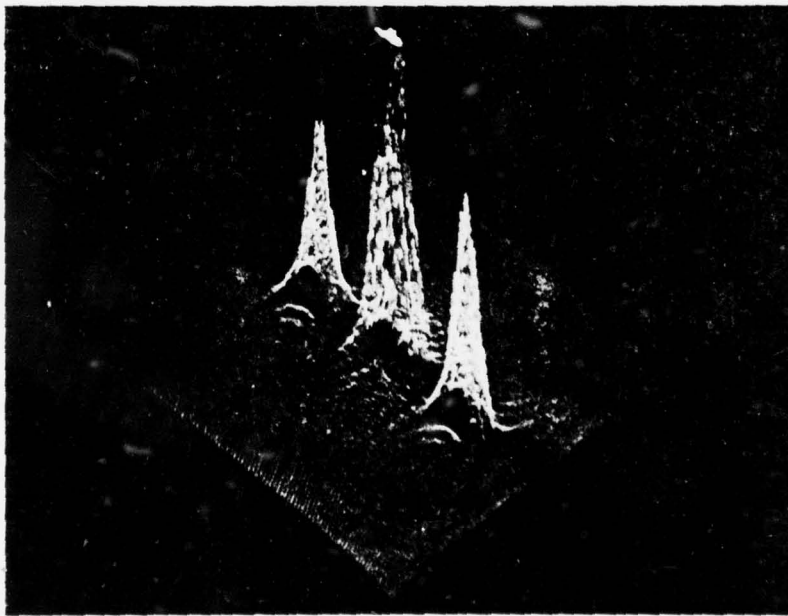
Figure 5.6 Schematic Diagram of Real-Time Crossed Input Ambiguity Function Optical Processor
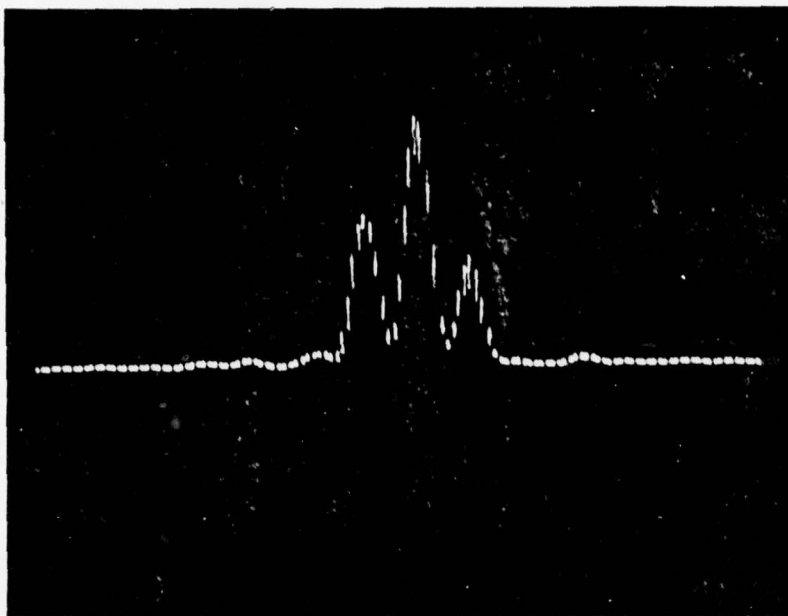
(a)   Input

(b)   Pseudo 3-D Amgiguity Function Output
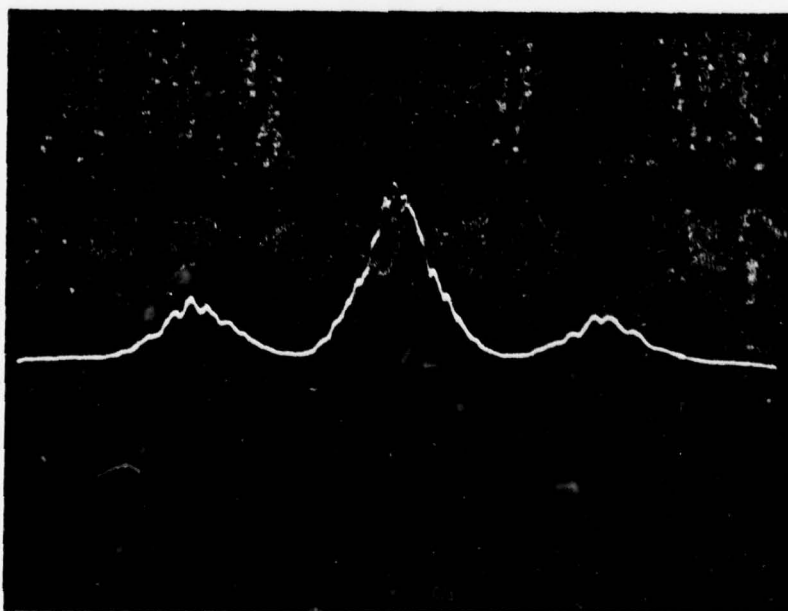
Figure 5.7   Real-Time Crossed Input Optical Ambiguity Function Generation Using Photo-DKDP

(c) Cross-Sectional Scan of (b) in Doppler ν

(d) Cross-Sectional Scan of (b) in Range τ

Figure 5.7 Real-Time Crossed Input Optical Ambiguity Function Generation Using Photo-DKDP
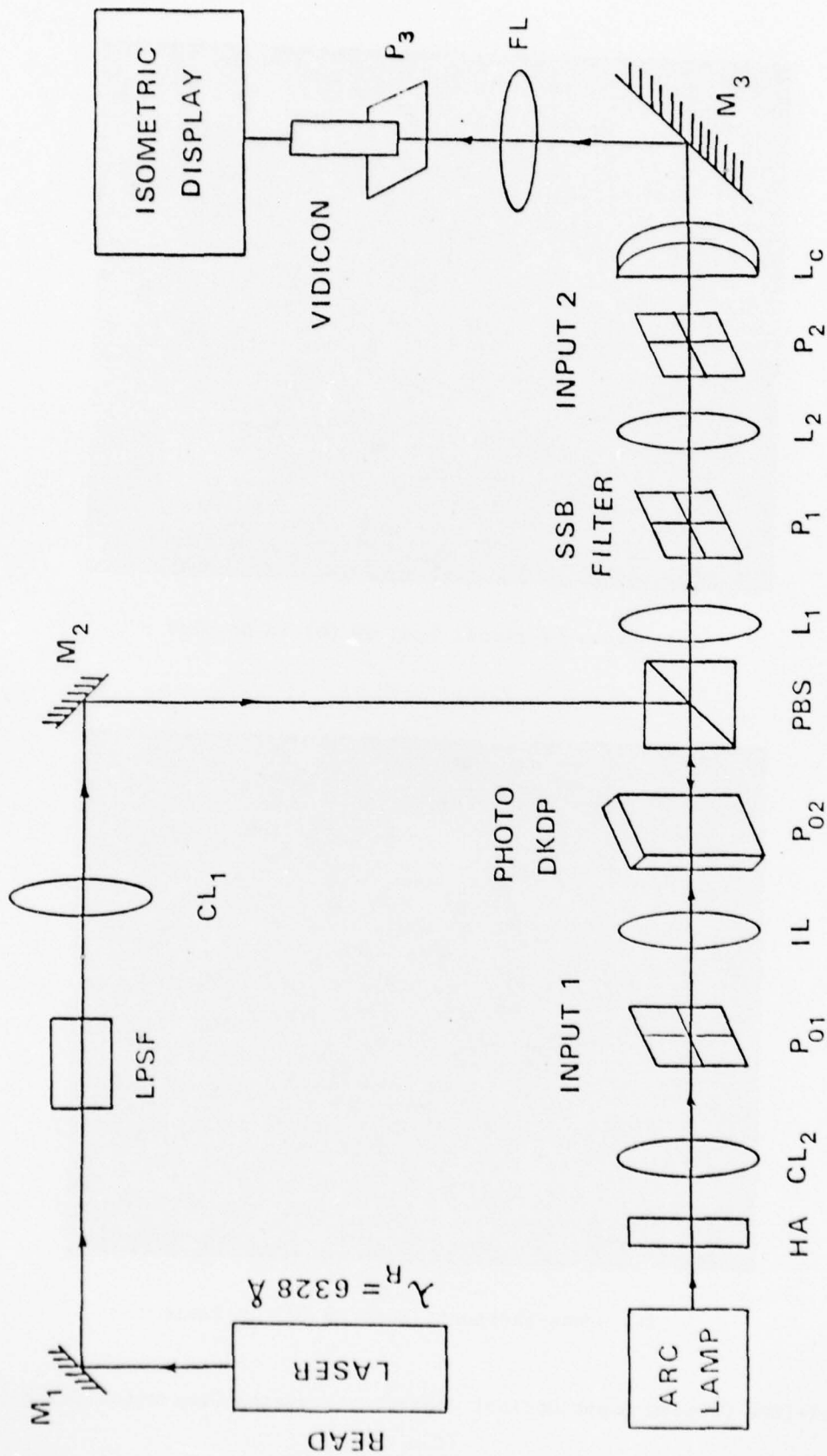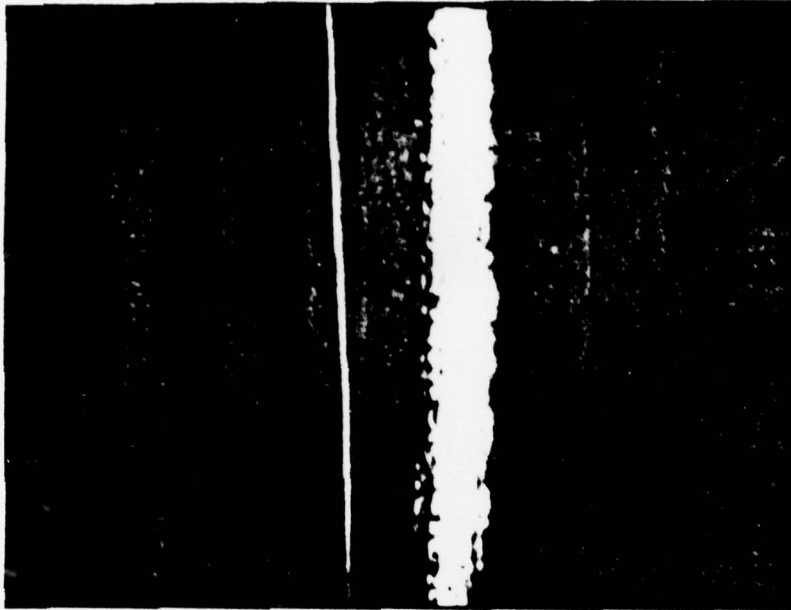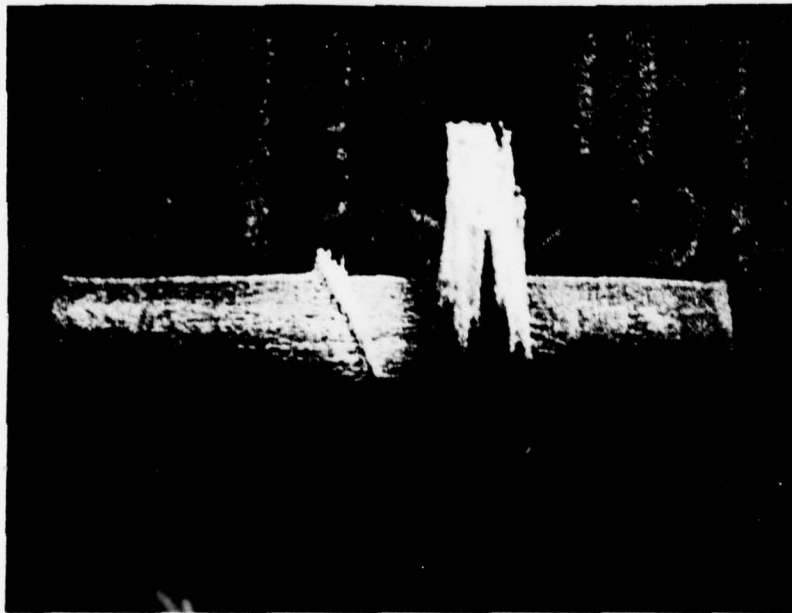(Con't)

Figure 5.8 Schematic Diagram of a Real-Time Optical Processor for Passive Ambiguity Function Computation

(a)   Orthographic Pattern

(b)   Isometric Pattern

Figure 5.9   Real-Time Optically Produced Passive Ambiguity Function for Linear FM
Input Data

6.   SUMMARY AND CONCLUSIONS

6.1 Summary

Real-time SLMs will remain the critical technology component in coherent optical data processors. As the discipline of optical data processing continues to mature, there is an urgent need for contractors and government agencies to adequately and fully specify the test, evaluation, and performance of these SLMs. The purpose of this present contract was to develop as unified of an SLM test and evaluation program as one can and to pursue experiments on the photo-DKDP SLM and analysis of prior experimental data on the LCLV SLM.

6.1.1 SLM Test and Evaluation

As the three major SLM parameters of concern, we have chosen: sensitometry, resolution, and noise.

The general SLM test and evaluation procedure we recommend was described in Section 2. In the area of sensitometry, we caution researchers to consider spatial variations and variations in the shape of the curve with control parameters, as well as field dependence (if static sensitometry data is used).

For resolution measurements we recommend use of unnormalized MTF data, careful distinguishing between amplitude and intensity modulation, and between linear and non-linear MTF. Above all, an accurate and complete description of the test procedure used is imperative. Interferometric MTF data is preferable whenever possible. The depth-of-focus of the lens system used in the SLM's actual application will determine whether interferometric MTF data are permissible.

In the area of SLM noise, we have distinguished three types of noise: scatter, phase, and amplitude linearity. We have described test systems for each, and obtained experimental test data on each.

Scatter level noise is a measure of the system's dynamic range, the SNR obtainable and the SNR loss due to the SLM. This data is most easily obtained from the FT of a square input aperture. This test should be performed in the same system with and without an SLM present.

Phase or OPD noise errors in an SLM are normally specified as rms values. However, as we have shown, spatial OPD maps are necessary to adequately describe the source and effect of such a noise source. Thus, attention should be given to how such phase errors are distributed and their spatial frequency (high or low), rather than to their rms values. A simple system using two input slits of fixed separation and variable location can be used to directly acquire such OPD data.

The third noise source we distinguish consists of non-linear amplitude response or equivalently interharmonic distortion. This noise source is best measured from the magnitude of the second-order term in the FT of an interferometrically recorded sinewave. We recommend that the "linear interferometric MTF" measurement technique (maintaining the intensity of the second harmonic 20dB below the fundamental) be used to obtain device resolution data as well.

6.1.2 LCLV

All SLMs are significantly different that a general test and evaluation procedure appropriate for all real-time transducers is difficult to devise. This point is best seen by specific SLM case studies. We consider the LCLV first, since it has been extensively studied and is well documented and fairly well understood. In our test and evaluation of this SLM, its sensitometry, as well as its contrast ratio were found to vary spatially. In addition, the shape of the sensitometry curve was found to change as the magnitude and frequency of the voltage applied across the device is varied.

The origin of these LCLV features were theoretically analyzed and described using an off-state model for the entire LCLV. Extended modifications of this

model were advanced and a complete device description using this model was presented. From this analysis, variations in the thickness of the LC layer appear to be the major reason for the spatial response variations; whereas the variations in the shape of the device's sensitometry curve were explained directly from the RC time constants in the LCLV model.

We thus recommend that device research on the LCLV be directed toward maintaining a more uniform LC thickness. We also hasten to note that if thicker LC layers (and resultant slower device speeds can be tolerated in the specific application) that the effect of these LC layer thickness variations on contrast ratio and dynamic range can be greatly reduced. From our local LCLV sensitometry data, we note that the potential capabilities of the LCLV are a contrast ratio in excess of 10,000:1 and a dynamic range of 30,000:1.

6.1.3 Photo-DKDP

The major portion of our experimental program was devoted to the test and evaluation of the photo-DKDP SLM. This SLM is manufactured in France and has no U.S. equivalent. It thus merits far more attention and more extensive test and evaluation than we were able to provide. Available funds provided support for only one student with no telephone, Xerox or equipment support. As a result, many concessions had to be made in the test and evaluation program of this device. Nonetheless, a wealth of new information, an in depth description of prior information, and considerable first hand experience with this device resulted from this one year study.

Sensitometry, resolution, and noise tests on this SLM were all successfully performed. The optical quality of the device was measured at $\lambda/2 - \lambda/4$ over the central $2 \times 2 \text{cm}^2$ device area. This should be improved to better use the device in coherent optical processing, although other U.S. SLMs have similar true rms OPD. We note that use of this SLM introduces only 3dB of added scatter level noise and that it still permits fabrication of a 53dB dynamic range SNR optical processor and that these are admirable specifications.

An extensive electronic, vacuum, and cooling support system had to be fabri-
cated to allow this device to be tested. An improved version of such a system
(as well as a better optical 3-axis mount for the SLM) should be fabricated if
extensive tests are to be performed on it. The device's resolution at 50% of the
peak modulation is 16cy/mm with a limiting resolution of about 40cy/mm or more.
Its dark storage time and storage time under readout were found to be excellent.

A new and extensive analysis of the device including a carrier description
of its operation was performed. This provided considerable new information and
allowed analysis of our observed results. The major new finding on the physics
of this SLM was the voltage dependent photo-sensitivity of the Selenium photo-
conductor used. The photo-sensitivity was found to vary as a function of the
field across the photoconductor layer. This same effect may well occur in other
storage mode SLMs, such as the Prom and should be considered in any SLM sensi-
tometry experimental test and evaluation program. We also verified the known
superior transport efficiency of holes over electrons in this SLM. The effect
of these two SLM features are that the device performs poorer for long exposures
than for short exposures.

Thus, sensitometry data acquired statistically with long exposures will
not apply during shorter exposure dynamic tests in actual device operation.
This aspect of SLM performance affects the test and evaluation, as well as the
measurement procedure to be used. The only disadvantage of these effects is
that linear addition and subtraction of gray scale imagery on this SLM is not
possible. However, as we have shown, use of alternate dopings with different $\mu\tau$
products than our unit appears to exhibit can aleviate this situation if such
interferometric operations are desirable. In essence, these remarks are most
attractive, since they indicate that the dynamic performance of this SLM will be
superior to its static performance (that we measured).

6.1.4 Real-Time Application Demonstrations

We have demonstrated the real-time reconstruction of binary imagery text resolution charts, as well as gray scale scenes on this SLM. We have also demonstrated contrast reversed imagery image addition and subtraction, plus 1-D and 2-D horizontal and vertical differentiation on this SLM.

We have used the device as the input transducer for four different image and signal pattern recognition systems for: word correlation, missile guidance image correlation, and for ambiguity function computation using a crossed input and image plane correlator topologies. In the former two image pattern recognition systems, we duplicated the experiments with film inputs and compared the real-time results (using the SLM input) to those using the film (off-line) inputs. In the latter two optical pattern recognition systems, the accuracy of the optically produced ambiguity function outputs were compared to the theoretically expected ones. In all instances, the real-time optically generated output correlation patterns were very accurate and agreed with the off-line film inputs and the theoretically predicted results.

6.2 Conclusions

The photo-DKDP SLM was found to be a most attractive and viable real-time and reusable SLM for coherent optical data processing. Its sensitivity is excellent, however improvements in its optical quality and assessment of its limiting resolution are needed.

6.3 Future Work

The unforeseen and unexpected experimental results obtained in our LCLV and photo-DKDP SLM test and evaluation work have clearly influenced the general SLM test and evaluation procedure we have advanced. Further experiments on both of these SLMs (especially with attention to dynamic tests) and a complete battery of tests on the prom and CCD addressed LCLV, plus attention to filter plane uses of

all of these SLMs will unquestionably refine the general test and evaluation procedure to be used even further. Since all SLMs are considerably different and all have their unique quirks, firsthand experience and a one year test and evaluation program on each device appears necessary. Adequate documentation and uniformity of test procedures used will make the various independent and similar programs of this type of more use.

The application, as well as the associated optical data processing system architecture must be considered in all cases. The optical system architectures should be chosen to suit the SLM with its deficiencies, rather than insisting on the use of one system architecture and then requiring the existance of a perfect SLM. Specific mission oriented programs with extensive SLM usage, are felt to be necessary and must completely assess this issue, as well as the test and evaluation procedure to be used in a given application and the appropriateness of various tests.

Since SLMs have large resolution (above 100cy/mm in many cases) but this resolution is only available at greatly decreased modulation, we feel that: a system light level budget analysis, input recording accuracy and fidelity, lens requirements, and most important, a detector test and evaluation program are necessary. These programs should be mission oriented ones with the reasons advanced above.